

CONFIDENTIAL

Gyroscopic Motion Control During The Lowering Procedure of Monopile Installation

R. A. A. Wiskie

Technische Universiteit Delft



CONFIDENTIAL

GYROSCOPIC MOTION CONTROL DURING THE LOWERING PROCEDURE OF MONOPILE INSTALLATION

by

R. A. A. Wiskie

To obtain the degree of

Master of Science

in Aerospace Engineering: Aerodynamics and Wind Energy

at the Delft University of Technology,
to be defended publicly on the 24th of November 2021.

Student number:	4228936	
Supervisors:	Dr. ir. W. A. A. M. Bierbooms,	TU Delft
	Ir. J. Koppenol,	TWD
Thesis committee:	Dr. ir. W. A. A. M. Bierbooms,	TU Delft
	Ir. J. B. van Wuijckhuijse,	TWD
	Dr. ir. J.M. Kuiper,	TU Delft
	Prof. dr. D.A. von Terzi,	TU Delft

This thesis is confidential and cannot be made public until the 24th of November 2023

ABSTRACT

Due to the ever increasing demand of energy and the urgency in which this has to be produced using renewable energy resources the request for offshore wind farms is larger than ever. As a result of the competitive nature of the energy sector it is important to keep the cost of energy low in order to keep an edge over the competition. Therefore, to keep wind energy economically viable in the future the cost of producing energy should be lowered. One way this can be done is by lowering the initial costs of installation, as this is relatively high. In this thesis an installation method of monopile foundations will be introduced, which has potential to reduce costs of the installation of wind farms. More specifically, this thesis will focus on lowering of monopiles to the seabed. Problems arise when the monopile hanging on the crane wire is excited by waves hitting the submerged part of the monopile. This can cause excessive motion of the monopile. Particularly if resonance occurs, which is the case when the wave frequencies and the natural frequencies of the monopile coincide. This could lead to catastrophic failure if no mitigating measures are taken. The most common method to counteract this phenomenon is to wait until weather conditions allow for further continuation of operations, which can consume lots of valuable time and thus increasing costs.

Therefore, this thesis will focus on optimizing the workability of offshore installations of monopiles by using gyroscopic motion actuators. These actuators, called control moment gyroscopes (CMG), will reduce motion of the monopile by applying a moment counteracting the moment created by the waves. This system is modelled in MATLAB. The model consists of the monopile suspended on the crane wire, a gripper and the CMG. The equations of motion are determined using the Lagrangian method and linearized around their equilibrium position. The equations of motion are then written in state space representation in order to study the behaviour of the system and to tune the PD controller. The PD controller was tuned using the loop shaping method. The MATLAB model is used to tune the controller. However, the results will be examined using OrcaFlex. Therefore, the same system is also modelled in OrcaFlex, a commercial time domain simulations package, in which an external function is built using Python to represent the CMG and the corresponding PD controller of the CMG moment. The whole system is then subjected to a sea state with a significant wave height of 2 meters and a wave period range from 5-8 seconds. The 3 hour simulations are run for each period step of 0.5 seconds from 5 to 8 seconds. From each simulation the most probable maximum is calculated. This is done for four variants of the system: A system where the CMG is present but not spinning, a passive system in which the CMG is spinning and free to precess around its axis, an actively controlled system where the nutation angle is controlled and the actively controlled system that sets a limit to the maximum moment the CMG can produce. This moment is determined to be $1158kN$, which at this point is deemed to be within technological and physical limits.

The results show that the passive system could be an option to reduce crane wire angles if the system is designed in a manner that removes the natural frequency sufficiently far away from the wave frequencies. At this point the passive systems only shows better results near the natural frequency of the system, which are at the higher end of the period range. As expected the actively controlled system performs best with the largest reduction in maximum crane wire angle of 74%. When the whole period range is considered the average reduction is 48%. Another benefit is the reduction in the forces on the gripper, where a maximum reduction of 38% can be seen and an average reduction of 17%. The passive system performs poorly in this area and actually increases the force on the gripper. which at this point would not make it a preferable option compared to the active systems. The maximum reduction, of both active systems, happen near the resonance period of the original system where the CMG is not spinning. However, when the maximum moment is considered the average reductions for the crane wire angle and force in the gripper lowers to 15% and 7%, respectively. Nonetheless, this will enable the same equipment to operate in sea states with a higher significant wave height. Thereby increasing the workability of the lowering operation. The beneficial side effect that the actively controlled CMG system lowers the force exerted on the gripper by the monopile could lead to smaller and less intricate grippers lowering their design and construction costs and also their deck space needed. Both of which are cost saving for the total installation of offshore wind farms.

PREFACE

After what felt like an eternity I'm proud to present this Master of Science thesis on gyroscopic motion control. Ever since I've started my master at TU Delft I knew I wanted to do my thesis within a company that was in wind energy sector. Therefore I was more than happy when TWD gave me the opportunity to do my thesis on gyroscopic motion control. The idea that there is possibility that this idea might be realized in the future gave me extra motivation to achieve the goals set at the start of the thesis. Although the writing of a thesis is almost inevitably paired with ups-and-downs, it has been a pleasure being able to contribute to the development of the offshore wind industry.

I would like to express my gratitude to TWD for giving me this opportunity and all the colleagues that were never too busy to give me advice or help me when I was stuck on something. A special thanks to Bas van Wuijckhuijse for first hiring me as an intern. Then from an intern to an employee during my studies and finally appointing this research topic to me to do my master thesis on. Another person I would like to thank is Jim Koppenol for his help as my daily supervisor. Jim's expertise in dynamics and control helped me great deal throughout the thesis. Furthermore, my thanks goes to Wim Bierbooms as he was my supervisor from TU Delft. His guidance and advice on structuring my report and his willingness and availability to have meetings, be it online due to another lockdown because of the pandemic or in person at the TU Delft, has really supported me from start to finish.

My gratitude extends to my parents for always supporting me throughout my studies and always being there for me in times of need.

*R. A. A. Wiskie
Rotterdam, September 2021*

CONTENTS

Abstract	iii
List of Figures	ix
Abbreviations	xi
List of Symbols	xiii
1 Introduction	1
1.1 Background	1
1.1.1 Development of Wind Energy	1
1.1.2 Increasing Size of Turbines	1
1.1.3 Problems During Installation	2
1.1.4 Control Moment Gyroscopes	2
1.2 Research Objectives	3
1.3 Thesis Outline	4
2 Required Theory For Modelling Of A Mechanical System	7
2.1 Mathematical Model	7
2.1.1 Lagrangian Mechanics	7
2.1.2 Linearization of The Equations of Motion	10
2.1.3 State Space	12
2.2 Control	13
2.2.1 Standard PID-controlblock Diagram	13
2.2.2 Proportional Controller	14
2.2.3 Integral Controller	15
2.2.4 Differential Controller	15
2.2.5 Proportional-Integral-Differential Controller	15
2.3 Waves	17
2.3.1 Waves	17
2.3.2 JONSWAP	17
2.3.3 Morison	18
3 Modelling	21
3.1 MATLAB model	21
3.1.1 Equations of Motion	21
3.1.2 Linearization of The Equation of Motion	24
3.1.3 State Space Model	25
3.2 Monopile suspended in air	27
3.2.1 Determining Key Variables	27
3.2.2 Natural Frequencies of Monopile Suspended in Air	28
3.2.3 OrcaFlex	29
3.2.4 OrcaFlex Model Setup	29
3.2.5 Model Comparison and Validation	30
3.3 Monopile Including Added Mass	31
3.3.1 Determining Key Variables	31
3.3.2 Natural Frequencies of Monopile Including Added and Trapped Mass	32
3.4 Controller	33
3.4.1 PID controller	33
3.4.2 Controller OrcaFlex Integration	36

3.5	Control Moment Gyroscope	36
3.5.1	Equations of Motion CMG	36
3.5.2	CMG Dimensions	40
3.6	Monopile Including CMG	41
3.6.1	State Space Model Complete System	43
3.6.2	Control of The Total System	46
3.7	OrcaFlex Python Integration	49
4	Results	51
4.1	Results of Tuned CMG on Monopile in MATLAB	51
4.2	OrcaFlex Model Results	54
5	Conclusion and Recommendations	59
5.1	Conclusion	59
5.2	Recommendation	61
A	Equations of Motion of a Pendulum	63
B	Equations of Motion of a Pendulum on a Cart	67
C	MATLAB Code Example	71
D	Potential Energy Derivatives	75
E	Nonlinear Stiffness Matrix Elements	77
F	Control of a Cart-Pendulum System	81
G	Euler Angles	89
	Bibliography	93

LIST OF FIGURES

1.1	Illustration of active and passive gyroscopic stabilisation system on a vessel [33]	3
1.2	Flowchart of the steps taken to answer the research question	4
2.1	Potential energy of a locally stable system, [11]	10
2.2	Block diagram PID-control system	14
2.3	Bode plot of a PID-controller	16
3.1	Schematic representation of the monopile suspended from the crane	22
3.2	Modes of a monopile suspended from a crane wire.	29
3.3	OrcaFlex model	30
3.4	Comparison of first natural frequency between models	33
3.5	Comparison of second natural frequency between models	33
3.6	Block diagram PID control system	33
3.7	Bode plot of the system when crane wire is submerged 30 meters (crane wire length 99)	34
3.8	Bode plot of important loops	35
3.9	Initial condition response of θ	35
3.10	Monopile angle during 200s simulation with $H_s=2m$	36
3.11	Crane wire crane wire angle during 200s simulation with $H_s=2m$	36
3.12	Torque against angular momentum for both CMGs and RWs [36].	37
3.13	Simplified drawing of control moment gyroscope showing its degrees of freedom	37
3.14	Flywheel size with increasing radius with all other parameters as constants versus the maximum moment it can then produce	41
3.15	Simplified drawing of the monopile and the CMG that clearly show how the degrees of freedom act for θ and ϕ . The Left image is the front view displaying the monopile angle θ and the right image shows the side view showing the nutation angle ϕ	42
3.16	Bode plot from the moment around θ to the angle θ for different submerged depths	46
3.17	Bode plot from the moment around θ to the angle θ for different spinning velocities	47
3.18	Bode plot from the moment around ϕ to the angle ϕ	48
3.19	Bode plot from the moment around θ to the angle θ to see the effect of a disturbance force such as waves creating a moment on the monopile	49
3.20	The flowchart of the interaction between OrcaFlex and Python during each iteration of the calculation	50
4.1	The sinusoidal disturbance moment around θ	52
4.2	Response of monopile angle θ to a sinusoidal disturbance moment input around θ	52
4.3	Response of monopile angle θ to a sinusoidal disturbance moment input around θ with a frequency of $0.13Hz$. ($T_p = 8s$)	53
4.4	Spectral density of a wave train with $H_s = 2m$ and $T_p = 8s$	55
4.5	Most probable maximum monopile angle θ for whole range of T_p for an H_s of $2m$	56
4.6	Most probable maximum crane wire angles for whole range of T_p for an H_s of $2m$	57
4.7	Most probable maximum force on gripper for whole range of T_p for an H_s of $2m$	58
4.8	Comparison of two systems with a capped maximum moment to see the effect of a larger moment	58
A.1	Single pendulum	63
B.1	Cart pendulum	67
F.1	Cart pendulum	81
F.2	Control block diagram of the cart pendulum	82
F.3	Bode plot of θ of the cart pendulum system	83

E4	Bode plots of θ of the cart pendulum system and important transferfunctions	85
E5	Bode plot of θ of the cart pendulum system and important transferfunctions	86
E6	Initial conditions response of x	86
E7	Initial condition response of θ	86
E8	Initial conditions response of x	87
E9	Initial condition response of θ	87
E10	Bode plot of θ of the cart pendulum system	88
G.1	Illustration of the rotations around a fixed point using Euler angles [30]	90

ABBREVIATIONS

Abbreviation

CMG

MP

MPM

OWF

PID

JONSWAP

EOM

Word/Phrase

Control Moment Gyroscope

MonoPile

Most Probable Maximum

Offshore Wind Farm

Proportional Integral Derivative

Joint North Sea Wave Observation Project

Equations Of Motion

LIST OF SYMBOLS

Symbol	Description	Units
A	State matrix	–
A_{csmmp}	Crosssectional area monopile	m^2
A_m	Area monopile that the flowing water encounters	m^2
B	Input matrix	–
C	Output matrix	–
C_{height}	Height of cranetip above sealevel	m
C_e	Constant	–
D	Damping matrix	–
D_{mp}	Diameter monopile	m
D_{ss}	Feedtrough/Feedforeward matrix	–
D_g	Vertical distance from total cog to gripper	m
E	Energy	J
e	Error	–
F	Force	N
F_b	Buoyancy force	N
f_c	Crossover/bandwidth frequency	Hz
F_g	Gravitational force	N
F_w	Force of wire	N
g	Gravitation acceleration	ms^{-2}
G	Gain	–
G_{height}	Height of gripper above sealevel	m
G_x	Displacement of the gripper original position	m
H_s	Significant waveheight	m
H_x	Horizontal distance from crane top to hook	m
H_z	Vertical distance from crane top to hook	m
I	Inertia total system	kgm^2
I_{am}	Inertia added mass	kgm^2
I_{tm}	Inertia trapped mass	kgm^2
I_{xy}	Inertia CMG around x and y axis	kgm^2
I_{zcmg}	Inertia CMG around z axis	kgm^2
k	Stiffness	Nm^{-1}
K	Stiffness matrix	–
K_d	Differential gain	–
K_i	Integral gain	–
K_p	Proportional gain	–
$L_{stretch}$	The stretch of the cranewire due to gravity	m
L_{cgam}	Distance from top monopile to centre of gravity added mass	m
L_{cgmp}	Distance from top monopile to centre of gravity monopile	m
L_{cgtot}	Distance from top monopile to centre of gravity total system	m
L_{mp}	Length monopile	m
L_{sub}	Length of submerged part monopile	m
L_0	Unstretched length crane wire	m
L_e	Elongation of crane wire	m
L_w	Length crane wire	m
m	Mass	kg
M	Mass matrix	–
M_ϕ	Moment acting in the ϕ degree of freedom	N

M_θ	Moment acting in the θ degree of freedom	N
m_{am}	Added mass	kg
m_{cmg}	Mass CMG	kg
m_{mp}	Mass monopile	kg
m_{tm}	Trapped mass	kg
M_m	Mass of displaced volume of the monopile	kg
m_x	Mass in x-direction	kg
m_z	Mass in z-direction	kg
n_d	Number of degrees of freedom	–
P	Power	W
q	General coordinate position	m
\dot{q}	General coordinate velocity	ms^{-1}
\ddot{q}	General coordinate acceleration	ms^{-2}
Q	Generalized forces	N
r	Number of inputs	–
r_{in}	Inner radius monopile	m
r_{out}	Outer radius monopile	m
r_0	Reference signal	–
s	Number of outputs	–
T	Kinetic energy	J
t_{cmg}	Thickness CMG	m
t_{mp}	Thickness monopile	m
T_p	Wave Peak period	s
u	controller output	–
u_f	Velocity of fluid	ms^{-1}
V	Potential energy	J
x	Horizontal position	m
\dot{x}	Horizontal velocity	ms^{-1}
\ddot{x}	Horizontal acceleration	ms^{-2}
z	Vertical position	m
\dot{z}	Vertical velocity	ms^{-1}
\ddot{z}	Vertical acceleration	ms^{-2}
ϵ	Total energy	J
θ	Angle of monopile	Rad
$\dot{\theta}$	Angular velocity of monopile	$Rads^{-1}$
$\ddot{\theta}$	Angular acceleration of monopile	$Rads^{-2}$
ρ	Density	kgm^{-3}
ρ_{steel}	Density steel	kgm^{-3}
ρ_{sw}	Density seawater	kgm^{-3}
ϕ	Angle around x-axis (nutaton angle)	Rad
$\dot{\phi}$	Angular velocity around x-axis (nutaton velocity)	$Rads^{-1}$
$\ddot{\phi}$	Angular acceleration around x-axis (nutaton acc.)	$Rads^{-2}$
ψ	Angle around z-axis	$Rads^{-1}$
$\dot{\psi}$	Angular acceleration around z-axis	$Rads^{-2}$
$\ddot{\psi}$	Angular velocity around z-axis	$Rads^{-1}$
$\dot{\psi}_0$	Constant angular velocity around z-axis	$Rads^{-1}$
ω_d	Differential frequency	$Rads^{-1}$
ω_i	Integral frequency	$Rads^{-1}$

1

INTRODUCTION

1.1. BACKGROUND

1.1.1. DEVELOPMENT OF WIND ENERGY

Since the need for renewable energy is increasing, so does the need for Offshore Wind Farms (OWFs) as wind power is one of the greenest ways to mass produce energy with low CO₂ emissions [4] [37]. In China alone in 2018 1.6GW of offshore wind power capacity was added [16]. The global offshore wind capacity is rapidly increasing at a rate of 16% compound annual rate from 2017 to 2030. This will lead to a increase from 17.6GW to an expected 115GW and becoming a \$1 trillion industry in 2040 [16] [3]. However, to make wind energy an even more attractive energy alternative to fossil fuels, it needs to become an even more economically viable option. This can be done by tackling one of its most expensive elements: The installation of the foundations.

The installation of the foundations of an OWF is a costly element of the total cost and it is directly correlated to the time it takes to install the foundations. Reducing installation time therefore reduces the total costs. Over the years the industry has seen a reduction in the time it takes to install a complete OWF. However, no real advancement has been made in installing a single foundation. The reduction in time with respect to the total installation process can be accounted for by the increasing size of turbines. Which means less turbines per wind farm for an equal amount of power produced [18].

1.1.2. INCREASING SIZE OF TURBINES

The amount of wind turbines is not the only aspect that is steadily increasing. As mentioned before, the dimensions of the turbines itself have seen substantial growth over the years. Ever since the first wind turbine with a power production capability larger than 1MW was built in Denmark, in 1978 with a rotor diameter of 54m [8], the power production and the diameters have kept increasing. The latest General electric wind turbine, the Haliade-X, has a rotor diameter of 220m and 14MW capacity, [7].

Larger rotors lead to higher aerodynamic forces. Together with the fact that these wind farms are placed further offshore and thus in deeper waters means that the foundations have become larger as well, to be able to take these increased loads. An example of a modern monopile is the so called XL monopile produced in Rotterdam by Sif. It can have a diameter up to 11 meters and a length of 120 meters. These monopiles can weigh up to 2250 tons, [9].

Research shows that for installation of a single foundation, performed between 2014 to 2017, the total time is 2.56 days, [18]. These Large monopiles bring their own set of challenges during installation. Due to their increased weight the eigenfrequencies are lower and fall in the range of the wave frequencies. These lower frequent waves carry more energy. This might lead to resonance if the excitation of the waves has the same frequency as the eigenfrequency of the monopile while lowering. An example of where installation took much longer as planned is the "Borkum west wind farm". The planned installation time would be 200 days. However, due to bad weather the installation lasted for 367 days for which the installation vessel was rented the entire duration [34].

1.1.3. PROBLEMS DURING INSTALLATION

The way the installation is performed is dependent on which type of foundation is used. There are multiple types of foundations. The three main types used are jackets (8.9%), gravity based (5.7%) and monopiles (81%) [21], the percentages are valid for European OWFs. World wide this percentage is bit lower for monopiles but still more than 60% [31]. Since the monopile is the most widely used foundation type this report focuses on this method of foundation installation.

There are 3 main steps in installing monopiles: [20].

1. Upending the monopile from the horizontal position on deck to an upright position using the crane and an upending bucket.
2. Placing the monopile in the gripper and lowering it to the seabed. This means that the monopile will cross the wave zone and thus experience hydrodynamic loading that generates motion.
3. While the monopile is on the seabed and the gripper is restricting its motions it will be driven deeper into the seabed.

The costs of installation are directly related to the daily rate of the installation vessels which can be up to \$250,000/day [18]. To speed up the installation process one can make sure that the installation can be done in higher significant wave heights (H_s). As a result the workability of the operation increases and thus the total time of installation decreases. Subsequently, the installation vessel can be rented for fewer days reducing installation costs.

A part which is sensitive to the sea state is the lowering of the MP (this is true for all types of foundations) to the seabed. If the wave periods coincide with the natural period of the monopile hanging on a crane, resonance could occur and large displacements of the top can be observed leading to substantial off- and sidelead angles of the crane wire. Cranes in general are not build to withstand large horizontal loads and thus the off- and sidelead angles can be showstoppers if they exceed the thresh-hold values.

A possible solution to damp out these oscillations can be done with the use of gyroscopes. Such devices have been used in other fields of engineering with great success. Examples in which they have been frequently used are satellites and vessels [29], [19]. In satellites these gyroscopes are used for attitude control while in vessels they are most commonly used for roll damping [33], [32].

1.1.4. CONTROL MOMENT GYROSCOPES

Gyroscopes have been used in the stabilisation of objects and structures in many different fields. Well known examples are satellites and vessels, [29], [19]. In satellites the gyros are mainly used for attitude control while in vessels it is mostly installed to damp the roll motion of the vessel, [33], [32]. The main difference between these two is that for satellites three axis have to be controlled while in a vessel only one (roll), therefore making satellites control systems more complex. The type of gyrostabilisers can be divided into two main categories: Reaction wheels and Control Moment Gyroscopes (CMG).

The first type is a reaction wheel which is the simplest of the two. A reaction wheel relies on the acceleration and deceleration of a wheel to create a moment around a fixed axis using angular momentum to move the total system. Angular momentum is a conserved quantity meaning that the total angular momentum in a closed system is constant if no external torque acts upon the system. As a result angular moment can be exchanged between objects within a system. When a reaction wheel is suddenly accelerated it creates a moment. This moment equals the moment exerted on the object attached to the reaction wheel but in opposite direction which then causes the rest of the system to rotate if no external force acts on it, [36].

The second type of gyrostabiliser is the Control Moment Gyroscope . A control moment gyroscope uses a wheel that spins at a high, but constant (majority of the cases), angular velocity and makes use of the gyroscopic effect of called *Nutation* or *Precession* to create a moment around a specified axis, [33]. This moment is created when the spinning wheel is forced to spin at a different angle. It is called nutation if the gyroscope's spinning plane is actively forced to spin at a different angle forcing the attached object to rotate a certain

direction. Precession is where the attached object is moved and the gyroscope counter acts this moment by changing the plane of the spinning disc. Thus, creating a moment opposite of the motion of the rotation of the object. Precession is what what is happening in a passive system while nutation is used for actively controlled systems. This is visualized in Figure 1.1.

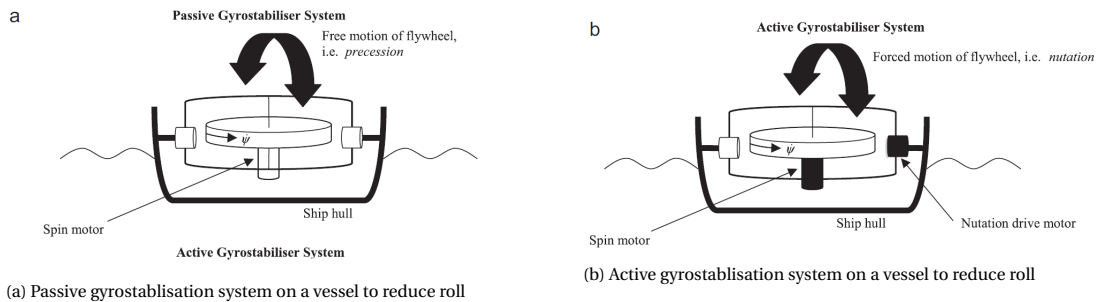


Figure 1.1: Illustration of active and passive gyroscopic stabilisation system on a vessel [33]

Control moment gyroscopes can create a larger moment with respect to reaction wheels with any given amount of momentum capacity that the rotating disk can store, [36]. The largest active gyrostabiliser ever installed on a vessel was on an Italian luxury liner weighing 41000 *tonne* and went by the name of *Conte Di Davaia*, [12]. This gyrostabiliser was able to reduce the vessel roll with 60% and only weighed 1.72% of the total weight of the vessel, [12]. Even though the control moment gyroscope is more powerful than a reaction wheel, the power required to provide the torque is also less than a reaction wheel with the same amount of angular momentum, [36]. A small downside of the control moment gyroscope is that the elaborate equations of motion have to be incorporated in the controller as well as the *Euler angles*. This is not only making the physical structure more complex due to the use of a gimbal but also the controller.

1.2. RESEARCH OBJECTIVES

In the following section the main research objective is presented together with the sub research objectives. The main research objective is stated below:

Optimize the workability of offshore installations of monopiles by using gyroscopic motion actuators.

The following sub-objectives need to be carried out to be able to realize the main objective:

1. *Determine best suitable gyroscope actuator system to control excessive motions of a monopile suspended on a crane.*
2. *Set up the computer model of the monopile, gyrostabilizer, gripper and crane system.*
3. *Determine eigenfrequency of the total system.*
4. *Add a wave spectrum that include the eigenfrequencies of the system.*
5. *Create controller for the gyrostabilisation system and incorporate it into the complete model to test effect.*

1.3. THESIS OUTLINE

To answer the research question and find out if and how a control moment gyroscope can be used to optimize workability of monopile installations, the flowchart given in Figure 1.2 is used. The theory behind each step is given in Chapter 2.

First the equations of motion are determined. This is done using the Lagrange method (1). Second, is where the highly nonlinear equations of motion are linearized (2). After they are linearized the equations are rewritten in state space format (3). The eigenfrequencies are calculated and are then compared and validated (5) against a model built in OrcaFlex (4). A controller will be built (6) and is then integrated in OrcaFlex (7) to see if a generated moment can compensate the movement of the monopile due to waves. From these results a worst case scenario will be encountered which gives the highest angle and thus the greatest moment to counteract (8). This moment is then used to dimension the CMG so that it can apply a force greater than or at least equal to this moment (11). The equations of motion of a CMG are used for this dimensioning (10). This newly created CMG will then be included into the controller that is used to counter the displacement of the monopile due to the waves (12). The numbers that are given correspond to the numbers in the Figure 1.2. The sections in the report that elaborate on these topics are given in Table 1.1.

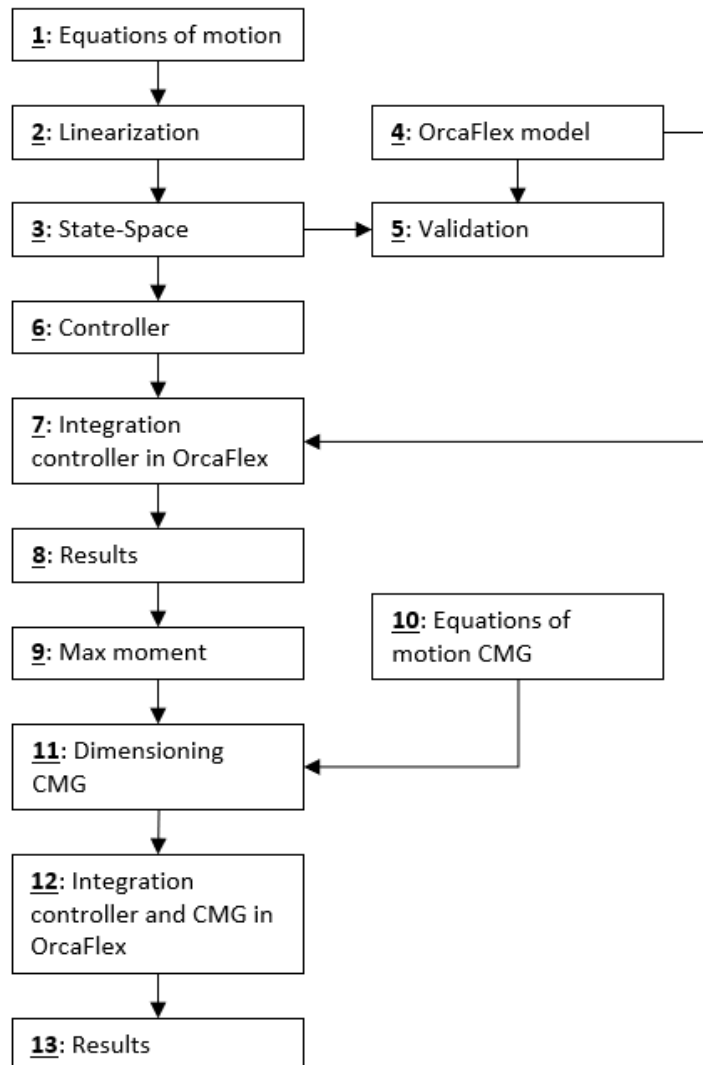


Figure 1.2: Flowchart of the steps taken to answer the research question

Table 1.1: Blocks given in Figure 1.2 with the corresponding sections

Block number(s)	Discription	Section
1	Equations of motion	3.1.1
2	Linearization	3.1.2
3	The state space model	3.1.3
4	The OrcaFlex model	3.2.4
5	Comparison and validation	3.2.5
6	The controller	3.4.1
7 - 9	Integration of the controller and results	3.4.2
10	Equations of motion CMG	3.5.1
11	required dimension of the CMG	3.5.2
12, 13	Final results	4

Following the aforementioned steps will show that a CMG can be used to minimize motions of the monopile due to waves. Thus, increasing workability allowing installation to continue in seastates with a higher H_s . Which in its turn will allow monopile foundations to be installed in less time decreasing the cost of installation.

2

REQUIRED THEORY FOR MODELLING OF A MECHANICAL SYSTEM

In this chapter the methods and theory used throughout the rest of the thesis will be explained. First the Lagrange method will be discussed. After which the transition from nonlinear to linear equations of motion is explained in more detail. Furthermore, the state space system is discussed which is constructed using the linear equations of motion.

2.1. MATHEMATICAL MODEL

2.1.1. LAGRANGIAN MECHANICS

The first step in modelling a mechanical system is to construct the equations of motion. In this case the Lagrange method will be used. Lagrange makes use of the concept of energy which can be determined by integrating power over time. If a force is applied on a rigid body in a one-dimensional situation the power is determined by multiplying force and velocity as shown in Equation 2.1, [35].

$$P = F\dot{x} \quad (2.1)$$

As mentioned above taking the integral over time gives the energy applied by that force as stated in Equation 2.2.

$$E = \int P dt = \int F\dot{x} dt \quad (2.2)$$

When Newton's equation of motion is used to describe the motion of an object which is then multiplied by the velocity and integrated over time, the result will state the energy equation of that particular system. This is shown in the equations 2.3 to 2.5.

$$\int F\dot{x} dt = \int m\ddot{x}\dot{x} dt \quad (2.3)$$

$$\int F \frac{dx}{dt} dt = \int m \frac{d\dot{x}}{dt} \dot{x} dt \quad (2.4)$$

$$\int F dx = \int m\dot{x} d\dot{x} \quad (2.5)$$

Working out the integral for a constant force for simplicity reasons gives the following Equation 2.6 where C is an integration constant.

$$Fx = \frac{1}{2} m\dot{x}^2 + C \quad (2.6)$$

Next is to set the potential energy function V as shown in Equation 2.7.

$$\frac{\partial V}{\partial x} = -F \quad (2.7)$$

When again assuming a constant force, the potential energy function can be written as $V = -Fx$. The kinetic energy T of the object in motion is mentioned in Equation 2.8, [35].

$$T = \frac{1}{2} m \dot{x}^2 \quad (2.8)$$

Substituting the kinetic energy and the potential energy in to Equation 2.6 will lead to Equation 2.9. Which states that the sum of potential en kinetic energy in a (conservative) system is constant, [35].

$$T + V = C_e \quad (2.9)$$

In order to use the same principles from a 1D case and a single mass for a rigid body with multiple degrees of freedom the equations are generalized, [35]. The kinetic energy then becomes as shown in Equation 2.10.

$$T = \frac{1}{2} \dot{x}_i \dot{x}_j M_{ij} \quad (2.10)$$

With

$$\dot{x}_i = (\dot{x}_b, \dot{y}_b, \dot{\psi}_b), \quad M_{ij} = \begin{bmatrix} m_b & 0 & 0 \\ 0 & m_b & 0 \\ 0 & 0 & I_b \end{bmatrix}, \quad b = 1 \dots N, \quad i, j = 1 \dots n \quad (2.11)$$

The potential energy function is constructed using the conservative forces acting on the system, e.g. gravity, while the non-conservative forces are collected and named F_i . The next step to get the equations of motion is to differentiate with respect to the coordinates, as Equation 2.12 shows. This is in line with the integration done before was with respect to the displacement of those coordinates, $dx_i = \dot{x}_i dt$, [35].

$$\underbrace{-\frac{\partial V}{\partial x_i} + F_i}_{\text{Applied forces}} = \underbrace{\frac{d}{dt} \left(\frac{\partial T}{\partial \dot{x}_i} \right)}_{\text{Inertia terms}} \quad (2.12)$$

As can be seen in Equation 2.12, the left hand side of the equation are the applied forces and the right hand side the inertial forces, exactly as before in Equation 2.5, [35]. This equation states the equation of motion with respect to its centre of mass position, orientation and velocity. However, the goal is to get the equation of motion in the generalized coordinates. Generalized coordinates are a set of coordinates that can define the position of a system uniquely relative to the initial position. The minimum number of generalized coordinates needed to describe a system in this manner is the *number of degrees of freedom*, [13]. The first step is to express the coordinates in terms of the generalized coordinates, assuming this is possible. Mathematically presented in Equation 2.13.

$$x_i = x_i(q_j), \quad i = 1 \dots n, \quad j = 1 \dots n_d \quad (2.13)$$

In Equation 2.13 n_d is the number of degrees of freedom. The velocities of the generalized coordinates are given in Equation 2.14.

$$\dot{x}_i = \frac{\partial x_i}{\partial q_j} \dot{q}_j \quad (2.14)$$

Using the aforementioned generalized coordinates, the kinetic and potential energy can now also be expressed in these terms.

$$T = T(\dot{x}_i) = T(q_j, \dot{q}_j) \quad (2.15)$$

$$V = V(x_i) = V(q_j) \quad (2.16)$$

Now to get to the generalized forces Q_j the definition of virtual power is used, which is $\delta P = Q_j \delta \dot{q}_j$ together with Equation 2.13, [35]. Equation 2.17 and 2.18 show the steps to determine the final result in Equation 2.19. The symbol \forall used in these equations means "for all".

$$F_i \delta \dot{x}_i = Q_j \delta \dot{q}_j \quad \forall \quad \delta \dot{x}_i = \frac{\partial x_i}{\partial q_j} \delta \dot{q}_j \quad (2.17)$$

$$F_i \frac{\partial x_i}{\partial q_j} \delta \dot{q}_j = Q_j \delta \dot{q}_j \quad \forall \quad \delta \dot{q}_j \quad (2.18)$$

$$Q_j = F_i \frac{\partial x_i}{\partial q_j} \quad (2.19)$$

Using this knowledge the equations of motion from equations 2.12 are rewritten and substituted into Equation 2.19 as shown in 2.20, [35].

$$Q_j = \frac{\partial x_i}{\partial q_j} \left(\frac{d}{dt} \left(\frac{\partial T}{\partial \dot{x}_i} \right) + \frac{\partial V}{\partial x_i} \right) \quad (2.20)$$

The first term can be derived from the chainrule that is stated below in Equation 2.21. This is then rewritten in Equation 2.22 which is substituted into Equation 2.20 to get to Equation 2.23.

$$\frac{d}{dt} \left(\frac{\partial x_i}{\partial q_j} \frac{\partial T}{\partial \dot{x}_i} \right) = \frac{\partial x_i}{\partial q_j} \frac{d}{dt} \left(\frac{\partial T}{\partial \dot{x}_i} \right) + \frac{\partial T}{\partial \dot{x}_i} \left(\frac{\partial x_i}{\partial q_j} \right) \frac{d}{dt} \quad (2.21)$$

$$\frac{\partial T}{\partial \dot{x}_i} \left(\frac{\partial x_i}{\partial q_j} \right) \frac{d}{dt} = \frac{\partial x_i}{\partial q_j} \frac{d}{dt} \left(\frac{\partial T}{\partial \dot{x}_i} \right) - \frac{d}{dt} \left(\frac{\partial x_i}{\partial q_j} \right) \frac{\partial T}{\partial \dot{x}_i} \quad (2.22)$$

$$Q_j = \frac{d}{dt} \left(\frac{\partial x_i}{\partial q_j} \frac{\partial T}{\partial \dot{x}_i} \right) - \frac{d}{dt} \left(\frac{\partial x_i}{\partial q_j} \right) \frac{\partial T}{\partial \dot{x}_i} + \frac{\partial V}{\partial q_j} \quad (2.23)$$

To further simplify Equation 2.23 and to fully express it in generalized coordinates it has to be determined that the partial derivatives of the coordinates and the velocities is equal to each other. First step is to take the partial derivative of Equation 2.14 with respect to \dot{q}_j shown in Equation 2.24.

$$\frac{\partial \dot{x}_i}{\partial \dot{q}_j} = \frac{\partial}{\partial \dot{q}_j} \left(\frac{\partial x_i}{\partial q_j} \dot{q}_j \right) = \frac{\partial x_i}{\partial q_j} \quad (2.24)$$

The time derivative of the partial derivatives can be rewritten in the manner that is shown in Equation 2.25, [35].

$$\frac{d}{dt} \left(\frac{\partial x_i}{\partial q_j} \right) = \frac{\partial}{\partial q_k} \left(\frac{\partial x_i}{\partial q_j} \right) \dot{q}_k \quad (2.25)$$

Using the fact that the second order derivatives are symmetric they can be rewritten as Equation 2.26

$$\frac{\partial}{\partial q_k} \left(\frac{\partial x_i}{\partial q_j} \right) = \frac{\partial}{\partial q_j} \left(\frac{\partial x_i}{\partial q_k} \right) \quad (2.26)$$

Substitution of equations 2.24 (in this case using q_k and \dot{q}_k instead of q_j and \dot{q}_j) and 2.26 into Equation 2.25 is shown below with the final result in Equation 2.29. This equation determines that the time derivative of the velocities are equal to the partial derivatives of the velocities.

$$\frac{d}{dt} \left(\frac{\partial x_i}{\partial q_j} \right) = \frac{\partial}{\partial q_j} \left(\frac{\partial x_i}{\partial q_k} \right) \dot{q}_k \quad (2.27)$$

$$\frac{\partial}{\partial q_j} \left(\frac{\partial x_i}{\partial q_k} \right) \dot{q}_k = \frac{\partial \dot{q}_k}{\partial q_j} \left(\frac{\partial \dot{x}_i}{\partial \dot{q}_k} \right) = \frac{\partial \dot{x}_i}{\partial q_j} \quad (2.28)$$

$$\frac{d}{dt} \left(\frac{\partial x_i}{\partial q_j} \right) = \frac{\partial \dot{x}_i}{\partial q_j} \quad (2.29)$$

The final step to get the Lagrange equations of motion is to substitute equations 2.24 and 2.29 into Equation 2.23. This substitution is shown in Equation 2.30 and the end result is Equation 2.31.

$$Q_j = \frac{d}{dt} \left(\frac{\partial x_i}{\partial q_j} \frac{\partial T}{\partial \dot{x}_i} \right) - \frac{d}{dt} \left(\frac{\partial x_i}{\partial q_j} \right) \frac{\partial T}{\partial \dot{x}_i} + \frac{\partial V}{\partial q_j} = \frac{d}{dt} \left(\frac{\partial \dot{x}_i}{\partial \dot{q}_j} \frac{\partial T}{\partial \dot{x}_i} \right) - \frac{\partial \dot{x}_i}{\partial q_j} \frac{\partial T}{\partial \dot{x}_i} + \frac{\partial V}{\partial q_j} \quad (2.30)$$

$$\frac{d}{dt} \left(\frac{\partial T}{\partial \dot{q}_j} \right) - \frac{\partial T}{\partial q_j} + \frac{\partial V}{\partial q_j} = Q_j, \quad j = 1, \dots, n_d \quad (2.31)$$

2.1.2. LINEARIZATION OF THE EQUATIONS OF MOTION

The equations of motion of a system can be highly non linear even for something as simple as a pendulum. However, in order to create and tune a controller it is more convenient to work with equations that are linear. This section will elaborate on the linearization of a general system in order to make handling these equations of motion easier. This short elaboration is based on the book Mechanical Vibrations: Theory and Application to Structural Dynamics by Geradin and Rixen [11].

As stated before for a conservative system the total sum of the kinetic energy and the potential energy is constant as shown in Equation 2.9. In order to simplify the elaboration of the linearization of the equations of motion the origin of the generalized coordinate system is chosen to be in the equilibrium position. Thus, equilibrium position is at $q_s = 0$ with $s = 1 \dots n$ where n is the number of generalized coordinates and q_s is the deviation from the equilibrium position. The potential energy is defined up to a constant which at its equilibrium position is chosen to be equal to 0, to simplify the problem and for convenience of explaining the process, as shown in Equation 2.32 and illustrated in Figure 2.1, [11]. Note that the generalized forces can be highly non linear and thus more then one equilibrium position may exist.

$$V(q_s = 0) = 0 \quad (2.32)$$

In Figure 2.1 the total amount of energy is denoted as ϵ instead of C as it was before. Thus Equation 2.9 becomes Equation 2.33.

$$T + V = \epsilon \quad (2.33)$$

The definition of a local equilibrium position is given below and can also be seen in Figure 2.1.

“The equilibrium position $q_s = 0$ is stable when an energy bound ϵ^* exists such that, for any energy $\epsilon < \epsilon^*$ given to the system, one has $T \leq \epsilon$ at any later instant, equality occurring only at equilibrium.” [11]

Figure 2.1 shows that any point near the equilibrium position $V \geq 0$. Due to the fact that the kinetic energy is a positive definite quantity the energy conservation will lead to the conclusion $0 \leq V \leq \epsilon$ meaning that if the initial energy given to the system is small any deviation from the equilibrium position will also be small, [11].

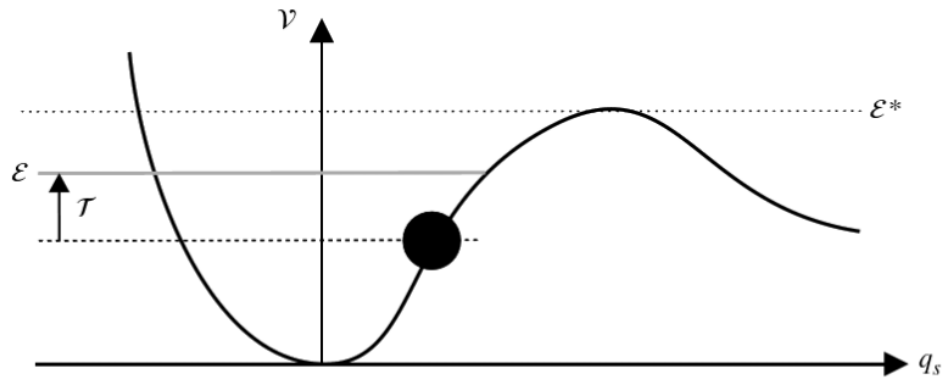


Figure 2.1: Potential energy of a locally stable system, [11]

To get the linearized form of the potential energy the energy expression must be a quadratic expression in terms of the generalized displacements and their derivatives, [11]. This will lead to the generalized forces being linear. As mentioned before q_s is taken as the deviation from the equilibrium position and thus the Taylor series could be used to describe the equation in the proximity of the equilibrium position. The Taylor expansion is shown in Equation 2.34.

$$V(q) = V(0) + \sum_{s=1}^n \left(\frac{\partial V}{\partial q_s} \right)_{q=0} q_s + \frac{1}{2} \sum_{s=1}^n \sum_{r=1}^n \left(\frac{\partial^2 V}{\partial q_s \partial q_r} \right)_{q=0} q_s q_r + \mathcal{O}(q^3) \quad (2.34)$$

With $V(0) = 0$ as stated before and the derivative of the potential energy of the system $\frac{\partial V}{\partial q_s} = 0$ Equation 2.34 turns into Equation 2.35.

$$V(q) = \frac{1}{2} \sum_{s=1}^n \sum_{r=1}^n k_{sr} q_s q_r > 0 \quad \text{for} \quad q \neq 0 \quad (2.35)$$

Where the stiffness matrix elements k_{sr} are given by Equation 2.36

$$k_{sr} = k_{rs} = \left. \frac{\partial^2 V}{\partial q_s \partial q_r} \right|_{q_{eq}} \quad (2.36)$$

For the kinetic energy the linearized equations are obtained by expanding the coefficients of the quadratic form in the vicinity of $q_s = 0$.

$$T(\dot{q}, q) = \frac{1}{2} \sum_{s=1}^n \sum_{r=1}^n \left(\frac{\partial^2 T}{\partial \dot{q}_s \partial \dot{q}_r} \right) \dot{q}_s \dot{q}_r \quad (2.37)$$

$$= \frac{1}{2} \sum_{s=1}^n \sum_{r=1}^n \left(\frac{\partial^2 T}{\partial \dot{q}_s \partial \dot{q}_r} \right)_{q=0} \dot{q}_s \dot{q}_r + \mathcal{O}(\dot{q}^2, q) \quad (2.38)$$

$$(2.39)$$

The second order approximation then gives the linearized equations of the kinetic energy as shown in Equation 2.40

$$T(\dot{q}) = \frac{1}{2} \sum_{s=1}^n \sum_{r=1}^n m_{sr} \dot{q}_s \dot{q}_r \quad (2.40)$$

Where m_{sr} denotes the inertia matrix and is given in Equation 2.41

$$m_{sr} = m_{rs} = \left. \frac{\partial^2 T}{\partial \dot{q}_s \partial \dot{q}_r} \right|_{q_{eq}} \quad (2.41)$$

When each element of the mass matrix M and stiffness matrix K is calculated they are used to construct the matrices and describe the equations of motion as stated in Equation 2.42 with the matrices shown in 2.43.

$$M\ddot{q} + D\dot{q} + Kq = F \quad (2.42)$$

$$M = \begin{bmatrix} m_{11} & \cdots & m_{1r} \\ \vdots & \ddots & \vdots \\ m_{s1} & \cdots & m_{sr} \end{bmatrix} \quad K = \begin{bmatrix} k_{11} & \cdots & k_{1r} \\ \vdots & \ddots & \vdots \\ k_{s1} & \cdots & k_{sr} \end{bmatrix} \quad (2.43)$$

If there are terms in the Lagrange equation dependent on a velocity, such as damping terms or gyroscopic terms, then the damping matrix is formed using both terms from Equation 2.31. This will be called f_T and is shown in Equation 2.44. The damping matrix is then formed using Equation 2.45

$$f_T = \frac{d}{dt} \frac{\partial T}{\partial \dot{q}} - \frac{\partial T}{\partial q} \quad (2.44)$$

$$d_{sr} = d_{rs} = \left. \frac{\partial f_T}{\partial \dot{q}_s} \right|_{q_{eq}} \quad (2.45)$$

2.1.3. STATE SPACE

Once the equations of motion have been linearized it is time to put them into a state space form. This method is a useful way of representing the equations of motion in a structured way.

The equations of motion in general form are given in equations 2.46 and 2.47, [10].

$$M\ddot{q} + D\dot{q} + Kq = F \quad (2.46)$$

$$y = C_{oq}q + C_{ov}\dot{q} \quad (2.47)$$

In Equation 2.46 q is the displacement vector with dimensions $n_d \times 1$, where n_d is equal to the number of degrees of freedom of the system. The velocity vector which has the same dimensions is called \dot{q} . The input vector is denoted by u and has dimensions $s \times 1$ where s is the number of inputs. y is the output vector with size $r \times 1$, where r denotes the number of outputs. The output displacement matrix and the output velocity matrix both with dimensions $r \times n_d$ are C_{oq} and C_{ov} , respectively. The mass matrix M is a diagonal matrix, the stiffness and damping matrices are K and D , respectively, [10].

The goal is to write Equation 2.46 and 2.47 in state space form. A state space is a linear time invariant system that describes the equations of motion with the linear coefficient differential equation shown in equations 2.48, [10]. In the state space form the A matrix is the state matrix, B is the input matrix and C is the output matrix and D_{ss} is the feedforward/feedthrough matrix. The x and u are the state and input vector, respectively.

$$\dot{x} = Ax + Bu \quad (2.48)$$

$$y = Cx + D_{ss}u \quad (2.49)$$

The first step to rewrite Equation 2.46 is isolate \ddot{q} which means dividing the equation by M , giving Equation 2.50

$$\ddot{q} + M^{-1}D\dot{q} + M^{-1}Kq = M^{-1}B_0u \quad (2.50)$$

The next step is to determine the state vector. A state vector is consists of the minimal number of physical variables that describe the motion of a system. This implies that using these variables an output can be uniquely determined when using a specified input, [10]. For a structure, displacements and velocities of the masses are needed to determine such a unique outcome. In Equation 2.51 state vector x is determined where q are the displacements and \dot{q} are the velocities, [10].

$$x = \begin{pmatrix} x_1 \\ x_2 \end{pmatrix} = \begin{pmatrix} q \\ \dot{q} \end{pmatrix} \quad (2.51)$$

Equation 2.51 can then be used to rewrite Equation 2.50 and essentially lowering the order of the equation from second to first as shown in equations 2.53 and 2.54.

$$\dot{x}_1 = x_2, \quad (2.52)$$

$$\dot{x}_2 = -M^{-1}Dx_2 - M^{-1}Kx_1 + M^{-1}B_0u \quad (2.53)$$

$$y = C_{oq}x_1 + C_{ov}x_2 \quad (2.54)$$

$$A = \begin{bmatrix} 0 & I \\ -M^{-1}K & -M^{-1}D \end{bmatrix}, \quad B = \begin{bmatrix} 0 \\ M^{-1}B_0 \end{bmatrix} \quad C = [C_{oq} \quad C_{ov}] \quad (2.55)$$

Filling in these equations in to Equation 2.48 will give the final state space representation shown in Equation 2.56

$$\begin{pmatrix} \dot{x}_1 \\ \dot{x}_2 \end{pmatrix} = \begin{bmatrix} 0 & I \\ -M^{-1}K & -M^{-1}D \end{bmatrix} \begin{pmatrix} x_1 \\ x_2 \end{pmatrix} + \begin{bmatrix} 0 \\ M^{-1}B_0 \end{bmatrix} u \quad (2.56)$$

$$y = [C_{oq} \quad C_{ov}] \begin{pmatrix} x_1 \\ x_2 \end{pmatrix} \quad (2.57)$$

Where The A matrix has dimensions of $N \times N$, The B matrix size is $N \times s$ and C is a $r \times N$ matrix. Where N is always $2n_d$: Twice the amount of degrees of freedom.

In Appendix A the example of a simple pendulum is given that takes the same steps as discussed in this chapter for a single degree of freedom system. The same steps have been done in Appendix B which elaborates on the pendulum on a cart which is a two degrees of freedom system.

2.2. CONTROL

The classical PID-controller is one of the most used controllers in the industry due to its relatively straightforward mode of operations all while delivering sufficient performance results [23]. It is important to know the different properties of the PID-controller in order to properly tune a controller. Therefore this section will discuss the PID-controller in more detail and the tuning method used. This is done following the method described in [23]. A Simple example is used to show the effects of the controller in Appendix F using the cart pendulum that was discussed in Appendix B.

2.2.1. STANDARD PID-CONTROLBLOCK DIAGRAM

In Figure 2.2 the standard control block is shown including the PID-controller showing its individual parts. The state space block is the mathematical model that describes the behaviour of the physical system. This is described earlier in this chapter. The reference signal r_0 is the desired value of the controlled variable. E.g. a position or a velocity of an object. The error signal e is the reference signal minus the actual value of the controlled variable. The error signal serves as input for the PID-controller for which the controller tries to minimize the error. It does this with three distinct elements within the controller. These elements are proportional, integrator and the differentiator. The amount that each elements contributes to the controller output u can be determined by their individual gains which are denoted by K_p , K_i and K_d for the proportional, integration and differential gains, respectively. The controller output is also the input for the aforementioned state space system, which is also called the 'plant' in a control block diagram. The controller output depends on the input variable chosen in a state space system. In most cases this is a force which is exerted on an object in order to control its position/velocity.

A PID-controller is defined by the relationship of the input error e and the output of the controller u . They can be expressed in time, frequency and Laplace domain. The time domain controller output is defined by Equation 2.59. Using the *Laplace-transform* the equation can be written in the laplace domain. The Laplace-transform for a derivative F_d and an integral F_i are given in Equation 2.58 [23]. While the integral transformation includes the initial value of $-e(0)$ in practice this term is often neglected in dynamical analysis. This is due to the fact that the frequency response functions, from which these equation are derived using the Laplace-transform, depend on a continuous input signal being present[23]. The Laplace domain expression is shown in Equation 2.60.

$$F_i(s) = \mathcal{L} \left\{ \int_0^{t'} e(t) dt \right\} = \frac{e(s)}{s} \quad F_d(s) = \mathcal{L} \left\{ \frac{de(t)}{dt} \right\} = se(s) - e(0) \quad (2.58)$$

$$u(t) = K_p e(t) + K_i \int_0^t e(\tau) d\tau + K_d \frac{de(t)}{dt} \quad (2.59)$$

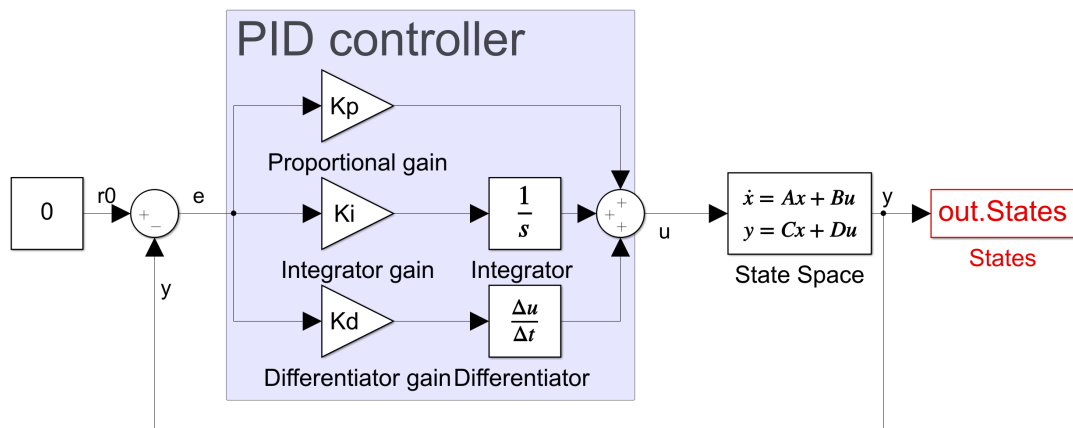


Figure 2.2: Block diagram PID-control system

$$u(s) = e(s) \left(K_p + \frac{K_i}{s} + K_d s \right) \quad (2.60)$$

$$C_{pid}(s) = \frac{u(s)}{e(s)} = K_p + \frac{K_i}{s} + K_d s$$

Using Equation 2.61 the time domain Equation 2.59 can be transformed to the frequency domain Equation 2.62. This is done by means of *Fourier transform*. Again, the standard results for the Fourier transform for a derivative $F_d(\omega)$ and an integral $F_i(\omega)$ is given in Equation 2.61 [23].

$$F_i(\omega) = \mathcal{F} \left\{ \int_0^{t'} e(t) dt \right\} = \frac{e(\omega)}{j\omega} \quad F_d(\omega) = \mathcal{F} \left\{ \frac{de(t)}{dt} \right\} = j\omega e(\omega) \quad (2.61)$$

$$C_{pid}(\omega) = \frac{u(\omega)}{e(\omega)} = K_p + \frac{K_i}{j\omega} + j\omega K_d \quad (2.62)$$

Now that the equations for a PID-controller are known a closer look is taken at the individual parts of the equations: proportional part K_p , and integral part K_i and differential part K_d .

2.2.2. PROPORTIONAL CONTROLLER

The proportional part of a PID-controller, Equation 2.63, in a mechanical system acts as a virtual spring as it adds a certain stiffness to the system. Where K_p is the proportional gain. The gain simply amplifies the error input such that the output is the error multiplied by the proportional gain i.e. the controller exerts more force as the error becomes larger. Therefore, the comparison of the proportional part to a spring is a valid one since a spring exerts more force the larger the deviation/distance is from its resting position.

$$u(t) = K_p e(t) \quad (2.63)$$

When only a proportional controller is used the value of the gain is the total gain K_t shown in Equation 2.64. This is equal to the inverse gain $G(\omega)$ of the plant at the desired bandwidth frequency f_c , also known as the unity-gain crossover frequency [23]. The cross-over frequency can thus be chosen or is a value given due to the operational limits of actuators e.g. actuator of which its maximum frequency is a physical constraint.

$$K_t = -\frac{1}{G(\omega)} \quad (2.64)$$

It is worth noting that for the total PID-controller this total gain is just a preliminary value for the proportional gain. This will be discussed in Section 2.2.5

2.2.3. INTEGRAL CONTROLLER

The integral part of the controller K_i , Equation 2.65, has no mechanical counterpart that it can be compared to. The integrating part helps to increase the controller gain at low frequencies and achieve a zero steady-state error.

$$u(t) = K_i \int_0^t e(\tau) d\tau \quad (2.65)$$

It does this by taking the integral of the error over time. This works because when the error is close to zero the proportional gain is low. However, the integral part can still be a non zero value due to the time that the error was not zero. This can cause an overshoot when the integral gain is not properly tuned. Due to the fact that even though the actual error might be at zero the value of the error integrated up to that point might still be a non zero value and thus the controller keeps applying force to make up for it. An important aspect to keep track of is that a integration in the frequency domain causes a phase shift of 90° (phase lag). This is due to the term $j\omega$ in the denominator of the frequency domain Equation 2.62.

2.2.4. DIFFERENTIAL CONTROLLER

The differentiating part, Equation 2.66, can be compared to a damper in a physical system. The reason for this is that the differential action is proportional to the derivative of the error at a single point in time. When the error grows fast it has a large derivative and therefore the amount the differentiating part contributes to the total controller output is large, i.e. the differential part tells the controller to give a larger output when the error is increasing rapidly and less force when the error is decreasing rapidly in order to avoid overshooting. Substitution of the rate at which the error changes with the rate the position changes (velocity) connected to a damper and the comparison between the differentiator and damper becomes clear. The faster the mass goes the more force the damper exerts in the opposite direction.

$$u(t) = K_d \frac{de(t)}{dt} \quad (2.66)$$

As the differentiating action makes sure there is less overshoot unlike the integrating action one has to make sure that the integrating and differentiating part should not have a large overlap in order to avoid nullifying their individual effect. While the integrating part adds a phase lag the differentiating part adds a phase lead.

2.2.5. PROPORTIONAL-INTEGRAL-DIFFERENTIAL CONTROLLER

Now that all the individual parts are discussed a closer look is taken at how the total controller performs and how the values for the individual gains should be determined. As explained in Section 2.2.2 the total gain should be determined at the cross-over frequency, f_c . Using this frequency the frequency at which the integrating action ends ω_i and where the differentiating frequency starts ω_d can be calculated. This is shown in equations 2.68 and 2.67. Note that these values are also converted to radians per second. As can be seen the integrating frequency ends at $0.1f_c$ while the differentiating frequency starts at $0.33f_c$. These are the 'guidelines' described in 'The design of high performance mechatronics : high-tech functionality by multi-disciplinary system integration' [23].

$$\omega_d = \frac{2\pi f_c}{3} \quad (2.67)$$

$$\omega_i = 2\pi \cdot 0.1 \cdot f_c \quad (2.68)$$

Now that the frequencies are known they can be used in order to finally come up with the values for the individual gains. The total gain determined in Section 2.2.2 is used for the proportional gain when a full PID-controller is used to control a system. As can be seen in Equation 2.69 this is one third the value of the cross-over gain.

$$K_p = \frac{K_t}{3} \quad (2.69)$$

The integral gain should start at low frequencies and stop working at higher frequencies. Determining a value for the integrating gain K_i is done using Equation 2.70.

$$K_i = K_p \omega_i \quad (2.70)$$

The differentiating action gain is computed using Equation 2.71. As can be seen they are all a function of the total gain and the frequency. The reason for this is that the total gain of the whole controller should be equal to the total gain K_t at the cross-over frequency. That is why the proportional gain is not equal to K_t because the differentiating gain is also contributing at this frequency. Together they will add up to be equal to K_t at this frequency. This is also illustrated in Figure 2.3 where all the frequencies and effects of each individual part of the PID-controller is shown. In this figure it is clear that the integrator works at the low frequencies where the control curve has a -1 slope and the effectiveness of the integrator diminishes towards the integrator frequency f_i . The small section that is relatively straightened is mostly governed by the proportional part of the controller until the defined differentiating frequency f_d . This is where the effect of the differentiator will start to govern the controllers behaviour as can be seen by the +1 line. The 'tamed' part is not used in this thesis and therefore will not be discussed.

$$K_d = \frac{K_p}{\omega_d} \quad (2.71)$$

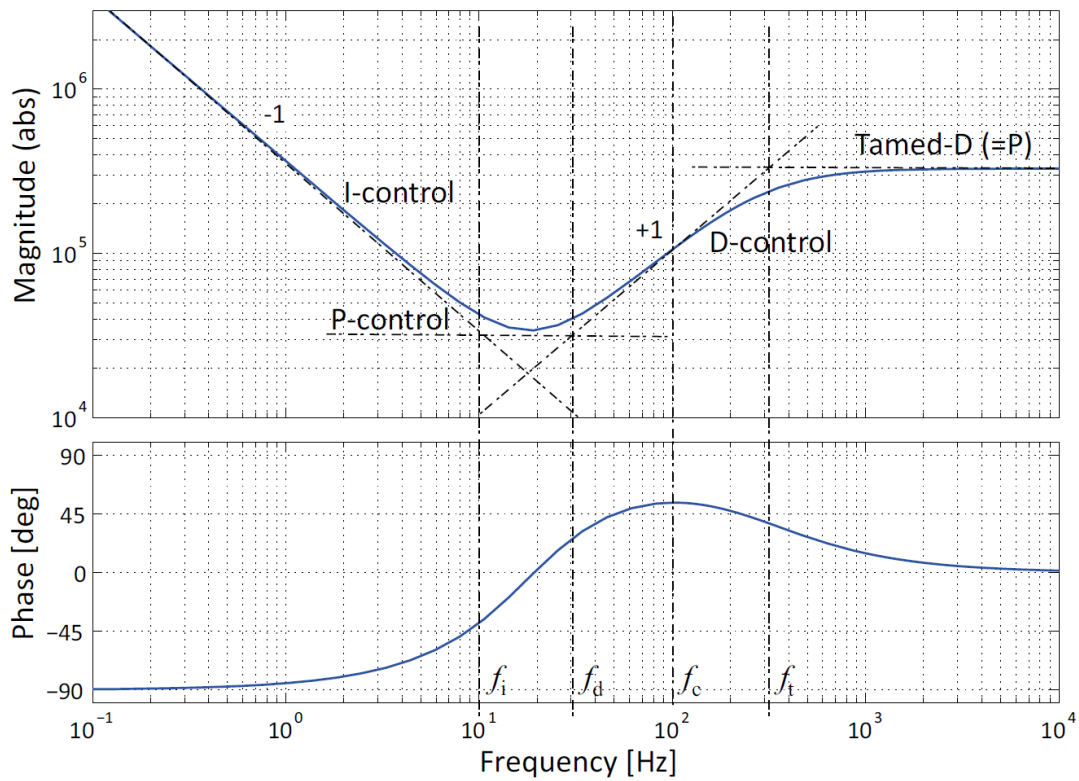


Figure 2.3: Bode plot of a PID-controller

2.3. WAVES

This section will discuss how waves are generated physically as well as how they are modelled in the software package that has been used for this thesis (OrcaFlex). It will also elaborate on the used sea state and wave spectrum.

2.3.1. WAVES

As described in the introduction a cause of excessive motions of the monopile during lowering is due to wave loading. The type of wave the monopile is subjected to depends on its geographical location as this effects the factors that create the waves. These factors are listed below.

Waves are influenced by the following five aspects [38]:

- Wind speed relative to the waves
- Fetch: The distance the wind can act on the water surface over an uninterrupted distance without a significant change in the wind direction
- Water depth
- Wind duration
- Width of the area perpendicular to fetch

There are 2 distinct type of waves: wind and "swell" waves. Wind waves are waves that are mostly dominant in locations that are sheltered from oceans such as the North Sea which is cut off from the Atlantic ocean by Great-Britain. The other type of waves are "swell" waves. One of the places these can be found is on the Atlantic coastline of France. These swell waves are generated by distant weather systems. A distant storm creates waves which travel a long distance dissipating energy by internal friction, air resistance and fanning (the divergence of the direction of propagation) [28]. The focus will be on wind waves as these are used in the simulations.

2.3.2. JONSWAP

A wave spectrum is a mathematical approach to describe the energy distribution of the waves at different frequencies. The aim of describing ocean waves as a spectrum is to describe the surface area as a stochastic process and not as a detail of one single observation, i.e. to represent all possible observations that could have been made during a time period during conditions of the actual observation [15].

The North Sea wave spectrum is described by the short wave JONSWAP spectrum [14]. JONSWAP is a acronym for Joint North Sea Wave Observation Project. This particular spectrum governed by wind waves as the North Sea is relatively sheltered from the oceans, i.e. the Atlantic ocean. The most important variables of a sea state are the significant wave height and the peak period: a certain H_s and corresponding T_p range. The significant wave height is the mean value of the highest third of the waves being sampled [1]. The T_p range given by by DNVGL for the wind sea spectrum (JONSWAP) is shown in Equation 2.72 [6]. If the natural periods of the monopile, crane and gripper system are within the upper and lower bounds resonance can occur. This can cause large motions of the monopile.

$$\sqrt{13H_s} < T_p < \sqrt{30H_s} \quad (2.72)$$

However, there is another variable involved which has an effect on the sea state. This is the peak enhancement factor or peakedness factor, γ . This is a method of fitting the wave spectrum to fit the actual waves spectrum measured [14]. Essentially, the JONSWAP spectrum is the Pierson-Moskowitz spectrum. Where the Pierson-Moskowitz spectrum is determined for a fully developed sea. However, in most situations a sea state is not fully developed and that is where the peak enhancement factor comes into play. The peakedness therefore helps describe an evolving sea state. The JONSWAP spectrum is the Pierson-Moskowitz multiplied by the peak enhancement factor [14]. This factor is thus dependent on the significant wave height as well as the peak period. In this thesis the method described by [5] is used to calculate the appropriate peakedness factor for each of the peak periods used of the corresponding significant wave heights. Equation 2.73.

$$\begin{aligned}
\gamma &= 5 \quad \text{for} \quad \frac{T_p}{\sqrt{H_s}} \leq 3.6 \\
\gamma &= e^{5.75 - 1.15 \frac{T_p}{\sqrt{H_s}}} \quad \text{for} \quad 3.6 < \frac{T_p}{\sqrt{H_s}} < 5 \\
\gamma &= 1 \quad \text{for} \quad 5 \leq \frac{T_p}{\sqrt{H_s}}
\end{aligned} \tag{2.73}$$

A higher H_s has more energy in a wave than a lower H_s . If the systems eigenperiods fall within the T_p range with a high H_s large displacements are to be expected which can, as previously stated, have a large impact on the allowable sea state and thus installation time.

The offshore wind energy field is developing monopiles that get bigger and heavier, thus lowering the natural frequency of the lowering system. Lowering of the natural frequencies means that there will be overlap with the wave frequencies.

2.3.3. MORISON

The Morison equations are a pretty straight forward approach to predict the wave forces that are applied on a pile vertically submerged in water. This is done by super imposing the inertia force and the drag force to get the total force on the pile. The equation is given in Equation 2.74. The total force on the pile F_{waves} is dependent on the density of the fluid ρ , the diameter of the pile D_{mp} , the velocity u_f and its derivative the acceleration of the fluid \dot{u} as well as the inertia and the drag coefficients C_M and C_D , respectively. The inertia force is directly proportional to the acceleration while the drag force is proportional to the square of the velocity. This results in the fact that the force components are out of phase by 90 degrees when looking at the equation as a function of time.

$$F_{waves}(t) = \underbrace{\frac{\pi}{4} \rho C_M D_{mp}^2 \dot{u}_f(t)}_{\text{Inertia force}} + \underbrace{\frac{1}{2} \rho C_D D_{mp} u_f(t) |u_f(t)|}_{\text{Drag force}} \tag{2.74}$$

C_M is determined by Equation 2.75 where C_a is the added mass coefficient. With C_a for a cylinder equal to 1 [5].

$$C_M = 1 + C_a \tag{2.75}$$

Rewriting Equation 2.74 such that it is the total force instead of force per meter is done by multiplying the equation by the total submerged length of the pile L_{sub} . This is what is done in Equation 2.76. $\frac{\pi}{4} \rho D^2 L_{sub}$ is equal to the mass of the displaced volume of the pile and is labeled as M_m . Something similar can be done for the latter part of the equation where $D L_{sub}$ is equal to the area A_m . This substitution is shown in Equation 2.76.

$$\begin{aligned}
F_{waves}(t) &= \frac{\pi}{4} \rho C_M D_{mp}^2 \dot{u}_f(t) L_{sub} + \frac{1}{2} \rho C_D D_{mp} u_f(t) |u_f(t)| L_{sub} \\
&= C_M M_m \dot{u}_f(t) + \frac{1}{2} \rho C_D A_m u_f(t) |u_f(t)|
\end{aligned} \tag{2.76}$$

The equation for the total forces can also be written for a moving pile in the waves. Which is what will happen in the case that is being studied where the monopile is lowered through the wave zone. This is done as by taking the relative velocities and acceleration of the pile and using Equation 2.75 the equation is written in its simplest form. By doing this Equation 2.74 then transforms to Equation 2.77 in which subscript f denotes the fluid related variables and subscript b denotes the body (pile) related variables.

$$F_{waves}(t) = (C_M M_m \dot{u}_f(t) - C_a M_m \dot{u}_b(t)) + \frac{1}{2} \rho C_D A_m (u_f(t) - u_b(t)) |u_f(t) - u_b(t)| \tag{2.77}$$

The relative acceleration between the fluid and the body, denoted by subscript r is given by $\dot{u}_r = \dot{u}_f - \dot{u}_b$. Rewriting this equation in the form $\dot{u}_b = \dot{u}_f - \dot{u}_r$ and using Equation 2.75 to substitute the acceleration of the

body and the inertial coefficient, Equation 2.77 can be simplified. The relative velocity u_r is straight forward and is substituted by $u_r = u_f - u_b$. The steps are shown in Equation 2.78

$$\begin{aligned}
 F_{waves}(t) &= M_m (C_m \dot{u}_f(t) - C_a \dot{u}_f(t) + C_a \dot{u}_r(t)) + \frac{1}{2} \rho C_D A_m u_r(t) |u_r(t)| \\
 &= M_m (\dot{u}_f(t) + C_a \dot{u}_f(t) - C_a \dot{u}_f(t) + C_a \dot{u}_r(t)) + \frac{1}{2} \rho C_D A_m u_r(t) |u_r(t)| \quad (2.78) \\
 &= M_m (\dot{u}_f(t) - C_a \dot{u}_r(t)) + \frac{1}{2} \rho C_D A_m u_r(t) |u_r(t)|
 \end{aligned}$$

Morison is used in OrcaFlex to calculate the wave forces on the monopile. However, Morison is only accurate for certain diameter to wavelength ratios. The ratio for which the calculation method is valid is $D/\lambda < 0.1$ to 0.2 [17]. For larger ratios the results are exaggerating the force applied on the pile. Nonetheless, this is a fast and efficient method and can tell a lot about the trends and behaviour of the system. Especially when trying to determine if a control moment gyroscope is a valid possibility for the task of damping the motion of the monopile, which is based on a relative validation (directly comparing the case with and without gyroscope).

3

MODELLING

In this the chapter the equations of motion are derived using the Lagrange method stating any assumptions and constraints used in this derivation. Following this derivation of the equations of motion the linearization about the equilibrium position is shown. The construction of the state space model is then discussed after which the validity of the model is proven. This is done using OrcaFlex. This is done in steps of increasing complexity. First the monopile without added mass and trapped mass is considered. The next step is adding the added and trapped mass after which the equations of motion of the control moment gyroscope are derived and implemented in the equations. The final step that is discussed is the tuning of the controller.

3.1. MATLAB MODEL

3.1.1. EQUATIONS OF MOTION

In order to get the equations of motion of a monopile suspended from a crane and held by a gripper, the centre of gravity of the system and the inertia should be known. In Figure 3.1 a schematic representation is given including relevant dimensions that are needed to calculate the equations of motion. The origin is at the crane tip with the y -axis pointing into the paper. As can be seen in Figure 3.1 the system consists of the monopile and two springs representing the crane wire and the gripper.

The Lagrange method starts by determining the degrees of freedom (DOF). Next writing the potential and kinetic energy equations in terms of these DOF. For the system portrayed in Figure 3.1 the degrees of freedom are x , z and θ . Thus the generalized coordinates are as given in Equation 3.1 together with their derivatives.

$$q = \begin{bmatrix} x \\ z \\ \theta \end{bmatrix} \quad \dot{q} = \begin{bmatrix} \dot{x} \\ \dot{z} \\ \dot{\theta} \end{bmatrix} \quad \ddot{q} = \begin{bmatrix} \ddot{x} \\ \ddot{z} \\ \ddot{\theta} \end{bmatrix} \quad (3.1)$$

The kinetic energy, T_{total} , of the whole system is found by adding the kinetic energy in each direction as shown in Equation 3.2. Where the kinetic energy in x , z and rotational direction, θ , are given by 3.3, 3.4 and 3.5, respectively.

$$T_{total} = T_x + T_z + T_\theta \quad (3.2)$$

$$T_x = \frac{1}{2} m_x \dot{x}^2 \quad (3.3)$$

$$T_z = \frac{1}{2} m_z \dot{z}^2 \quad (3.4)$$

$$T_\theta = \frac{1}{2} I \dot{\theta}^2 \quad (3.5)$$

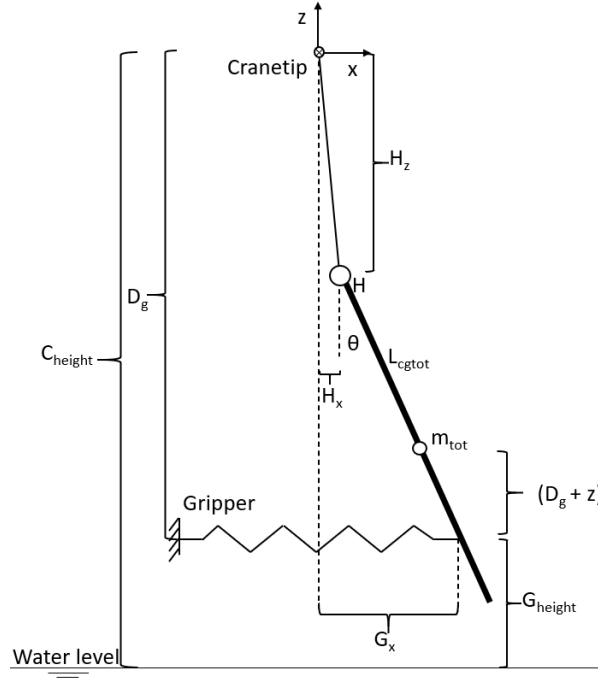


Figure 3.1: Schematic representation of the monopile suspended from the crane

The mass moment of inertia, I , in this case is just the inertia of the monopile around its centre of gravity. The following steps are taken in order to determine the wire elongation. This is required to properly set up the potential energy of the wire that will be modelled as a spring. The total length of the wire can be determined using Equation 3.6 after which the elongated part can be derived by subtracting the original length of the wire as shown in Equation 3.7

$$L_w = \sqrt{H_x^2 + H_z^2} \quad (3.6)$$

$$L_e = L_w - L_0 \quad (3.7)$$

The potential energy, V , is defined by gravity and the 2 springs. In Equation 3.8 the potential energy of the whole system is given.

$$V = m_z g z + \frac{1}{2} k_{wire} L_e^2 + \frac{1}{2} k_{gripper} G_x^2 \quad (3.8)$$

Where H_x is the position of the hook (where the crane wire attaches to the top of the lifting tool) in x -direction, H_z is the position in z -direction of this point and G_x is the position of where the gripper touches the monopile and can only move in the x direction. The equations are given below in equations 3.9, 3.10 and 3.11. Note that the x and z in the mentioned equations are the locations of the centre of gravity of the monopile.

$$H_x = x - L_{cgtot} \sin \theta \quad (3.9)$$

$$H_z = z + L_{cgtot} \cos \theta \quad (3.10)$$

$$G_x = x + (D_g + z) \tan \theta \quad (3.11)$$

With D_g as given in Equation 3.12 where C_{height} is the height of the crane tip and G_{height} the height of the gripper measured from sea level.

$$D_g = C_{height} - G_{height} \quad (3.12)$$

As explained in Chapter 2.1.1 the kinetic and potential energy that are constructed above will now be differentiated in order to get the equations of motion of the system. Using Equation 3.13.

$$\frac{d}{dt} \frac{\partial T}{\partial \dot{q}_i} - \frac{\partial T}{\partial q_i} + \frac{\partial V}{\partial q_i} = 0 \quad (3.13)$$

Equation 3.13 turns in to Equation 3.14 for $q_1 = x$ and taking the following steps results in the EOM for the x direction, 3.18.

$$\frac{d}{dt} \frac{\partial T}{\partial \dot{x}} - \frac{\partial T}{\partial x} + \frac{\partial V}{\partial x} = 0 \quad (3.14)$$

$$\frac{d}{dt} \frac{\partial T}{\partial \dot{x}} = m_x \ddot{x} \quad (3.15)$$

$$\frac{\partial T}{\partial x} = 0 \quad (3.16)$$

$$\frac{\partial V}{\partial x} = k_{gripper} G_x + \frac{k_{wire} L_e H_x}{L_w} \quad (3.17)$$

Substitute equations 3.15, 3.16 and 3.17 into Equation 3.14 to get the EOM in x -direction shown in Equation 3.18. Note that for the following equations for the derivatives in all degrees of freedom the end result is already stated in which the equation is written as concise as possible in order to keep a good understanding. However, Appendix D shows the full equations before being simplified by using substitution of terms.

$$m_x \ddot{x} + k_{gripper} G_x + \frac{k_{wire} L_e H_x}{L_w} = 0 \quad (3.18)$$

The same steps are now done for the z -direction EOM and are shown in equations 3.19 to 3.23.

$$\frac{d}{dt} \frac{\partial T}{\partial \dot{z}} - \frac{\partial T}{\partial z} + \frac{\partial V}{\partial z} = 0 \quad (3.19)$$

$$\frac{d}{dt} \frac{\partial T}{\partial \dot{z}} = m_z \ddot{z} \quad (3.20)$$

$$\frac{\partial T}{\partial z} = 0 \quad (3.21)$$

$$\frac{\partial V}{\partial z} = g m_z + k_{gripper} \tan \theta G_x + \frac{k_{wire} L_e H_z}{L_w} \quad (3.22)$$

Substitute equations 3.20, 3.21 and 3.22 into Equation 3.19 to get the EOM in z direction shown in Equation 3.23.

$$m_z \ddot{z} + g m_z + k_{gripper} \tan \theta G_x + \frac{k_{wire} L_e H_z}{L_w} = 0 \quad (3.23)$$

The last equation of motion is for the rotation with angle θ . The same steps apply as previously done for the other EOM. Equations 3.25, 3.26 and 3.27 into Equation 3.24 to get the EOM in θ direction shown in Equation 3.28

$$\frac{d}{dt} \frac{\partial T}{\partial \dot{\theta}} - \frac{\partial T}{\partial \theta} + \frac{\partial V}{\partial \theta} = 0 \quad (3.24)$$

$$\frac{d}{dt} \frac{\partial T}{\partial \dot{\theta}} = I \ddot{\theta} \quad (3.25)$$

$$\frac{\partial T}{\partial \theta} = 0 \quad (3.26)$$

$$\frac{\partial V}{\partial \theta} = - \frac{k_{wire} L_{cgtot} (H_x \cos \theta + H_z \sin \theta) L_e}{L_w} + k_{gripper} (D_g + z) G_x (\tan^2 \theta + 1) \quad (3.27)$$

$$I \ddot{\theta} - \frac{k_{wire} L_{cgtot} (H_x \cos \theta + H_z \sin \theta) L_e}{L_w} + k_{gripper} (D_g + z) G_x (\tan^2 \theta + 1) = 0 \quad (3.28)$$

3.1.2. LINEARIZATION OF THE EQUATION OF MOTION

Equations 3.18, 3.23 and 3.28 are highly non linear and thus the next step is to linearize these equations following the steps described in Section 2.1.2. Due to linearization around its equilibrium position the product terms where variables are multiplied by other variables (constants are acceptable) cancel out as well as any sine and tangent terms. The cosine terms will become 1. Exponential and square root terms involving variables (general coordinates) are also cancelled out.

To get the linearized mass matrix, Equation 2.41 is used and becomes Equation 3.31 for this system when differentiated around the equilibrium position. The equilibrium position for x and θ is equal to 0. However, the equilibrium position for z is $z = -(L_0 + L_{cgtot} + L_{0stretch})$. $L_{0stretch}$ is the elongation of the wire at rest (equilibrium position), Equation 3.30. This is the location of the centre of gravity of the system when at rest. When the general coordinates are at equilibrium position the vector, q_{eq} , is formed and is shown in 3.29

$$q_{eq} = \begin{bmatrix} 0 \\ -(L_0 + L_{cgtot} + L_{0stretch}) \\ 0 \end{bmatrix} \quad (3.29)$$

$$L_{0stretch} = \frac{m_z g}{k_{wire}} \quad (3.30)$$

$$M = \left. \frac{\partial^2 T}{\partial \dot{q}^2} \right|_{q_{eq}} \rightarrow M = \begin{bmatrix} m_x & 0 & 0 \\ 0 & m_z & 0 \\ 0 & 0 & I \end{bmatrix} \quad (3.31)$$

The entries of the stiffness matrix, based on the derivative given in Equation 2.36 are given in equations 3.32 to 3.40 per element.

$$k_{11} = \frac{\partial^2 V}{\partial q_1 \partial q_1} = \left(\frac{L_e}{L_w} + \frac{H_x^2}{L_w^2} - \frac{L_e H_x^2}{L_w^3} \right) k_{wire} + k_{gripper} \quad (3.32)$$

$$k_{12} = \frac{\partial^2 V}{\partial q_1 \partial q_2} = k_{gripper} \tan \theta + \left(\frac{k_{wire}}{L_w^2} - \frac{k_{wire} L_e}{L_w^3} \right) H_z H_x \quad (3.33)$$

$$k_{13} = \frac{\partial^2 V}{\partial q_1 \partial q_3} = k_{gripper} (D_g + z) (\tan^2 \theta + 1) \dots \\ + L_{cgtot} \left(-\frac{k_{wire} \cos \theta L_e}{L_w} - \frac{k_{wire} H_x (x \cos \theta + z \sin \theta)}{L_w^2} + \frac{k_{wire} L_e H_x (x \cos \theta + z \sin \theta)}{L_w^3} \right) \quad (3.34)$$

$$k_{21} = \frac{\partial^2 V}{\partial q_2 \partial q_1} = k_{gripper} \tan \theta + \left(\frac{k_{wire}}{L_w^2} - \frac{k_{wire} L_e}{L_w^3} \right) H_z H_x \quad (3.35)$$

$$k_{22} = \frac{\partial^2 V}{\partial q_2 \partial q_2} = \left(\frac{L_e}{L_w} + \frac{H_z^2}{L_w^2} - \frac{L_e H_z^2}{L_w^3} \right) k_{wire} + k_{gripper} \tan^2 \theta \quad (3.36)$$

$$k_{23} = \frac{\partial^2 V}{\partial q_2 \partial q_3} = \left(-\frac{\sin \theta L_e}{L_w} - \frac{H_z (x \cos \theta + z \sin \theta)}{L_w^2} + \frac{L_e H_z (x \cos \theta + z \sin \theta)}{L_w^3} \right) L_{cgtot} k_{wire} \dots \\ + k_{gripper} (\tan^2 \theta + 1) G_x + k_{gripper} \tan \theta (D_g + z) (\tan^2 \theta + 1) \quad (3.37)$$

$$k_{31} = \frac{\partial^2 V}{\partial q_3 \partial q_1} = k_{gripper} (D_g + z) (\tan^2 \theta + 1) \dots \\ + L_{cgtot} \left(-\frac{k_{wire} \cos \theta L_e}{L_w} - \frac{k_{wire} H_x (x \cos \theta + z \sin \theta)}{L_w^2} + \frac{k_{wire} L_e H_x (x \cos \theta + z \sin \theta)}{L_w^3} \right) \quad (3.38)$$

$$k_{32} = \frac{\partial^2 V}{\partial q_3 \partial q_2} = \left(-\frac{\sin \theta L_e}{L_w} - \frac{H_z (x \cos \theta + z \sin \theta)}{L_w^2} + \frac{L_e H_z (x \cos \theta + z \sin \theta)}{L_w^3} \right) L_{cgtot} k_{wire} \dots \\ + k_{gripper} (\tan^2 \theta + 1) G_x + k_{gripper} \tan \theta (D_g + z) (\tan^2 \theta + 1) \quad (3.39)$$

$$k_{33} = \frac{\partial^2 V}{\partial q_3 \partial q_3} = \left(\left(\frac{(x \cos \theta + z \sin \theta)^2}{L_w^2} - \frac{L_e (x \cos \theta + z \sin \theta)^2}{L_w^3} \right) L_{cgtot}^2 - \frac{L_{cgtot} L_e (z \cos \theta - x \sin \theta)}{L_w} \right) k_{wire} \\ + k_{gripper} (D_g + z)^2 (\tan^2 \theta + 1)^2 + 2 k_{gripper} \tan \theta (D_g + z) (\tan^2 \theta + 1) G_x \quad (3.40)$$

However, these equations are non linear. Once they are evaluated at the equilibrium position they will become linear. The linearized stiffness matrix is the square matrix shown in Equation 3.41. For readability the individual elements of the matrix are shown in equations 3.42 to 3.50. As can be seen the elements are linear.

$$K = \begin{bmatrix} k_{11} & k_{12} & k_{13} \\ k_{21} & k_{22} & k_{23} \\ k_{31} & k_{32} & k_{33} \end{bmatrix} \quad (3.41)$$

$$k_{11} = \left. \frac{\partial^2 V}{\partial q_1 \partial q_1} \right|_{q_{eq}} = k_{gripper} + \frac{k_{wire} L_{0stretch}}{L_0 + L_{0stretch}} \quad (3.42)$$

$$k_{12} = \left. \frac{\partial^2 V}{\partial q_1 \partial q_2} \right|_{q_{eq}} = 0 \quad (3.43)$$

$$k_{13} = \left. \frac{\partial^2 V}{\partial q_1 \partial q_3} \right|_{q_{eq}} = -\frac{L_{cgtot} k_{wire} L_{0stretch}}{L_0 + L_{0stretch}} - k_{gripper} (L_0 - D_g + L_{0stretch} + L_{cgtot}) \quad (3.44)$$

$$k_{21} = \left. \frac{\partial^2 V}{\partial q_2 \partial q_1} \right|_{q_{eq}} = 0 \quad (3.45)$$

$$k_{22} = \left. \frac{\partial^2 V}{\partial q_2 \partial q_2} \right|_{q_{eq}} = k_{wire} \quad (3.46)$$

$$k_{23} = \left. \frac{\partial^2 V}{\partial q_2 \partial q_3} \right|_{q_{eq}} = 0 \quad (3.47)$$

$$k_{31} = \left. \frac{\partial^2 V}{\partial q_3 \partial q_1} \right|_{q_{eq}} = -\frac{L_{cgtot} k_{wire} L_{0stretch}}{L_0 + L_{0stretch}} - k_{gripper} (L_0 - D_g + L_{0stretch} + L_{cgtot}) \quad (3.48)$$

$$k_{32} = \left. \frac{\partial^2 V}{\partial q_3 \partial q_2} \right|_{q_{eq}} = 0 \quad (3.49)$$

$$k_{33} = \left. \frac{\partial^2 V}{\partial q_3 \partial q_3} \right|_{q_{eq}} = k_{gripper} (L_0 - D_g + L_{0stretch} + L_{cgtot})^2 + \frac{L_{cgtot} k_{wire} L_{0stretch} (L_0 + L_{0stretch} + L_{cgtot})}{(L_0 + L_{0stretch})} \quad (3.50)$$

The MATLAB code used to create these matrices is shown in Appendix C in the linearization part.

3.1.3. STATE SPACE MODEL

Now that the linearized equations of motion are known the next step consists of rewriting the equations in state space form. As explained in Chapter 2.1.3 the first step is to isolate \ddot{q} as shown in Equation 3.52. The inverse matrix of M is given in Equation 3.51.

$$M^{-1} = \begin{bmatrix} \frac{1}{m_x} & 0 & 0 \\ 0 & \frac{1}{m_z} & 0 \\ 0 & 0 & \frac{1}{I} \end{bmatrix} \quad (3.51)$$

$$\ddot{q} = M^{-1} B_0 u - M^{-1} K q \quad (3.52)$$

The state vector is shown in Equation 3.53

$$\vec{x} = \begin{pmatrix} x_1 \\ x_2 \\ x_3 \\ x_4 \\ x_5 \\ x_6 \end{pmatrix} = \begin{pmatrix} q_1 \\ q_2 \\ q_3 \\ \dot{q}_1 \\ \dot{q}_2 \\ \dot{q}_3 \end{pmatrix} = \begin{pmatrix} x \\ z \\ \theta \\ \dot{x} \\ \dot{z} \\ \dot{\theta} \end{pmatrix} \quad (3.53)$$

the A and B matrix can be constructed using Equation 2.55.

$$A = \begin{bmatrix} 0 & 0 & 0 & 1 & 0 & 0 \\ 0 & 0 & 0 & 0 & 1 & 0 \\ 0 & 0 & 0 & 0 & 0 & 1 \\ -\frac{k_{11}}{m_x} & -\frac{k_{12}}{m_x} & -\frac{k_{13}}{m_x} & 0 & 0 & 0 \\ -\frac{k_{21}}{m_z} & -\frac{k_{22}}{m_z} & -\frac{k_{23}}{m_z} & 0 & 0 & 0 \\ -\frac{k_{31}}{I} & -\frac{k_{32}}{I} & -\frac{k_{33}}{I} & 0 & 0 & 0 \end{bmatrix} \quad (3.54)$$

The system is controlled by exerting a moment around the y -axis applied in the θ degree of freedom and thus the B matrix will look as shown in Equation 3.55.

$$B = \begin{bmatrix} 0 \\ 0 \\ 0 \\ 0 \\ 0 \\ \frac{1}{I} \end{bmatrix} \quad (3.55)$$

The C matrix is chosen so that all the displacements and velocities are given as out put of the system. Therefore, the C matrix is a 6x6 identity matrix.

$$C = \begin{bmatrix} 1 & 0 & 0 & 0 & 0 & 0 \\ 0 & 1 & 0 & 0 & 0 & 0 \\ 0 & 0 & 1 & 0 & 0 & 0 \\ 0 & 0 & 0 & 1 & 0 & 0 \\ 0 & 0 & 0 & 0 & 1 & 0 \\ 0 & 0 & 0 & 0 & 0 & 1 \end{bmatrix} \quad (3.56)$$

The full state space representation is shown in 3.57.

$$\begin{pmatrix} \dot{x}_1 \\ \dot{x}_2 \\ \dot{x}_3 \\ \ddot{x}_4 \\ \ddot{x}_5 \\ \ddot{x}_6 \end{pmatrix} = \begin{bmatrix} 0 & 0 & 0 & 1 & 0 & 0 \\ 0 & 0 & 0 & 0 & 1 & 0 \\ 0 & 0 & 0 & 0 & 0 & 1 \\ -\frac{k_{11}}{m_x} & -\frac{k_{12}}{m_x} & -\frac{k_{13}}{m_x} & 0 & 0 & 0 \\ -\frac{k_{21}}{m_z} & -\frac{k_{22}}{m_z} & -\frac{k_{23}}{m_z} & 0 & 0 & 0 \\ -\frac{k_{31}}{I} & -\frac{k_{32}}{I} & -\frac{k_{33}}{I} & 0 & 0 & 0 \end{bmatrix} \begin{pmatrix} x_1 \\ x_2 \\ x_3 \\ x_4 \\ x_5 \\ x_6 \end{pmatrix} + \begin{pmatrix} 0 \\ 0 \\ 0 \\ 0 \\ 0 \\ \frac{1}{I} \end{pmatrix} u \quad (3.57)$$

$$y = \begin{bmatrix} 1 & 0 & 0 & 0 & 0 & 0 \\ 0 & 1 & 0 & 0 & 0 & 0 \\ 0 & 0 & 1 & 0 & 0 & 0 \\ 0 & 0 & 0 & 1 & 0 & 0 \\ 0 & 0 & 0 & 0 & 1 & 0 \\ 0 & 0 & 0 & 0 & 0 & 1 \end{bmatrix} \begin{pmatrix} x_1 \\ x_2 \\ x_3 \\ x_4 \\ x_5 \\ x_6 \end{pmatrix} \quad (3.58)$$

3.2. MONOPILE SUSPENDED IN AIR

3.2.1. DETERMINING KEY VARIABLES

Now that we have the mathematical model, the dimensions of the actual physical system have to be determined. Here the case is shown when the monopile is suspended in the air and thus not partially submerged. Table 3.1 shows the used input values of the system that is depicted in Figure 3.1 together with the dimensions of the monopile itself. From these values all other terms can be calculated.

Table 3.1: The dimensions of the system are shown that are used in the mathematical model and OrcaFlex

Description	Abbreviation	Value	Unit
Height of cranetip above sealevel	C_{height}	150	m
Height of gripper above sealevel	G_{height}	10.0	m
Stiffness of gripper	$k_{grripper}$	$10 \cdot 10^6$	N/m
Length of monopile	L_{mp}	80.0	m
Unstretched length crane wire	L_0	75.0	m
Density of steel	ρ_{steel}	$7.85 \cdot 10^3$	kg/m^3
Wall thickness of monopile	t_{mp}	0.06	m
Diameter of monopile	D_{mp}	8.00	m
Stiffness of crane wire	k_{wire}	$37 \cdot 10^6$	N/m

The monopile is assumed to be a cylinder with an even thickness over its length. The mass of the weight is determined as follows in Equation 3.59. Because a homogeneous hollow cylinder is assumed in this case the center of gravity $L_{cg_{tot}}$ is at half the length of the monopile.

$$m_{mp} = \rho_{steel} \cdot A_{csm} \cdot L_{monopile} \quad (3.59)$$

Where A_{csm} is the cross-sectional area of the monopile and is given by Equation 3.60 where r_{out} and r_{in} are the outer and inner radius of the monopile, respectively.

$$A_{csm} = \pi (r_{out}^2 - r_{in}^2) \quad (3.60)$$

Using the values in Table 3.1 and equations 3.59 and 3.60 the mass can be determined. The inner and outer radius of the monopile can easily be determined but are stated for the sake of completeness in Equation 3.61.

$$r_{in} = \frac{D_{mp}}{2} - t_{mp} = 3.94m \quad (3.61)$$

$$r_{out} = \frac{D_{mp}}{2} = 4.00m$$

$$A_{csm} = 1.50m \quad (3.62)$$

$$m_{mp} = 9.40 \cdot 10^5 kg \quad (3.63)$$

Now the mass is known the inertia of the monopile can be calculated as shown in Equation 3.64, [2].

$$I_{mp} = \frac{1}{12} m_{mp} (3(r_{out}^2 + r_{in}^2) + L_{mp}^2) \quad (3.64)$$

$$I_{mp} = 5.09 \cdot 10^8 kg \cdot m^2 \quad (3.65)$$

The wire elongation due to gravity only ($L_{0stretch}$), i.e. when stationary in its equilibrium point, is calculated using Equation 3.66. As can be seen this is only dependent on the stiffness of the wire, k_{wire} , gravity, g , which is $9.81ms^{-2}$ and monopile mass, m_{mp} .

$$L_{0stretch} = \frac{m_{mp}g}{k_{wire}} = 0.25m \quad (3.66)$$

The distance from the cranetip to gripper, D_g , is determined by Equation 3.12 and is shown again in Equation 3.67.

$$D_g = C_{height} - G_{height} = 140m \quad (3.67)$$

Now it is also possible to determine the equilibrium position of the system. The positions of x and θ are trivial and are equal to 0. However, the z position is determined by Equation 3.68 which is dependent on the length of the wire (L_0) and its stationary elongation due to gravity ($L_{0stretch}$) and the distance from the hook to the centre of gravity of the system ($L_{cg_{tot}}$). The centre of gravity from the hook is half the length of the monopile, as mentioned before.

$$z_{eq} = -(L_0 + L_{cg_{tot}} + L_{0stretch}) = -115.25m \quad (3.68)$$

With these values all the other positions and velocities needed to compute the equations of motions can be determined. Once these values are substituted into the equations the eigenfrequencies of the system can be computed which are the natural frequencies of the system. These and other values can then be compared to the values of the OrcaFlex model to validate the mathematical model.

3.2.2. NATURAL FREQUENCIES OF MONOPILE SUSPENDED IN AIR

There are 3 distinct eigenfrequencies of the system that in general can be calculated using Equation 3.69. Where ω , K and M are the natural frequency in rad/s , stiffness matrix and mass matrix, respectively.

$$\omega = \sqrt{\frac{K}{M}} \quad (3.69)$$

The natural frequencies are shown for 2 models. The first model has the gripper stiffness set to 0, i.e. there is no gripper included in the system, and one with the gripper included. This is to show the effect of a gripper on the frequency of a suspended monopile and to prove that the model works in multiple scenarios. The frequencies of the eigenmodes are given in Table 3.2. The behaviour of the first two eigenmodes of the system are shown in Figure 3.2. These two modes of each system are of interest due to the fact that these are in the period range that a typical sea state might experience. The third natural frequency is vertical translation of the monopile at a higher frequencies and not of interest for this study. In Section 3.2.4 this system is modelled in OrcaFlex and the calculated frequencies will be compared to each other to validate the MATLAB model.

Table 3.2: Eigenmodes of the system without and with a gripper

Type of system	Mode number	Period [s]	Frequency [Hz]
No Gripper	Mode 1	22.0	0.046
	Mode 2	5.82	0.172
Gripper	Mode 1	7.00	0.143
	Mode 2	1.31	0.766

In Figure 3.2 the modes are visualised of the monopile excluding the gripper and with the gripper. In Figure 3.2a it can be seen that when no gripper is included in the system the first mode resembles a low frequent pendulum motion with a single rotation point at the cranetip. However, mode 2 of the system excluding gripper describes a higher frequent motion around a node positioned just below half the monopile length this can be seen in Figure 3.2b. In mode 1 of the actual system with a gripper, Figure 3.2c, a node is near the gripper height with the monopile rotating around this point. The higher frequent motion of the monopile gripper combination, mode 2, is visualised in 3.2d and shows a mode where the gripper actually moves with the monopile and the rotation point is located higher, in this case between the top of the monopile and its centre of gravity.

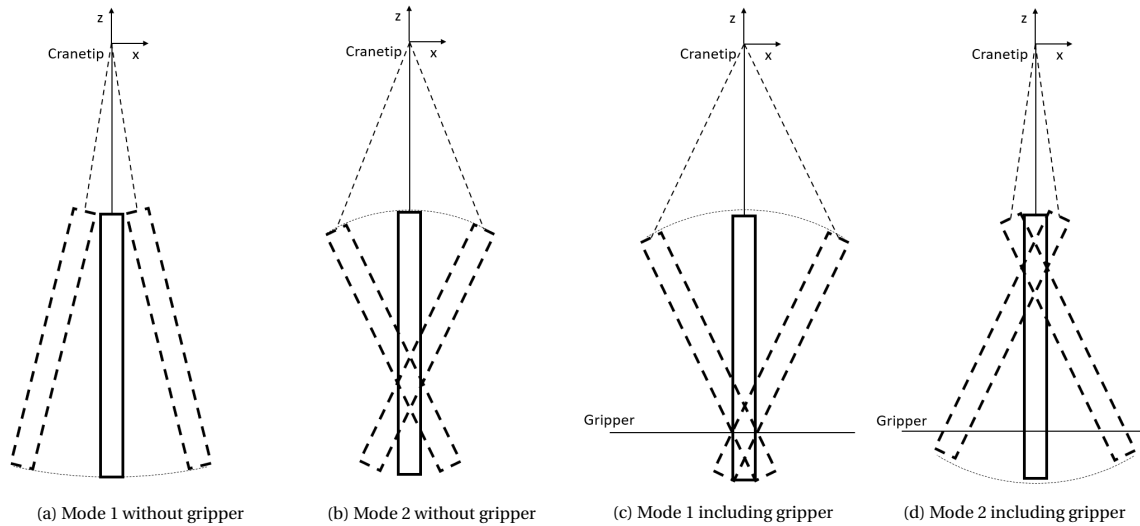


Figure 3.2: Modes of a monopile suspended from a crane wire.

3.2.3. ORCAFLEX

To validate the code and the MATLAB model a model is also built in OrcaFlex. This is done with the exact same inputs as the mathematical model used in MATLAB. OrcaFlex is widely used in the offshore industry and has proven itself in many offshore projects. Its use include, but are not limited to, installation analysis of pipelay, anchor and mooring deployment, risers, through splash-zone deployment, deep water installation of subsea hardware and offshore wind farm installation, [25].

OrcaFlex uses finite element with 6 DoFs at each node and can use various constraints to fix or impose individual DoFs. It can also connect midline nodes to any other object. This is particularly handy with e.g. gripper connection to monopile. OrcaFlex has fully coupled tension, bending and torsion for both small and non-linear large displacement analysis. There are multiple numerical procedures to solve these problems. The first one is non-linear implicit or explicit time domain analysis with variable or constant time steps. The second one is frequency domain analysis 1st and 2nd order, [25]. However, frequency domain doesn't include nonlinear effects as well as effects that are dependent on time.

Both regular and irregular waves can be simulated. Regular waves Airy, Stokes'5th and more. Irregular waves are the ones that will be used as they are more true to the realistic situation of an offshore location. Irregular waves can be created using for example JONSWAP, ISSC, Ochi-Hubble and Time History. The water can be defined by the user by setting the water density, kinematic viscosity and temperature. These can be constant or variable with depth, [25].

In OrcaFlex it is possible to integrate an external controller which is the next step to test if the CMG concept will work. The different components in the OrcaFlex model are discussed below, in Section 3.2.4, such as cranewire, monopile and gripper constraints.

3.2.4. ORCAFLEX MODEL SETUP

The cranewire is modelled as a *link* of the type *tether*. Tethers are a simplistic representation of a wire. They are massless as the effect of the mass can be neglected with respect the mass of the monopile. It can take tension but not compression and the force is dependent on the relative position of the ends of the tether. The attachment points are the crane tip and the top of the monopile. The unstretched length and stiffness are specified and are $75m$ and $37 \cdot 10^6 N/m$, respectively. If the distance between the two ends is smaller than the unstretched length that is specified, the tether will not apply force and falls slack. The top part of the tether is fixed $150m$ above sea level. The bottom is attached to the monopile and is free to move.

The monopile is modelled as a homogeneous pipe with the same dimensions as mentioned in Table 3.1,

80m in length, 8m in diameter, wall thickness of 0.06m and a steel density of $7.85 \cdot 10^3 \text{ kg/m}^3$. The Young's modulus is that of steel 212GPa. The gripper is modelled as 3 separate constraints 10m above sea level. They are connected to each other to allow it to move along the x – axis, z – axis and rotate around the y – axis. The stiffness in x direction is the same as the gripper stiffness, $10 \cdot 10^6 \text{ N/m}$. Translation in the y direction is prohibited by a rigid constraint. Another rigid constrain is the constraint that prohibits the rotation around the x – axis. The monopile is free to move along the z – axis. This essentially transforms it to a 2D problem to simplify the comparison to the MATLAB model. If it is not simplified into a 2D model the same eigenfrequencies will be observed. However, due to the symmetry in x and y direction this means that the all the frequencies/modes are doubled. This is because it will have the same eigenmodes for these two directions. Figure 3.3 shows the model in OrcaFlex. The motion of the eigenmodes are similar to the ones discussed before and their frequencies are shown in Table 3.3.

Table 3.3: Eigenmodes of the system without and with a gripper computed in OrcaFlex

Type of system	Mode number	Period [s]	Frequency [Hz]
No Gripper	Mode 1	22.0	0.046
	Mode 2	5.80	0.173
Gripper	Mode 1	7.00	0.143
	Mode 2	1.30	0.768

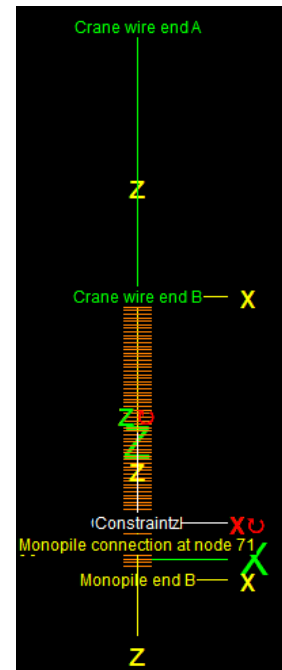


Figure 3.3: OrcaFlex model

3.2.5. MODEL COMPARISON AND VALIDATION

Now that the eigenfrequencies of the MATLAB and OrcaFlex model have been computed for the case where the monopile suspended in air, a comparison has been made to see if there is a difference between the two models also percentage wise. The results are shown in Table 3.4. It can be seen that for both the gripper and 'no-gripper' system the results are similar with only a negligible difference between the results (all errors are smaller than 1%). This can be credited to the fact that in MATLAB the monopile is rigid while in OrcaFlex the monopile is modelled as a flexible pipe with the stiffness proportional to its Young's modulus and area moment of inertia.

Table 3.4: Comparison of eigenfrequencies between MATLAB and OrcaFlex

Type of system	Mode number	MATLAB Frequency [Hz]	OrcaFlex Frequency [Hz]	Difference [%]
No Gripper	Mode 1	0.046	0.046	-0.11
	Mode 2	0.172	0.173	0.44
Gripper	Mode 1	0.143	0.143	0.10
	Mode 2	0.766	0.768	0.33

3.3. MONOPILE INCLUDING ADDED MASS

3.3.1. DETERMINING KEY VARIABLES

The equations of motion described in Section 3.2.1 are without any water, i.e. it is the monopile suspended in the air without partly being submerged. When the part of the monopile that is submerged, L_{sub} , fills with water this water moves along with the motion of the monopile as if it is attached to it. This mass is called *trapped mass*, m_{tm} . The equation for the trapped mass is trivial as it is the volume of the submerged part of the monopile times the density of water as shown by Equation 3.70. However, there also exists water on the outside that moves together with the monopile even though this water is not enclosed by the monopile. This is known as the *added mass*, m_{am} . The equation for the added mass is given in Equation 3.71 [5]. The added mass is determined by the area of the enclosed area of the reference object A_r which in this case is the monopile and therefore the enclosed area of the outer radius can be used, density of the fluid surrounding the object ρ which is seawater in this case and the added mass coefficient C_a that is 1 for a cylinder [5]. Note that this gives the added mass in kg/m and thus it still has to be multiplied by the length it is submerged L_{sub} . Using this knowledge Equation 3.71 can be written as Equation 3.72 for this particular case. As can be seen the trapped and added mass are a function of the inner and outer radius of the monopile and the submerged length, r_{in} , r_{out} and L_{sub} respectively. The length of the monopile that is submerged is calculated using Equation 3.73.

$$m_{tm} = \pi r_{in}^2 L_{sub} \rho_{sw} \quad (3.70)$$

$$m_{am} = \rho_{sw} C_a A_r \quad (3.71)$$

$$m_{am} = \pi r_{out}^2 L_{sub} \rho_{sw} \quad (3.72)$$

$$L_{sub} = L_0 + L_{0stretch} + L_{mp} - C_{height} \quad (3.73)$$

An important aspect to keep in mind is that the trapped and added mass only work in the x and θ -direction. In z -direction the water can freely move along and in and out of the monopile and thus the effect of added mass is not taken into account. However, another effect that can not be overseen is the effect of buoyancy. The buoyancy will lower the apparent weight the crane wire feels and therefore the stretch in equilibrium is less than given in Equation 3.30. In order to get to this new value the equilibrium position is used as shown in Equation 3.74 and is then solved for $L_{0stretch}$. The equation that is now used to calculate the new stretched length in equilibrium is given in Equation 3.75.

$$F_g = F_b + F_w \quad \rightarrow \quad g m_{mp} = A_{csmp} L_{sub} \rho_{sw} + L_{0stretch} k_{wire} \quad (3.74)$$

$$L_{0stretch} = \frac{g m_{mp} - A_{csmp} g \rho_{sw} (L_0 - C_{height} + L_{mp})}{k_{wire} + (A_{csmp} g \rho_{sw})} \quad (3.75)$$

Now that the trapped and added mass can be calculated their inertias can be determined. The inertia for the trapped mass is assumed to be that of a solid cylinder with the inner radius of the monopile as its radius. While the added mass is assumed to be a hollow cylinder with the monopiles outer radius as its inner radius and the outer radius is an estimation so that the added mass equals the mass of an equivalent hollow cylinder. The equation for the moment of inertia is for the trapped mass is given in Equation 3.76 [2] and Equation 3.77 [2] shows the equation for the added mass inertia. The r_{outam} in Equation 3.77 is there in order to determine the equivalent outer radius of the added mass cylinder. This derivation is shown in Equation 3.78

$$I_{tm} = \frac{m_{tm}}{12} (3r_{in}^2 + L_{sub}^2) \quad (3.76)$$

$$I_{am} = \frac{m_{am}}{12} (3((r_{outam})^2 + r_{out}^2) + L_{sub}^2) \quad (3.77)$$

$$\begin{aligned}
m_{am} &= m_{waterascylinder} \\
\pi r_{out}^2 L_{sub} \rho_{sw} &= \pi (r_{outam}^2 - r_{out}^2) L_{sub} \rho_{sw} \\
r_{out}^2 &= r_{outam}^2 - r_{out}^2 \\
r_{outam} &= \sqrt{2} r_{out}
\end{aligned} \tag{3.78}$$

The inertias given are the local inertias. To compute the total inertia of the monopile with trapped and added mass the parallel axis theorem is used. The total inertia of the system is given in Equation 3.82. Where L_{cgmp} is the centre of gravity of the monopile and L_{cgtot} the centre of gravity of the total system including the trapped and added mass. The centre of gravity for both trapped and added mass is denoted by L_{cgam} and is determined using Equation 3.80. These locations of the centre of gravity are taken from the top of the monopile.

$$m_x = m_{mp} + m_{tm} + m_{am} \tag{3.79}$$

$$L_{cgam} = L_{mp} - \frac{L_{sub}}{2} \tag{3.80}$$

$$L_{cgtot} = \frac{L_{cgmp} m_{mp} + L_{cgam} (m_{tm} + m_{am})}{m_x} \tag{3.81}$$

$$I = I_{mp} + m_{mp} (L_{cgmp} - L_{cgtot})^2 + I_{am} + m_{am} (L_{cgam} - L_{cgtot})^2 + I_{tm} + m_{tm} (L_{cgam} - L_{cgtot})^2 \tag{3.82}$$

3.3.2. NATURAL FREQUENCIES OF MONOPILE INCLUDING ADDED AND TRAPPED MASS

The new variables determined in the previous Section have an effect on the behaviour of the system. Implementing these variables into the MATLAB model and adding water to the OrcaFlex model will give different natural frequencies as before due to the added and trapped mass.

The equations given in Section 3.3.1 for the mass, inertia and centre of gravity are all dependent on the length of the crane wire, L_0 . In order to get a better understanding of the behaviour of the system when being lowered the eigenfrequencies are determined for a range of different crane wire lengths. The crane wire length extend from 69 meters to 99 meters. This represent the monopile being lowered to a depth of 30 meters. This is done both in OrcaFlex and MATLAB. The OrcaFlex model is similar to the one discussed in Section 3.2.4. The only difference is that seawater is added i.e. added and trapped mass are considered, with a density of $\rho_{sw} = 1.025 \cdot 10^3$. The results are plotted in Figures 3.4 and 3.5.

It can be seen that the behaviour of the second eigenfrequency is very similar in both models and only minor differences can be observed. The overall trend of both frequencies is that when the submerged length is increased the frequency goes down. For the first eigenfrequency this is more prevalent after 10 meters of submergence. The reason is that when the monopile is being lowered water moves with the pile increasing the mass being moved around which results in a lower frequency. The increasing length of the crane wire will also contribute to this just as it does with a pendulum, where a longer wire also results in a lower eigenfrequency.

When the first eigenfrequency is compared to OrcaFlex, larger differences are detected compared to the second eigenfrequency. However, these differences in reality are not that relevant. If a controller is designed for a frequency of e.g. $0.08 Hz$ and the actual value is $0.07 Hz$ this does not make a difference even though the actual difference is 12%. This will be shown later in Section 3.4.1. The third eigenfrequency is not shown as this one is not of interest for this study and the eigenfrequencies coincide with each other.

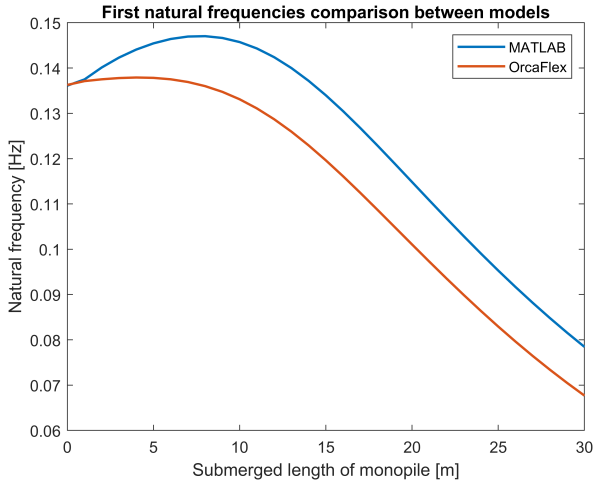


Figure 3.4: Comparison of first natural frequency between models

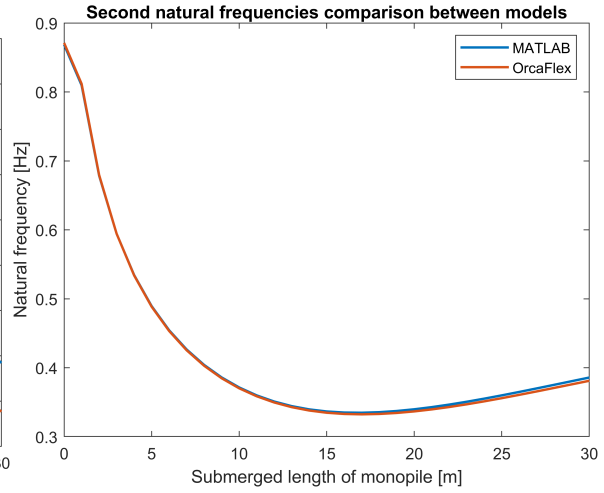


Figure 3.5: Comparison of second natural frequency between models

3.4. CONTROLLER

3.4.1. PID CONTROLLER

The next step is to design a controller that provides the moment exerted by the CMG on the monopile to control the angle θ . At this stage the controller will just apply a pure moment straight on the monopile to show that by creating a moment the motion can be controlled in a favorable manner. The whole system is shown in Figure 3.6. As can be seen the controller is a 'simple' Proportional Integral Derivative (PID) controller. The input to the state space block is $u(t)$ where the state space block is the state space system given in Section 3.1.3. The output signal $y(t)$ is still selected to show all the states. Therefore, the output is multiplied by a gain. This gain is called C_{tuning} and is added to get θ as the output signal in order to tune the controller. C_{tuning} is given in Equation 3.83. The reference signal r_0 is the desired angle of the monopile and thus is 0. $e(t)$ is the difference between the desired monopile angle and the actual angle. This difference (error) is used by the PID controller to determine what moment should be actuated on the monopile to reduce the error to 0 and thus placing the monopile in the desired upright position where θ equals 0. The proportional gain is K_p , the integral gain is K_i and the derivative gain is denoted as K_d .

$$C_{tuning} = [0 \ 0 \ 1 \ 0 \ 0 \ 0]^T \tag{3.83}$$

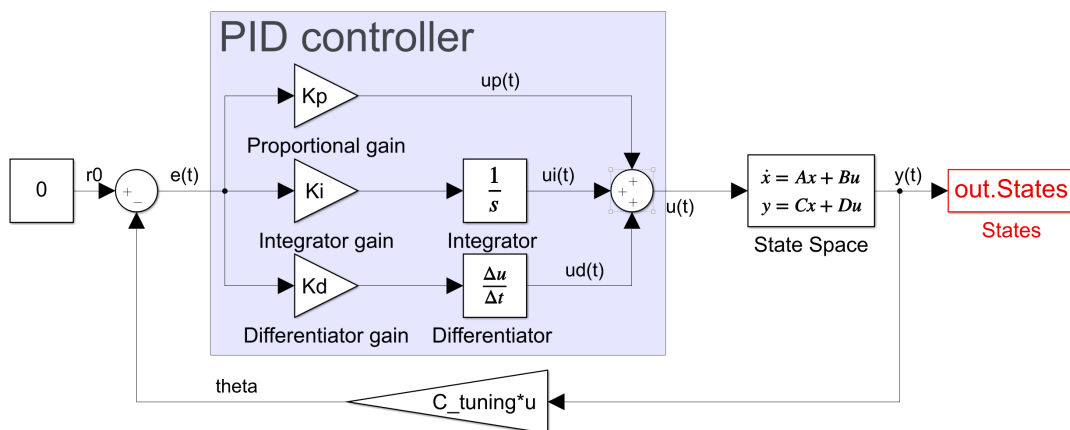


Figure 3.6: Block diagram PID control system

In order to get the correct PID values, use is made of the method described in Section 2.2. The first step is to create a Bode plot using the statespace system that is constructed using the equations of motion for the

monopile that is partially submerged in water. As this is still an example to show that the monopile can be stabilized using a moment, a single crane wire length is chosen and tuned in such a way that it will give favourable results. In the actual case a controller has to be designed to work on multiple frequencies i.e. all crane wire lengths. The bode plot for a crane wire length of 99 meters is shown in figure 3.7. This is the case in which the monopile is submerged 30 meters.

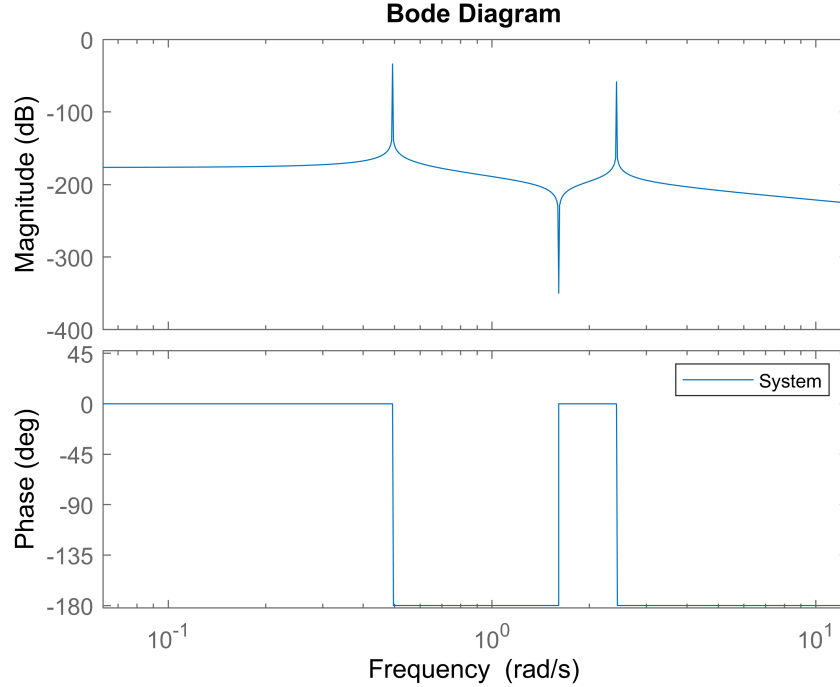


Figure 3.7: Bode plot of the system when crane wire is submerged 30 meters (crane wire length 99)

The next step is to determine the bandwidth. As the actual CMG properties are still unknown at this point an educated guess has to be made. For this situation it is chosen that the maximum operating frequency is 0.3 Hz.

$$\omega_d = \frac{2\pi f_c}{3} = 0.63 \text{ rad} \cdot \text{s}^{-1} \quad (3.84)$$

$$\omega_i = 2\pi \cdot 0.1 \cdot f_c = 0.19 \text{ rad} \cdot \text{s}^{-1} \quad (3.85)$$

The gain at $f_c = 0.3 \text{ Hz}$ is $G_{dB} = -200 \text{ dB}$. With this the total gain can be computed using 3.86. Following the steps described in Chapter 2.2 the values for K_p , K_i and K_d can be calculated. This is done in equations 3.87 to 3.89.

$$K_t = -\frac{1}{10^{\frac{G_{dB}}{20}}} = 8.91 \cdot 10^9 \text{ N} \cdot \text{m} \cdot \text{rad}^{-1} \quad (3.86)$$

$$K_p = \frac{K_t}{3} = 2.97 \cdot 10^9 \text{ N} \cdot \text{m} \cdot \text{rad}^{-1} \quad (3.87)$$

$$K_i = K_p \omega_i = 5.60 \cdot 10^8 \text{ N} \cdot \text{m} \cdot (\text{rad} \cdot \text{s})^{-1} \quad (3.88)$$

$$K_d = \frac{K_p}{\omega_d} = 4.73 \cdot 10^9 \text{ N} \cdot \text{m} \cdot \text{s} \cdot \text{rad}^{-1} \quad (3.89)$$

Using these values to create the control loop, open loop and closed loop Bode plots are depicted in Figure 3.8. The open loop as well as the closed loop are stable and phase and gain margins are 121° and 60.9 dB. The

closed loop is also sufficiently close to the 0dB line thus making this first estimate of the value a valid starting point and could be tuned further if needed.

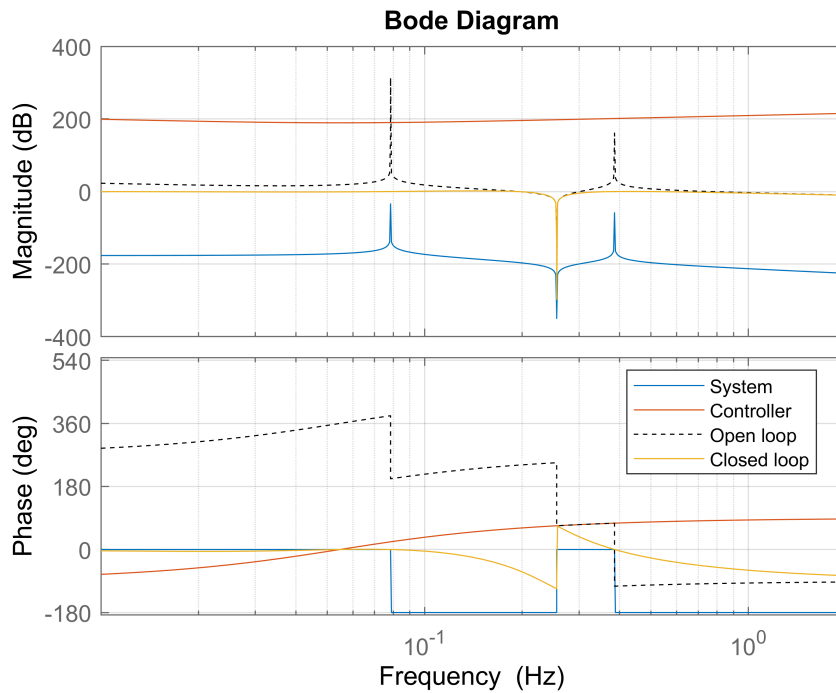


Figure 3.8: Bode plot of important loops

To test if the controller works properly the system is given an offset from its equilibrium. In this case the initial condition for θ is set to 0.2 radians or 11.5 degrees. The results of the system with the controller and the original system are plotted in order to clearly see the positive effect the controller has on the behaviour of the system. The goal is to damp out the angle of the monopile i.e. bring θ back to 0.

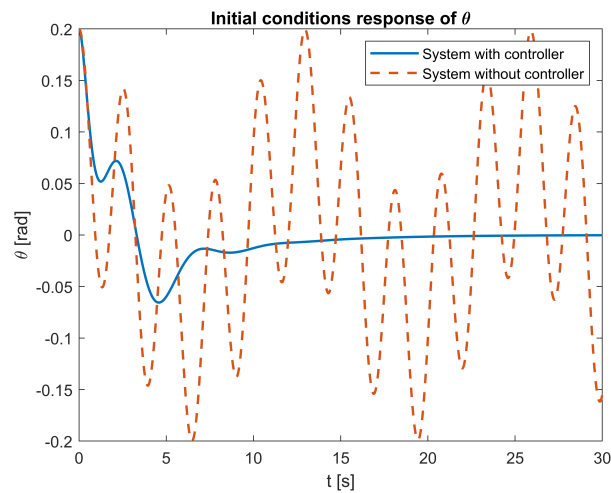


Figure 3.9: Initial condition response of θ

From Figure 3.9 it can be seen that the motion of the system with no controller is a periodic motion with no damping. This is logical as no damping is incorporated into the model. The motion of the controlled system damps out due to the controller at work, thus giving favourable results. The controller could be optimized even more however for the purpose of demonstration it is sufficient. The next step is to run an OrcaFlex simulation with actual waves hitting the monopile to get an idea of how the system behaves in more realistic conditions.

3.4.2. CONTROLLER ORCAFLEX INTEGRATION

In order to show that the concept and the tuned controller from Section 3.4.1 works the same PID controller is constructed to work in OrcaFlex. This enables the possibility to see the effect the controller has when the monopile is subjected to real wave conditions. For this demonstration the setup is chosen to be the case where the crane wire has a roll out length of $L_0 = 99m$ and the wave height is $H_s = 2m$. In Figure 3.10 the results are shown for the situation with no controller and including controller (controlling an 'ideal' moment around the y -axis). To show the effect of the controller even more the controller is started after 50s simulation time. It can be seen that both lines show the exact same behaviour up until that point and that the monopile angle is steadily increasing in a periodic manner. When the controller is started it controls the monopile angle. As can be seen the angle of the monopile doesn't deviate from 0 degrees by more than 0.5 degrees. This in contrary to the 'No controller' case where the maximum monopile angle is more than 8 degrees.

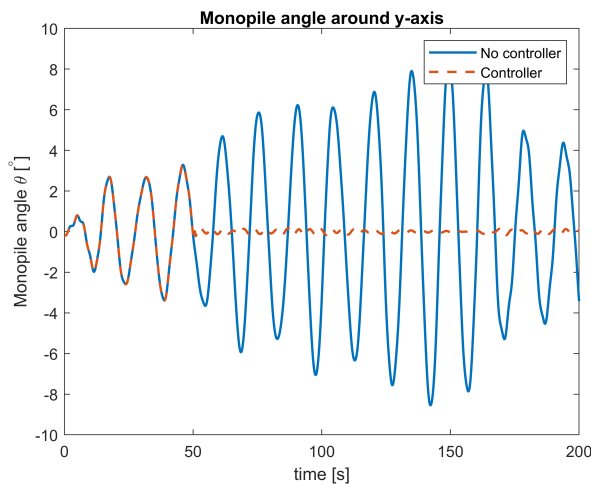


Figure 3.10: Monopile angle during 200s simulation with $H_s=2m$

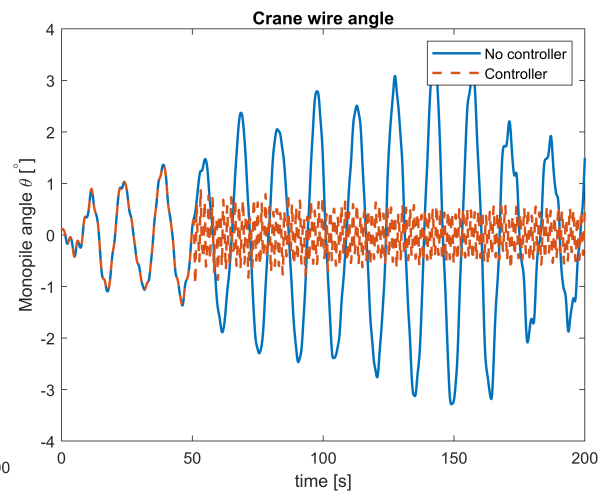


Figure 3.11: Crane wire crane wire angle during 200s simulation with $H_s=2m$

Even more important than the monopile angle is the angle the crane wire makes. These two values are of course closely linked as can be seen in their behaviour in Figure 3.10 and 3.11. Again, there are two cases presented: the 'no controller' case and the one including a controller implementing the restoring moment around the y -axis. It can be seen that the crane wire of the system without controller exceeds 3 degrees for crane wire angle while the controller makes sure that the maximum angle of the crane wire remains below a 1 degree angle.

The OrcaFlex integration shows that a properly tuned device that creates a moment can have a beneficial effect on crane wire angles in real offshore situations. It should be noted that at this point the moment is generated out of 'thin air' as there is no physical actuator in this model yet. Once this is added the controller will have to be re-tuned again in order to get favourable results.

3.5. CONTROL MOMENT GYROSCOPE

3.5.1. EQUATIONS OF MOTION CMG

During the literature study performed ahead of the thesis it was determined that the most suitable gyroscopic actuator is the control moment gyroscope. Reason is that CMGs can create a larger moment with respect to reaction wheels with any given amount of momentum capacity that the rotating disk can store, as shown in Figure 3.12 [36]. However, the equations of motion of a CMG are more elaborate than the ones a reaction wheel. Therefore, a small downside of the CMG is that these elaborate equations have to be incorporated in the controller as well as the *Euler angles*, explained in detail in Appendix G, making the tuning of the controller more complex.

The control moment gyroscope (CMG) is the actuator that will create the moment around the y -axis that is discussed in part 3.4.1 where it is modelled as an ideal moment readily available at any moment. In order to better grasp the way the CMG works the equations of motion are determined using the Lagrange method as shown before in sections 2.1.1 and 3.1.1. As usual the first step is to determine the degrees of freedom and

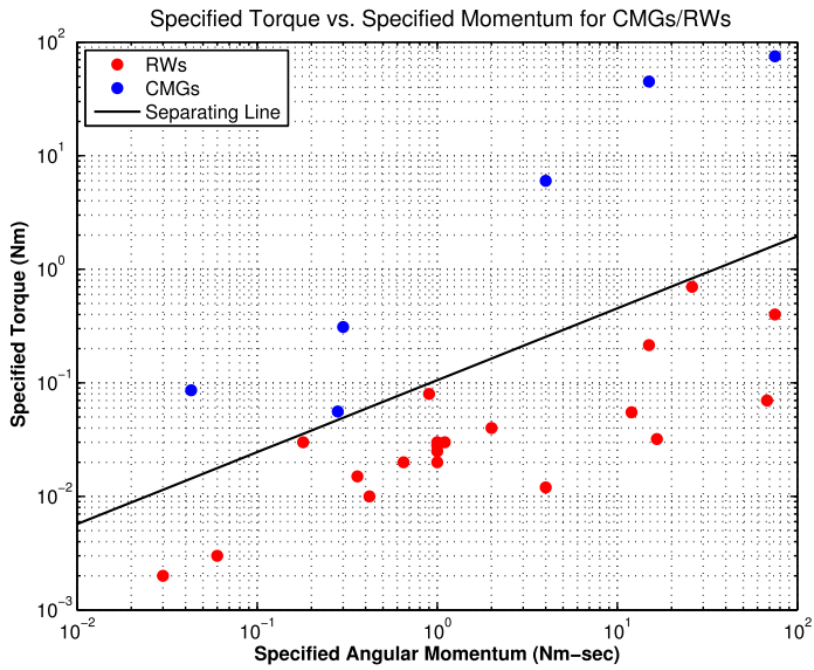


Figure 3.12: Torque against angular momentum for both CMGs and RWs [36].

the general coordinates that are used to express the kinetic and potential energy. In Figure 3.13 a simplified depiction of a control moment gyroscope is shown. As can be seen the CMG can rotate around the origin which is aligned with its centre of gravity therefore the degrees of freedom are θ , ϕ and ψ . In Equation 3.90 the generalized coordinates are shown and their derivatives.

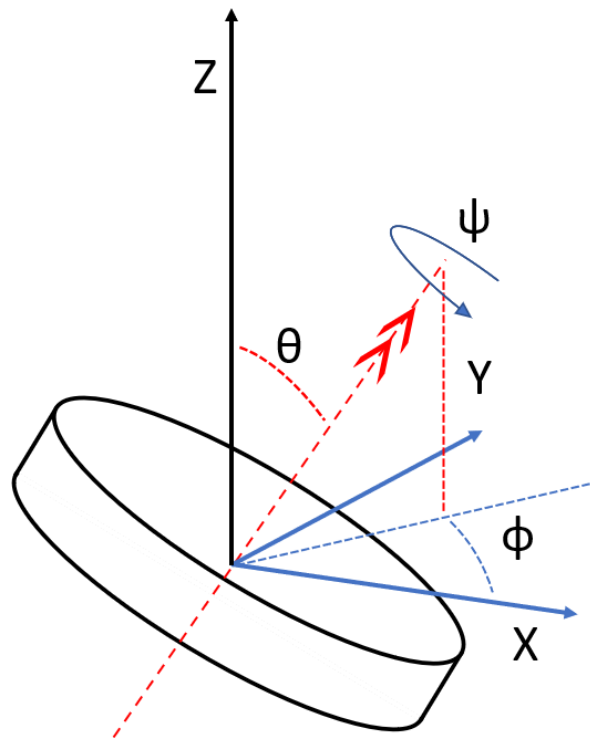


Figure 3.13: Simplified drawing of control moment gyroscope showing its degrees of freedom

$$q = \begin{bmatrix} \theta \\ \phi \\ \psi \end{bmatrix} \quad \dot{q} = \begin{bmatrix} \dot{\theta} \\ \dot{\phi} \\ \dot{\psi} \end{bmatrix} \quad \ddot{q} = \begin{bmatrix} \ddot{\theta} \\ \ddot{\phi} \\ \ddot{\psi} \end{bmatrix} \quad (3.90)$$

The first step is to determine the kinetic energy of the CMG around flywheel axis system where the angular velocities around the axis x_f , y_f and z_f are ω_x , ω_y and ω_z , respectively. The total kinetic energy is built using equation

$$\begin{aligned} T_{cmg} &= \frac{1}{2} I_{xy} \omega_x^2 + \frac{1}{2} I_{xy} \omega_y^2 + I_{zcmg} \omega_z^2 \\ &= \frac{1}{2} I_{xy} (\omega_x^2 + \omega_y^2) + I_{zcmg} \omega_z^2 \end{aligned} \quad (3.91)$$

The next step is to write the angular velocities such that the kinetic energy is expressed using the general coordinates. This is done using Euler angles. A clear explanation and derivation of the Euler angles used in the final transformation matrix is shown in Equation 3.92 is given in Appendix G.

$$\begin{bmatrix} \omega_x \\ \omega_y \\ \omega_z \end{bmatrix} = \begin{bmatrix} \sin \psi \sin \phi & \cos \psi & 0 \\ \cos \psi \sin \phi & -\sin \psi & 0 \\ \cos \theta & 0 & 1 \end{bmatrix} \begin{bmatrix} \dot{\theta} \\ \dot{\phi} \\ \dot{\psi} \end{bmatrix} \quad (3.92)$$

Using this matrix the angular velocity components are given in equations 3.93, 3.94 and 3.95 for ω_x , ω_y and ω_z , respectively.

$$\begin{aligned} \omega_x^2 &= (\dot{\theta} \sin \psi \sin \phi + \dot{\phi} \cos \psi)^2 \\ &= \dot{\theta}^2 \sin^2 \psi \sin^2 \phi + 2\dot{\theta}\dot{\phi} \sin \psi \cos \psi \sin \phi + \dot{\phi}^2 \cos^2 \psi \end{aligned} \quad (3.93)$$

$$\begin{aligned} \omega_y^2 &= (\dot{\theta} \cos \psi \sin \phi - \dot{\phi} \sin \psi)^2 \\ &= \dot{\theta}^2 \cos^2 \psi \sin^2 \phi - 2\dot{\theta}\dot{\phi} \sin \psi \cos \psi \sin \phi + \dot{\phi}^2 \sin^2 \psi \end{aligned} \quad (3.94)$$

$$\omega_z^2 = (\dot{\theta} \cos \phi + \dot{\psi})^2 \quad (3.95)$$

From Equation 3.93 and 3.94 it can be seen that when they are added together the equations are simplified. This is shown in Equation 3.96.

$$\omega_x^2 + \omega_y^2 = \dot{\theta}^2 \sin^2 \phi + \dot{\phi}^2 \quad (3.96)$$

Substituting equations 3.96 and 3.95 into Equation 3.91 and making use of the fact that the disk is spinning at a very high but constant angular velocity then $\dot{\psi}$ will be a constant named $\dot{\psi}_0$. This can be done due to the fact that this is a cyclic coordinate and the angular momentum associated with this remains constant [22]. i.e. the time derivative part of the Lagrange equation is 0 for $\dot{\psi}$ and since there is no potential energy this equation is not of interest and can be neglected. This will simplify the Lagrange equations as the problem turns into an expression with only two variables. Then the total kinetic energy expressed in global coordinates will take the form of Equation 3.97.

$$T_{cmg} = \frac{1}{2} I_{xy} (\dot{\theta}^2 \sin^2 \phi + \dot{\phi}^2) + \frac{1}{2} I_{zcmg} (\dot{\theta} \cos \phi + \dot{\psi}_0)^2 \quad (3.97)$$

For the equation of motion for θ Equation 3.98 is solved. The terms of the equation are shown in equations 3.100 and 3.101. The derivative of the kinetic energy with respect to $\dot{\theta}$ is calculated first in 3.101.

$$\frac{d}{dt} \frac{\partial T}{\partial \dot{\theta}} - \frac{\partial T}{\partial \theta} + \frac{\partial V}{\partial \theta} = 0 \quad (3.98)$$

$$\frac{\partial T}{\partial \dot{\theta}} = I_{xy} \dot{\theta} \sin^2 \phi + I_{zcmg} \cos \phi (\dot{\theta} \cos \phi + \dot{\psi}_0) \quad (3.99)$$

$$\frac{d}{dt} \frac{\partial T}{\partial \dot{\theta}} = \ddot{\theta} (I_{zcmg} \cos^2 \phi + I_{xy} \sin^2 \phi) + \dot{\phi} (2I_{xy} \dot{\theta} \cos \phi \sin \phi - 2I_{zcmg} \dot{\theta} \cos \phi \sin \phi - I_{zcmg} \dot{\psi}_0 \sin \phi) \quad (3.100)$$

$$\frac{\partial T}{\partial \theta} = 0 \quad (3.101)$$

The equations involving θ lead to the final results shown in Equation 3.102.

$$\ddot{\theta} (I_{zcmg} \cos^2 \phi + I_{xy} \sin^2 \phi) + \dot{\phi} (2I_{xy} \dot{\theta} \cos \phi \sin \phi - 2I_{zcmg} \dot{\theta} \cos \phi \sin \phi - I_{zcmg} \dot{\psi}_0 \sin \phi) = 0 \quad (3.102)$$

Solving Equation 3.103 will lead to the equation of motion is for ϕ . The terms are worked out in equations 3.105 and 3.105. The derivative of the kinetic energy with respect to $\dot{\phi}$ is calculated first in 3.104.

$$\frac{d}{dt} \frac{\partial T}{\partial \dot{\phi}} - \frac{\partial T}{\partial \phi} + \frac{\partial V}{\partial \phi} = 0 \quad (3.103)$$

$$\frac{d}{dt} \frac{\partial T}{\partial \dot{\phi}} = I_{xy} \dot{\phi} \quad (3.104)$$

$$\frac{d}{dt} \frac{\partial T}{\partial \dot{\phi}} = I_{xy} \ddot{\phi} \quad (3.105)$$

$$\frac{\partial T}{\partial \phi} = I_{xy} \dot{\theta}^2 \cos \phi \sin \phi - I_{zcmg} \dot{\theta} \sin \phi (\dot{\psi}_0 + \dot{\theta} \cos \phi) \quad (3.106)$$

The final equation of motion for ϕ is stated in Equation 3.107

$$I_{xy} \ddot{\phi} - I_{xy} \dot{\theta}^2 \cos \phi \sin \phi + I_{zcmg} \dot{\theta} \sin \phi (\dot{\psi}_0 + \dot{\theta} \cos \phi) = 0 \quad (3.107)$$

Note that in this case there is no potential energy as the centre of gravity is at its rotational point and no springs are attached in this situation. Now that the equations are determined they have to be linearized. The linearization is done around the points $\theta = 0$ and for ϕ is equal to $\pi/2$. The same steps have been taken as in the section before and as explained in Section 3.1.2. First the mass matrix is determined using Equation 3.109.

$$q_{eq} = \begin{bmatrix} 0 \\ \frac{\pi}{2} \end{bmatrix} \quad (3.108)$$

$$M = \left. \frac{\partial^2 T}{\partial \dot{q}_i^2} \right|_{q_{eq}} \rightarrow M = \begin{bmatrix} I_{xy} & 0 \\ 0 & I_{xy} \end{bmatrix} \quad (3.109)$$

The next step is calculation of the stiffness matrix. This is done according to Equation 3.110. It can be seen that the stiffness matrix is 0 since no springs are attached and gravity is not playing a role due to the fact that its centre of gravity is taken at 0 and thus not included.

$$K = \left. \frac{\partial^2 V}{\partial q_i \partial q_j} \right|_{q_{eq}} \rightarrow K = \begin{bmatrix} 0 & 0 \\ 0 & 0 \end{bmatrix} \quad (3.110)$$

Contrary to previous chapters and the example problems given in Appendix A and B the damping matrix is not 0. The terms that are inherent of a gyroscope appear in this matrix as they are dependent on the angular velocity of the gyroscope. The calculation used to determine the damping matrix is given in Equation 3.112. Where the terms of the total Lagrange equations, dependent on the kinetic energy, are called f_T and are shown in Equation 3.111.

$$f_T = \frac{d}{dt} \frac{\partial T}{\partial \dot{q}} - \frac{\partial T}{\partial q} \quad (3.111)$$

$$D = \left. \frac{\partial f_T}{\partial \dot{q}_i} \right|_{q_{eq}} \rightarrow D = \begin{bmatrix} 0 & -I_{zcmg}\dot{\psi}_0 \\ I_{zcmg}\dot{\psi}_0 & 0 \end{bmatrix} \quad (3.112)$$

The linearized equations are given in 3.114 and 3.115.

$$M\ddot{q} + D\dot{q} + Kq = F \quad (3.113)$$

$$\ddot{\theta}I_{xy} - I_{zcmg}\dot{\psi}_0\dot{\phi} = 0 \quad (3.114)$$

$$I_{xy}\ddot{\phi} + I_{zcmg}\dot{\psi}_0\dot{\theta} = 0 \quad (3.115)$$

3.5.2. CMG DIMENSIONS

Ideally the moment generated by the CMG would be large enough to counter even the highest moments that a monopile experiences during operation. The dimensions of the CMG and its properties, such as maximum nutation and spin velocity, determine the maximum moment it can produce. However, these values have to be within the bounds of what is expected to be physically possible for its intended use. Examples of factors that play a role in determining the dimensions of the CMG can be size and weight limitation. This is due to the fact that the device has to be lifted in combination with the monopile and should not take up too much space and weight compared to the monopile. Furthermore, technical limitations are also prevalent such as a maximum spin rate, nutation velocity, material and mechanical properties. The angular velocities are constrained by the type of actuators and materials used as the forces can induce stresses into the structure higher than the material can withstand if not taken into account. However, as this is still a preliminary study the assumptions and calculations done will remain high level such that the assumed dimensions are within a reasonable range from the possible finished product. Thus giving realistic results in the analysis.

For the spinning disk/flywheel a ring will be used. This is to minimize the weight while maximizing its inertia. The ring's dimensions are all shown in Table 3.5.

Table 3.5: Dimensions of the Control Moment Gyroscope

Description	Abbreviation	Value	Unit
Thickness of disk	t_{cmg}	0.5	m
Outer radius of disk	r_{outcmg}	1.5	m
Inner radius of disk	r_{incmg}	1.2	m
Nutation velocity	$\dot{\phi}$	0.3	$rad\,s^{-1}$
Spin velocity	$\dot{\psi}_0$	2000	RPM

The constants that are used in the derivation of the equation of motion of the CMG can be determined using the values in Table 3.5. The equation used for the inertia for a ring is the same as for the monopile around its x and y axis and is shown in Equation 3.116. The inertia that defines the moment, the ring's spinning axis, around the z axis is defined as shown by Equation 3.117.

$$I_{xy} = \frac{1}{12}m_{cmg} \left(3 \left(r_{outcmg}^2 + r_{incmg}^2 \right) + t_{cmg}^2 \right) \quad (3.116)$$

$$I_{zcmg} = \frac{1}{2}m_{cmg} \left(r_{outcmg}^2 + r_{incmg}^2 \right) \quad (3.117)$$

Assuming that the material of the CMG will be steel the mass is easily obtained by multiplying the density of steel by the volume of the CMG. This can be determined using the given parameters and is shown in 3.118.

$$m_{cmg} = \pi \left(r_{outcmg}^2 - r_{incmg}^2 \right) t_{cmg} \rho_{steel} \quad (3.118)$$

With this configuration the maximum moment the CMG can produce is easily calculated by using Equation 3.119.

$$M_{cmg} = I_{zcmg}\dot{\psi}_0\dot{\phi} = 1157.8kN \quad (3.119)$$

It can be seen that increasing the spinning velocity or the nutation velocity increases the moment linearly. However, increasing the radius increases the inertia quadratically. This is shown in Figure 3.14.

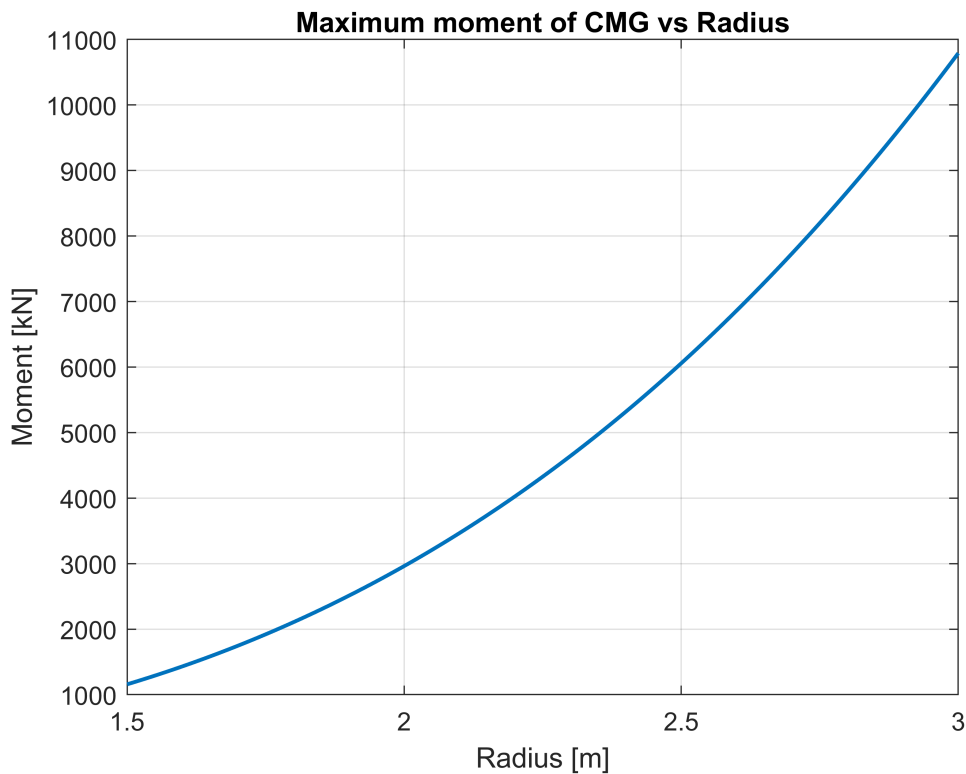


Figure 3.14: Flywheel size with increasing radius with all other parameters as constants versus the maximum moment it can then produce

3.6. MONOPILE INCLUDING CMG

Now that the equations of motion of a suspended monopile and a control moment gyroscope have been discussed the next step is to combine the two. The CMG will be placed on top of the monopile and will act as the lifting device as well. A schematic overview is given in Figure 3.15. It can be seen in this image that the rotation around the y -axis of the CMG is coupled to the monopile rotation, i.e. the angle θ of the monopile is equal to that of the CMG around the y -axis. The nutation angle ϕ on the other hand is an extra degree of freedom that has to be added within the equations of motion of the entire system. ϕ is a rotation around the x -axis. Therefore, the final system will have 4 degrees of freedom in total. The generalized coordinates and their derivatives are shown in Equation 3.120.

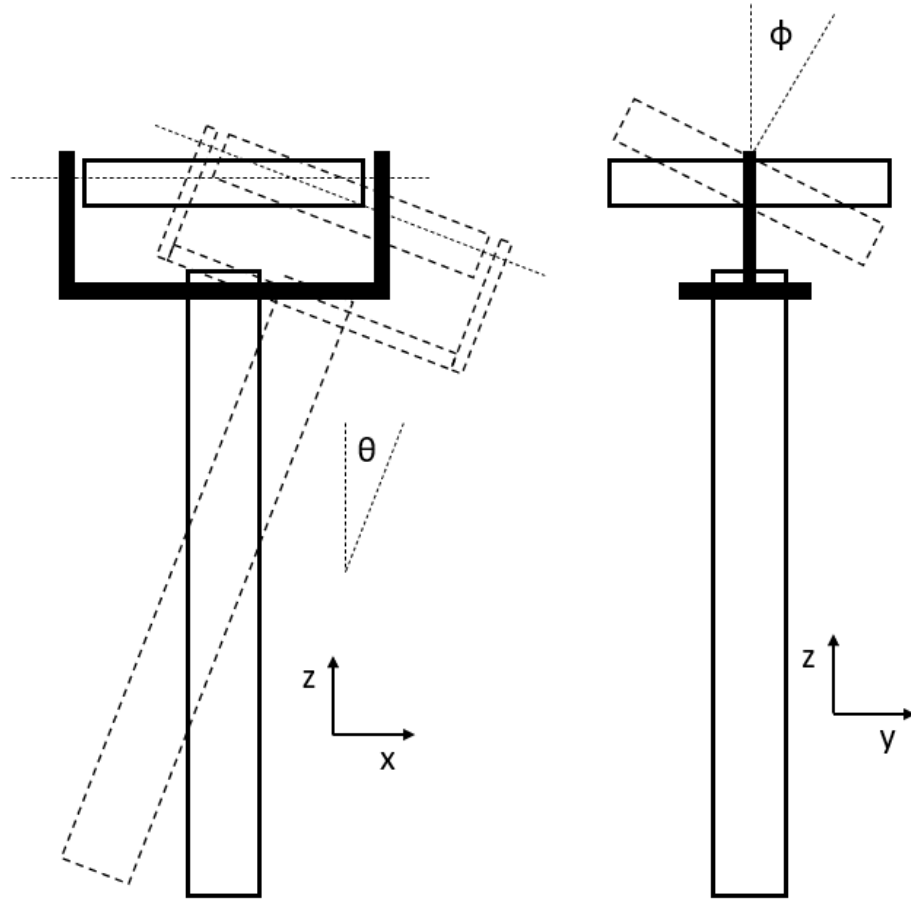


Figure 3.15: Simplified drawing of the monopile and the CMG that clearly show how the degrees of freedom act for θ and ϕ . The Left image is the front view displaying the monopile angle θ and the right image shows the side view showing the nutation angle ϕ

$$q = \begin{bmatrix} x \\ z \\ \theta \\ \phi \end{bmatrix} \quad \dot{q} = \begin{bmatrix} \dot{x} \\ \dot{z} \\ \dot{\theta} \\ \dot{\phi} \end{bmatrix} \quad \ddot{q} = \begin{bmatrix} \ddot{x} \\ \ddot{z} \\ \ddot{\theta} \\ \ddot{\phi} \end{bmatrix} \quad (3.120)$$

The total kinetic energy is combining the equations 3.91 and equations 3.2 which is given in Equation 3.121. The potential energy is equal to Equation 3.8, stated again in Equation 3.122 for convenience.

$$T_{total} = \frac{1}{2}I_{xy}(\dot{\phi}^2 + \dot{\theta}^2 \sin^2 \phi) + \frac{1}{2}I\dot{\theta}^2 + \frac{1}{2}I_{zcmg}(\dot{\psi}_0 + \dot{\theta} \cos \phi)^2 + \frac{1}{2}m_x \dot{x}_d^2 + \frac{1}{2}m_z \dot{z}^2 \quad (3.121)$$

$$V = m_z g z + \frac{1}{2}k_{wire}L_e^2 + \frac{1}{2}k_{gripper}G_x^2 \quad (3.122)$$

The same steps are taken as shown before. Therefore, only the final results of the linearized equations are shown as the mass, stiffness and damping matrix are almost identical as the ones shown in previous sections. The equilibrium points around which the equations are linearized are given in Equation 3.123. First the mass matrix is determined and is given in Equation 3.124. It can be seen that the mass matrix is now 4×4 .

$$q_{eq} = \begin{bmatrix} 0 \\ -(L_0 + L_{cgtot} + L_{0stretch}) \\ 0 \\ \frac{\pi}{2} \end{bmatrix} \quad (3.123)$$

$$M = \left. \frac{\partial^2 T}{\partial \dot{q}_i^2} \right|_{q_{eq}} \rightarrow M = \begin{bmatrix} m_x & 0 & 0 & 0 \\ 0 & m_z & 0 & 0 \\ 0 & 0 & I + I_{xy} & 0 \\ 0 & 0 & 0 & I_{xy} \end{bmatrix} \quad (3.124)$$

The damping matrix is now also a 4x4 and it are the same terms as given in Section 3.5.1 and are shown in Equation 3.126. With f_T given in Equation 3.125 which contains the kinetic energy terms of the Lagrange equation.

$$f_T = \frac{d}{dt} \frac{\partial T}{\partial \dot{q}} - \frac{\partial T}{\partial q} \quad (3.125)$$

$$D = \left. \frac{\partial f_T}{\partial \dot{q}_i} \right|_{q_{eq}} \rightarrow D = \begin{bmatrix} 0 & 0 & 0 & 0 \\ 0 & 0 & 0 & 0 \\ 0 & 0 & 0 & -I_{zcmg} \dot{\psi}_0 \\ 0 & 0 & I_{zcmg} \dot{\psi}_0 & 0 \end{bmatrix} \quad (3.126)$$

The stiffness matrix only gains a fourth row and column full of zeros as the rotation in ϕ direction is independent of any of the springs and gravity terms. The individual elements of the K matrix are given in 3.1.2.

$$K = \left. \frac{\partial^2 V}{\partial q_i \partial q_j} \right|_{q_{eq}} \rightarrow K = \begin{bmatrix} k_{11} & k_{12} & k_{13} & 0 \\ k_{21} & k_{22} & k_{23} & 0 \\ k_{31} & k_{32} & k_{33} & 0 \\ 0 & 0 & 0 & 0 \end{bmatrix} \quad (3.127)$$

Important is to note that the mass and inertia is now different as before. For the mass components in x and z direction the mass of the CMG is added. Due to the mass of CMG the centre of gravity of the total system changes as well as the inertia. In Equation 3.128 the mass in x -direction is calculated and it has for components: monopile mass, trapped mass, added mass and the mass of the CMG. The new centre of gravity is determined using Equation 3.130. Using the newly determined centre of gravity the inertia of the total system can be computed. This is the same as in Section 3.3.1 except that now the CMG is also taken into account. However, the local inertia is already included in the equation of motion due to the fact that the local inertia is taken into account in the kinetic energy. Therefore, the Steiner term is only included in the inertia calculation which only considers the effect of the point mass located away from the centre of gravity.

$$m_x = m_{mp} + m_{tm} + m_{am} + m_{cmg} \quad (3.128)$$

$$m_x = m_{mp} + m_{cmg} \quad (3.129)$$

$$L_{cgtot} = \frac{L_{cgmmp} m_{mp} + L_{cgam} (m_{tm} + m_{am}) + L_{cgmmp} m_{cmg}}{m_x} \quad (3.130)$$

$$I = I_{mp} + m_{mp} (L_{cgmmp} - L_{cgtot})^2 + I_{am} + m_{am} (L_{cgam} - L_{cgtot})^2 + I_{tm} + m_{tm} (L_{cgam} - L_{cgtot})^2 + m_{cmg} (0 - L_{cgtot})^2 \quad (3.131)$$

3.6.1. STATE SPACE MODEL COMPLETE SYSTEM

Now that the linearized equations of motion are known the next step consists of rewriting the equations in state space form as shown in Equation 3.132. As explained in Chapter 2.1.3 the first step is to isolate \ddot{q} as shown in Equation 3.133. The inverse matrix of M is given in Equation 3.134.

$$A = \begin{bmatrix} 0 & I \\ -M^{-1}K & -M^{-1}D \end{bmatrix}, \quad B = \begin{bmatrix} 0 \\ M^{-1}B_0 \end{bmatrix}, \quad C = [C_{oq} \quad C_{ov}] \quad (3.132)$$

$$\ddot{q} = M^{-1}B_0u - M^{-1}Kq - M^{-1}D\dot{q} \quad (3.133)$$

$$M^{-1} = \begin{bmatrix} \frac{1}{m_x} & 0 & 0 & 0 \\ 0 & \frac{1}{m_z} & 0 & 0 \\ 0 & 0 & \frac{1}{I+I_{xy}} & 0 \\ 0 & 0 & 0 & \frac{1}{I_{xy}} \end{bmatrix} \quad (3.134)$$

The state vector is shown in Equation 3.135

$$\vec{x} = \begin{pmatrix} x_1 \\ x_2 \\ x_3 \\ x_4 \\ x_5 \\ x_6 \\ x_7 \\ x_8 \end{pmatrix} = \begin{pmatrix} q_1 \\ q_2 \\ q_3 \\ q_4 \\ \dot{q}_1 \\ \dot{q}_2 \\ \dot{q}_3 \\ \dot{q}_4 \end{pmatrix} = \begin{pmatrix} x \\ z \\ \theta \\ \phi \\ \dot{x} \\ \dot{z} \\ \dot{\theta} \\ \dot{\phi} \end{pmatrix} \quad (3.135)$$

the A and B matrix can be constructed using Equation 2.55.

$$A = \begin{bmatrix} 0 & 0 & 0 & 0 & 1 & 0 & 0 & 0 \\ 0 & 0 & 0 & 0 & 0 & 1 & 0 & 0 \\ 0 & 0 & 0 & 0 & 0 & 0 & 1 & 0 \\ 0 & 0 & 0 & 0 & 0 & 0 & 0 & 1 \\ -\frac{k_{11}}{m_x} & -\frac{k_{12}}{m_x} & -\frac{k_{13}}{m_x} & 0 & 0 & 0 & 0 & 0 \\ -\frac{k_{21}}{m_z} & -\frac{k_{22}}{m_z} & -\frac{k_{23}}{m_z} & 0 & 0 & 0 & 0 & 0 \\ -\frac{k_{31}}{I+I_{xy}} & -\frac{k_{32}}{I+I_{xy}} & -\frac{k_{33}}{I+I_{xy}} & 0 & 0 & 0 & 0 & \frac{I_{zcmg}\psi_0}{I+I_{xy}} \\ 0 & 0 & 0 & 0 & 0 & 0 & -\frac{I_{zcmg}\psi_0}{I_{xy}} & 0 \end{bmatrix} \quad (3.136)$$

The B matrix will look as shown in Equation 3.138. Even though the system is controlled by exerting a moment around the y -axis in the ϕ direction all the other inputs are included in the B matrix as well. This is done in order to get the bode plots from all inputs to all outputs, depending on the input vector u . The input vector u is given in Equation 3.137. Where F_x and F_z are input forces in the x and z directions, while M_θ and M_ϕ are the input moments around the y and x axis. M_ϕ is therefore the moment that the controller determines to control the system.

$$u = \begin{pmatrix} F_x \\ F_z \\ M_\theta \\ M_\phi \end{pmatrix} \quad (3.137)$$

$$B = \begin{bmatrix} 0 & 0 & 0 & 0 \\ 0 & 0 & 0 & 0 \\ 0 & 0 & 0 & 0 \\ 0 & 0 & 0 & 0 \\ \frac{1}{m_x} & 0 & 0 & 0 \\ 0 & \frac{1}{m_z} & 0 & 0 \\ 0 & 0 & \frac{1}{I+I_{xy}} & 0 \\ 0 & 0 & 0 & \frac{1}{I_{xy}} \end{bmatrix} \quad (3.138)$$

The C matrix is chosen so that all the displacements and velocities are given and thus is a 6x6 identity matrix.

$$C = \begin{bmatrix} 1 & 0 & 0 & 0 & 0 & 0 & 0 \\ 0 & 1 & 0 & 0 & 0 & 0 & 0 \\ 0 & 0 & 1 & 0 & 0 & 0 & 0 \\ 0 & 0 & 0 & 1 & 0 & 0 & 0 \\ 0 & 0 & 0 & 0 & 1 & 0 & 0 \\ 0 & 0 & 0 & 0 & 0 & 1 & 0 \\ 0 & 0 & 0 & 0 & 0 & 0 & 1 \end{bmatrix} \quad (3.139)$$

The full state space representation is shown in 3.57.

$$\begin{aligned} \dot{x} &= Ax + Bu \\ y &= Cx + D_{ss}u \end{aligned} \quad (3.140)$$

$$\begin{pmatrix} \dot{x} \\ \dot{z} \\ \dot{\theta} \\ \dot{\phi} \\ \ddot{x} \\ \ddot{z} \\ \ddot{\theta} \\ \ddot{\phi} \end{pmatrix} = \begin{bmatrix} 0 & 0 & 0 & 0 & 1 & 0 & 0 & 0 \\ 0 & 0 & 0 & 0 & 0 & 1 & 0 & 0 \\ 0 & 0 & 0 & 0 & 0 & 0 & 1 & 0 \\ 0 & 0 & 0 & 0 & 0 & 0 & 0 & 1 \\ -\frac{k_{11}}{m_x} & -\frac{k_{12}}{m_x} & -\frac{k_{13}}{m_x} & 0 & 0 & 0 & 0 & 0 \\ -\frac{k_{21}}{m_z} & -\frac{k_{22}}{m_z} & -\frac{k_{23}}{m_z} & 0 & 0 & 0 & 0 & 0 \\ -\frac{k_{31}}{I+I_{xy}} & -\frac{k_{32}}{I+I_{xy}} & -\frac{k_{33}}{I+I_{xy}} & 0 & 0 & 0 & 0 & 0 \\ 0 & 0 & 0 & 0 & 0 & 0 & -\frac{I_{zcmg}\psi_0}{I_{xy}} & 0 \end{bmatrix} \begin{pmatrix} x \\ z \\ \theta \\ \phi \\ \dot{x} \\ \dot{z} \\ \dot{\theta} \\ \dot{\phi} \end{pmatrix} + \begin{bmatrix} 0 & 0 & 0 & 0 \\ 0 & 0 & 0 & 0 \\ 0 & 0 & 0 & 0 \\ 0 & 0 & 0 & 0 \\ \frac{1}{m_x} & 0 & 0 & 0 \\ 0 & \frac{1}{m_z} & 0 & 0 \\ 0 & 0 & \frac{1}{I+I_{xy}} & 0 \\ 0 & 0 & 0 & \frac{1}{I_{xy}} \end{bmatrix} \begin{pmatrix} F_x \\ F_z \\ M_\theta \\ M_\phi \end{pmatrix}$$

$$y = \begin{bmatrix} 1 & 0 & 0 & 0 & 0 & 0 & 0 & 0 \\ 0 & 1 & 0 & 0 & 0 & 0 & 0 & 0 \\ 0 & 0 & 1 & 0 & 0 & 0 & 0 & 0 \\ 0 & 0 & 0 & 1 & 0 & 0 & 0 & 0 \\ 0 & 0 & 0 & 0 & 1 & 0 & 0 & 0 \\ 0 & 0 & 0 & 0 & 0 & 1 & 0 & 0 \\ 0 & 0 & 0 & 0 & 0 & 0 & 1 & 0 \\ 0 & 0 & 0 & 0 & 0 & 0 & 0 & 1 \end{bmatrix} \begin{pmatrix} x \\ z \\ \theta \\ \phi \\ \dot{x} \\ \dot{z} \\ \dot{\theta} \\ \dot{\phi} \end{pmatrix} \quad (3.141)$$

3.6.2. CONTROL OF THE TOTAL SYSTEM

Now that the total system is constructed in a state space representation it is time to choose for which case the controller will be tuned. There are 2 variables that play an important role in the eigenfrequency of the system. The first one is the crane wire length as shown in Section 3.3.2. The crane wire length directly influences the added mass due to its dependence on the submerged length. In Figure 3.16 the Bode plot of the input of a disturbance is shown from a moment in θ around the y -axis (M_θ) to the angle of θ . This input can be the moment the waves create on the monopile and the effect that it has on the monopile angle. As expected the first eigenfrequencies follow the same trend as shown in Figures 3.4 and 3.5. Note that these are not exactly the same values as previously where the control moment gyroscope's inertia and mass were not added. However, the weight and inertia of the CMG compared to the total system is small and thus no large changes are to be expected. The typical wave frequencies are also considered when picking the case to be tuned. From the experience of TWD the typical wave periods are between 5 and 10 seconds which equals a frequency of 0.2Hz and 0.1Hz . This is typical for workable conditions of an H_s around 2.5m .

As can be seen in Figure 3.16 3 cases have been shown. For the cases with a submergence of 5m and 15m their eigenfrequencies fall within that range. Therefore, both will encounter waves at the natural frequency of the system. As 15m of submergence is halfway the final depth of 30m it is chosen as well as that the eigenfrequency is right in the wave frequency range.

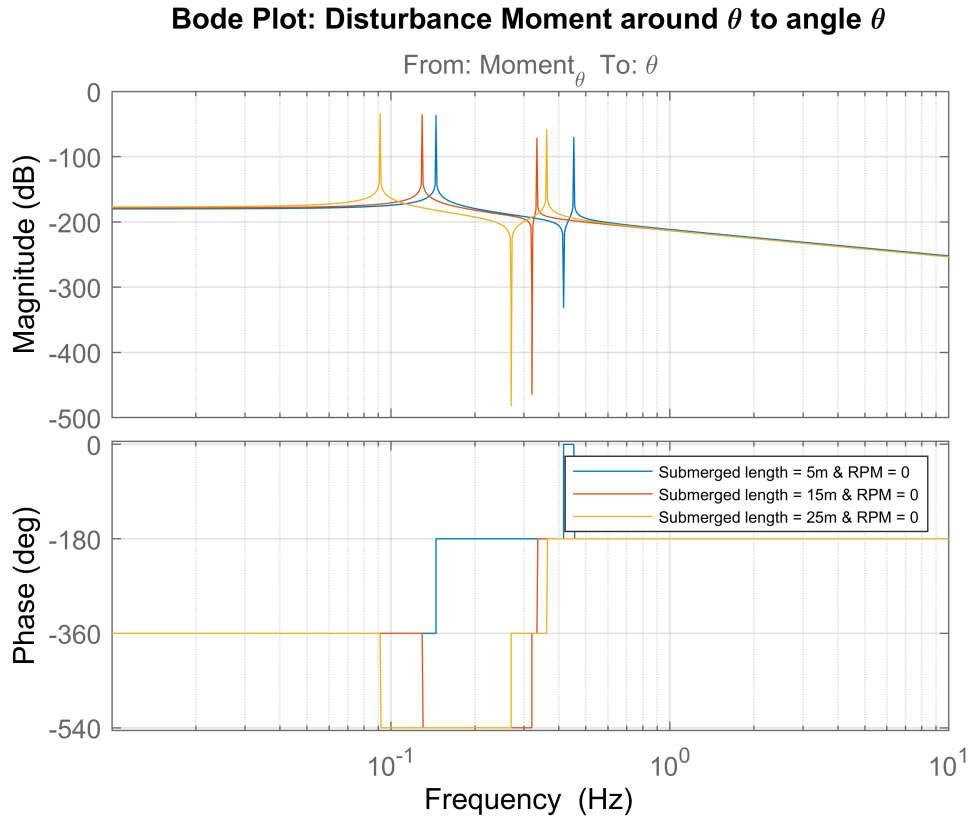


Figure 3.16: Bode plot from the moment around θ to the angle θ for different submerged depths

The second variable that has an influence on the natural frequencies is the angular velocity of the flywheel. The effect that the angular velocity has is shown in Figure 3.17. It can be observed that the effect of the CMG is mainly on the first eigenfrequency and makes the system stiffer as the eigenfrequency becomes higher. How much the frequency shifts is dependent on the angular velocity of the flywheel and its inertia around its spinning axis.

For the second eigenfrequency the frequency does not deviate much from the case where there is no spin. The cause for this is due to the fact that this eigenfrequency is mostly caused by the gripper stiffness. If a simple sanity check is done by only considering the gripper and the monopile then a simple mass spring system is

assumed. The mass is the total mass in x -direction m_x and the spring stiffness is $k_{gripper}$. Equation 3.142 can then be used to calculate the eigenfrequency. This is shown for a submergence of 15m. The mass for 15m submergence is $2.50 \cdot 10^6 kg$ and a gripper stiffness of $10.00 \cdot 10^6 kN/m$. Which is almost precisely what it is in Figure 3.17 for 15m submergence.

$$f_{15} = \sqrt{\frac{k_{gripper}}{m_x}} = 0.32 Hz \tag{3.142}$$

It is also worth noting that the eigenfrequency has now moved out of the frequency range of the waves. This might indicate that by choosing the right spinning velocity for certain wave conditions a passive system is sufficient to reduce the off and side lead of the crane wire. This will be further discussed in Chapter 4. Keep in mind that the eigenfrequency is probably not distanced enough from the wave frequency to not feel the influence of the disturbances.

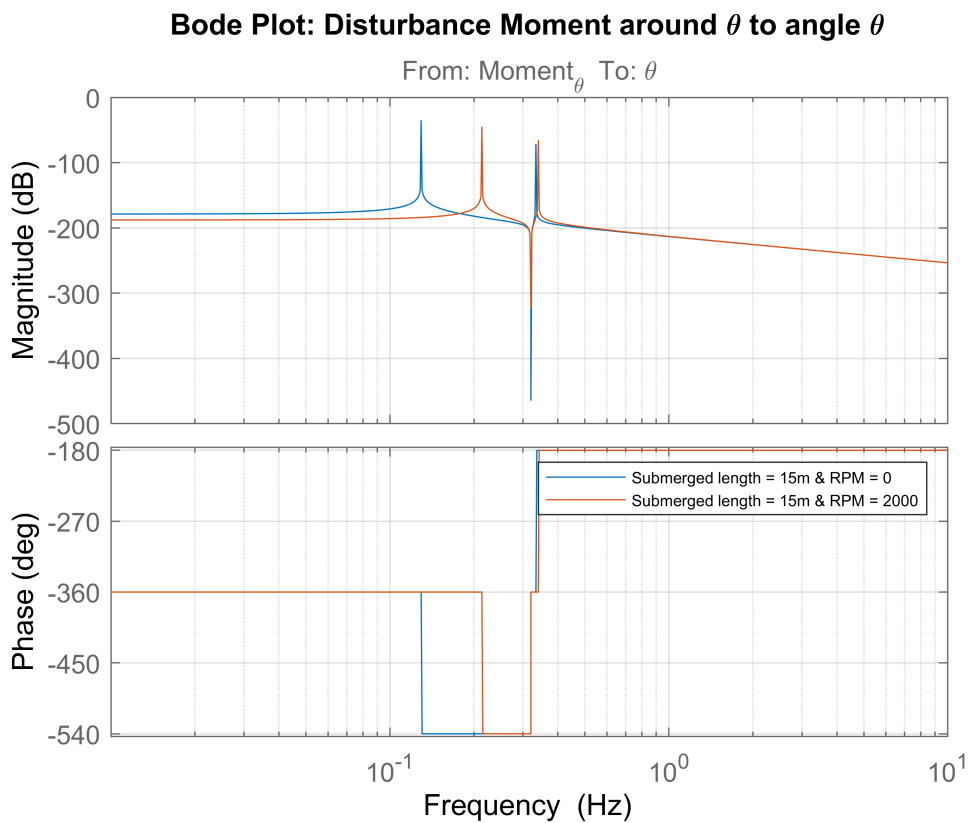


Figure 3.17: Bode plot from the moment around θ to the angle θ for different spinning velocities

In order to tune the controller for the control moment gyroscope to keep the monopile angle to a minimum the actual angle that is actively controlled is the one of the flywheel, ϕ . This can be done due to their dependence on each other due to the cross terms $\dot{\phi}$ and $\dot{\theta}$. This is what is called a full procession state controller as the controller is fully dependent on the state variables of the CMG and not directly of the monopile angle. An advantage of this system is that the monopile does not need a roll motion sensor [27]. The Bode plot from the input as a moment around ϕ to the angle ϕ is given in Figure 3.18. The line of the monopile and CMG combination shows the Bode plot of the system without its controller.

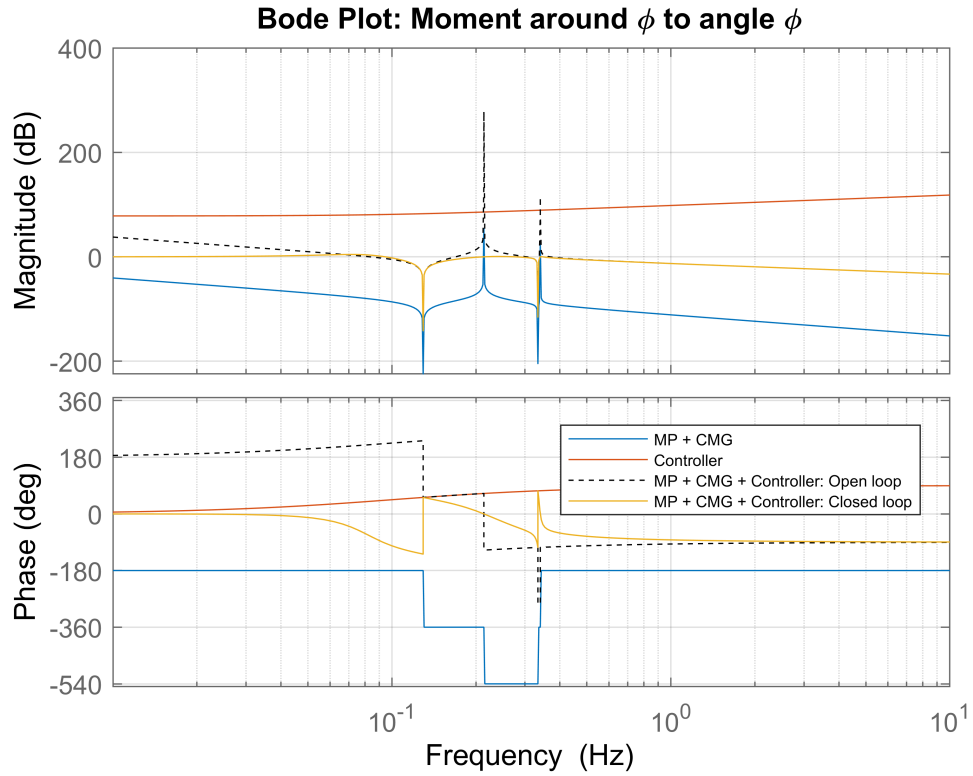


Figure 3.18: Bode plot from the moment around ϕ to the angle ϕ

Following the methods described in Section 2.2 and shown in Section 3.4.1 a bandwidth has to be set for which the gain is determined for the monopile and CMG system. In this case a crossover frequency is chosen of $f_c = 0.3\text{Hz}$. This crossover frequency is chosen according to two criteria which turn out to be two conflicting criteria. Therefore, a compromise has been made. The first criteria is that the bandwidth should encompass the wave frequencies that are acting on the monopile. Where typically a higher bandwidth leads to a better performance. However, this bandwidth should also be physically possible. The second criteria is that the disturbance output from moment created by the waves on the monopile to monopile angle should be as low as possible in the wave frequency range. Finally the bandwidth was selected to be 0.3Hz . Higher bandwidths were tried but resulted in less favourable outcomes for the disturbance plots.

The crossover frequency leads to the frequencies at which the differential and integral part of the controller start and stop. This is done in equations 3.143 and 3.144 both computed in radians per seconds. The corresponding gain of "MP + CMG" system is $G_{dB} = -87.8\text{dB}$ at $f_c = 0.3\text{Hz}$. This is used to get the total gain K_t in Equation 3.145. Using the total gain and the frequencies the proportional and differential gain are derived using equations 3.146 and 3.147.

$$\omega_d = \frac{2\pi f_c}{3} = 0.63\text{rad} \cdot \text{s}^{-1} \quad (3.143)$$

$$\omega_i = 2\pi \cdot 0.1 \cdot f_c = 0.19\text{rad} \cdot \text{s}^{-1} \quad (3.144)$$

$$K_t = -\frac{1}{10^{\frac{G_{dB}}{20}}} = 2.45 \cdot 10^4 \text{N} \cdot \text{m} \cdot \text{rad}^{-1} \quad (3.145)$$

$$K_p = \frac{K_t}{3} = 8.18 \cdot 10^3 \text{N} \cdot \text{m} \cdot \text{rad}^{-1} \quad (3.146)$$

$$K_d = \frac{K_p}{\omega_d} = 1.30 \cdot 10^4 \text{N} \cdot \text{m} \cdot \text{s} \cdot \text{rad}^{-1} \quad (3.147)$$

When looking at the controller curve it can be observed that the integral gain is set to 0. Adding the integrator is of no use when looking at the closed loop system. This is because the curve follows the $0dB$ line at low frequencies and thus the effect of an integrator (which operates in this frequency range) is redundant. When these gains are used the open loop and closed loop are created. As before the open loop is only used to determine its stability. While the closed loop shows the actual performance of the new system with controller. Again it can be seen that the closed loop system is close to the $0dB$ line and the resonance peaks are damped out and are almost non-existent except for the anti-resonance peaks. The figure also shows that the open loop system is stable as the phase plot does not cross 180 degrees near a point where the magnitude crosses the $0dB$ line. The phase minimum margin is 39.8 degrees.

Now that the controller is tuned to control ϕ . However, a positive effect should translate to the angle θ as well. Therefore in Figure 3.19 the transfer function from the moment around θ to the angle θ is given again. Focussing on the red line, it can be seen that the original monopile and control moment gyroscope line have been damped out and no more resonance peak can be seen. This means that if a disturbance, such as waves, create a moment on the monopile the resulting angle of θ will be much smaller. The effect will be most noticeable near its resonance frequency.

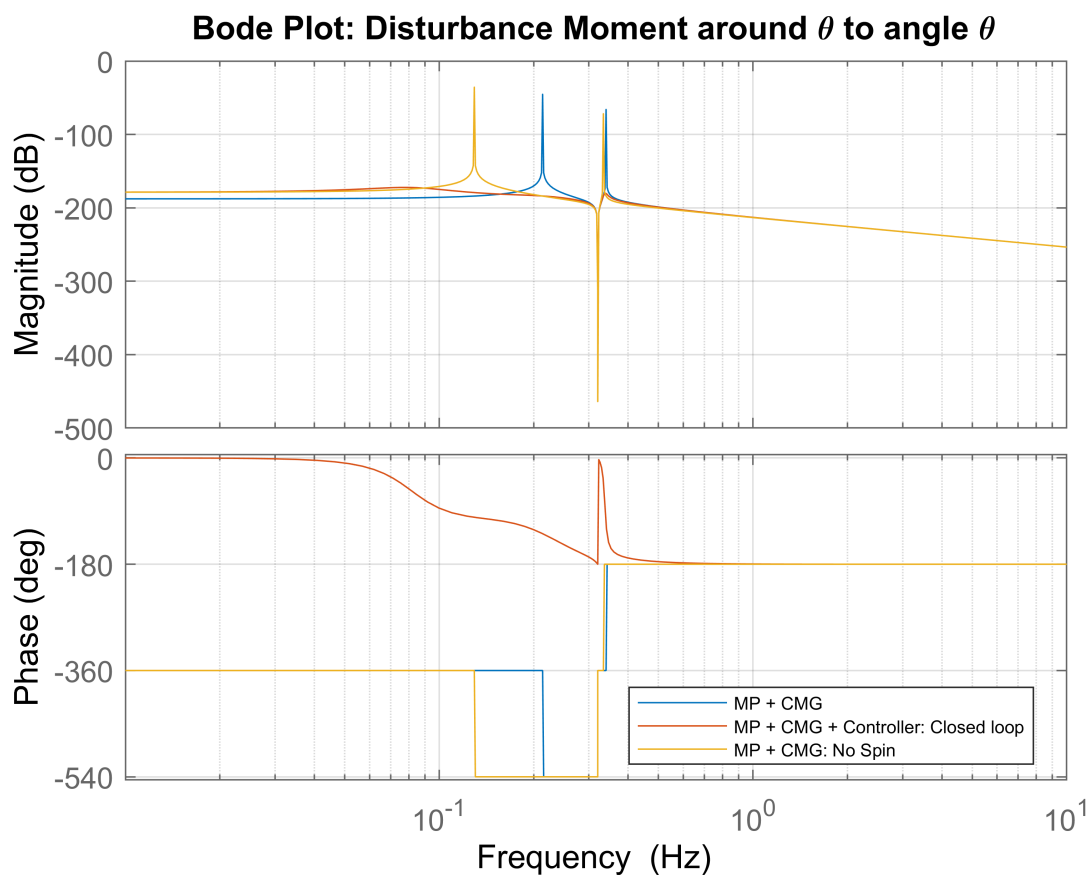


Figure 3.19: Bode plot from the moment around θ to the angle θ to see the effect of a disturbance force such as waves creating a moment on the monopile

3.7. ORCAFLEX PYTHON INTEGRATION

In order to get the CMGs physical characteristics in OrcaFlex a Python script is used. This Python script consists the PID controller as well as the state space involved to represent the CMG. Figure 3.20 shows the flow chart and the exchange of information from OrcaFlex to Python and vice versa. As can be seen it is the monopile angle θ that goes from OrcaFlex into Python and the CMG moment that acts on the pile is the output that goes into OrcaFlex again. In essence the state space is split up into the monopile part, in OrcaFlex, and the gyroscope part, in python. OrcaFlex calculates the movement of the monopile while Python calculates the CMG motions and forces.

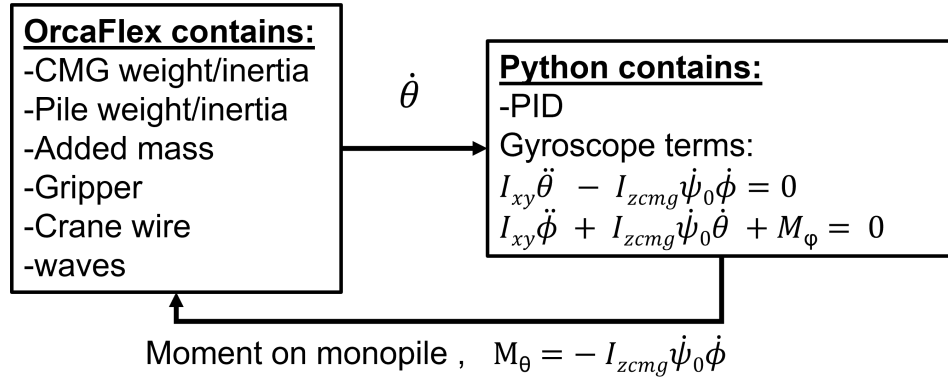


Figure 3.20: The flowchart of the interaction between OrcaFlex and Python during each iteration of the calculation

The state space in the Python script is shown in Equation 3.148. Where M_ϕ is the moment that is put on the flywheel. This is the moment that the PID controller provides. The moment is determined using the theory explained in Section 2.2.5 and is shown in Equation 3.149. The output, M_θ , is the moment exerted on the monopile by the CMG which is then imported into OrcaFlex for the next iteration.

$$\begin{pmatrix} \dot{\phi} \\ \ddot{\phi} \end{pmatrix} = \begin{bmatrix} 0 & 1 \\ 0 & 0 \end{bmatrix} \begin{pmatrix} \phi \\ \dot{\phi} \end{pmatrix} + \begin{bmatrix} 0 & 0 \\ -\frac{I_{zcmg}\dot{\psi}_0}{I_{xycmg}} & \frac{1}{I_{xycmg}} \end{bmatrix} \begin{bmatrix} \dot{\theta} \\ M_\phi \end{bmatrix} \quad (3.148)$$

$$M_\theta = \begin{bmatrix} 0 & I_{xycmg}\dot{\psi}_0 \end{bmatrix} \begin{pmatrix} \dot{\phi} \\ \ddot{\phi} \end{pmatrix}$$

$$M_\phi = K_p(\phi_{ref} - \phi) + K_d \frac{\partial(\phi_{ref} - \phi)}{\partial t} \quad (3.149)$$

4

RESULTS

In this chapter the results will be discussed of the models that are developed in previous chapters. First the results of the MATLAB model will be elaborated on in order to get a better understanding of the behaviour of the system. This is followed by a discussion of the results of the OrcaFlex model including the CMG.

4.1. RESULTS OF TUNED CMG ON MONOPILE IN MATLAB

To better understand the results of the bode plots that are given in Section 3.6.2 a simulation is run in MATLAB where the monopile is subjected to a sinusoidal moment. This sinusoidal moment could be seen as the moment waves might produce on the monopile. The monopile is subjected to a moment that has a frequency that falls within the wave frequency range. For this instance the frequency is chosen to be 0.17Hz which coincides with a wave period of 5.8 seconds. This frequency is chosen as it is between the 2 eigenfrequencies of the system with a rotating CMG and the one without rotation as shown in Figure 3.17. The moment that acts on the monopile is $10 \cdot 10^3 \text{ kNm}$. The chosen amplitude of the moment is not important as the output is linear with respect to the input. Doubling the input moment will give double the output motion. In order to see the effect of the CMG there are 3 systems that are examined. These 3 systems are the system with CMG and controller (active system), the system with CMG and no controller (passive system) and the base case where the CMG is on the monopile but is not spinning i.e. only the inertia and mass are included and thus the gyroscopic effect is not accounted for .

The disturbance signal that is used as an input is displayed in Figure 4.1. As mentioned before it is a sinusoidal moment acting around the y -axis of the monopile in the θ direction. The result in the angle θ is given in Figure 4.2. It can be seen that the system where the CMG is not spinning has the largest angle deviations up to 1.8 degrees as is to be expected. The passive system is an improvement to the base case due to the shift of the eigenfrequency, the system has become stiffer, and therefore the eigenfrequency is further removed from the excitation frequency. The maximum angle the passive system makes is 1.2 degrees. The actively controlled system which has a maximum deviation of 0.9 degrees is the best in this situation. Even though this is only mimicking wave loads, the effect of a gyrostabilizer can be seen as the effect this particular gyroscope in this test shows a reduction of 31% for the passive system compared to system where the CMG is not spinning. The motion in the fully controlled system has been reduced with 50%.

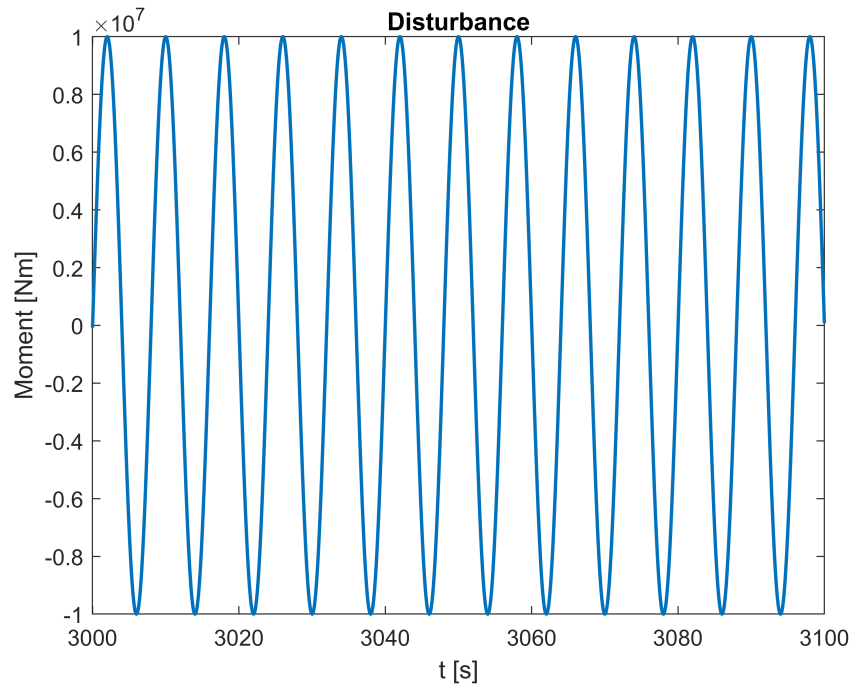


Figure 4.1: The sinusoidal disturbance moment around θ

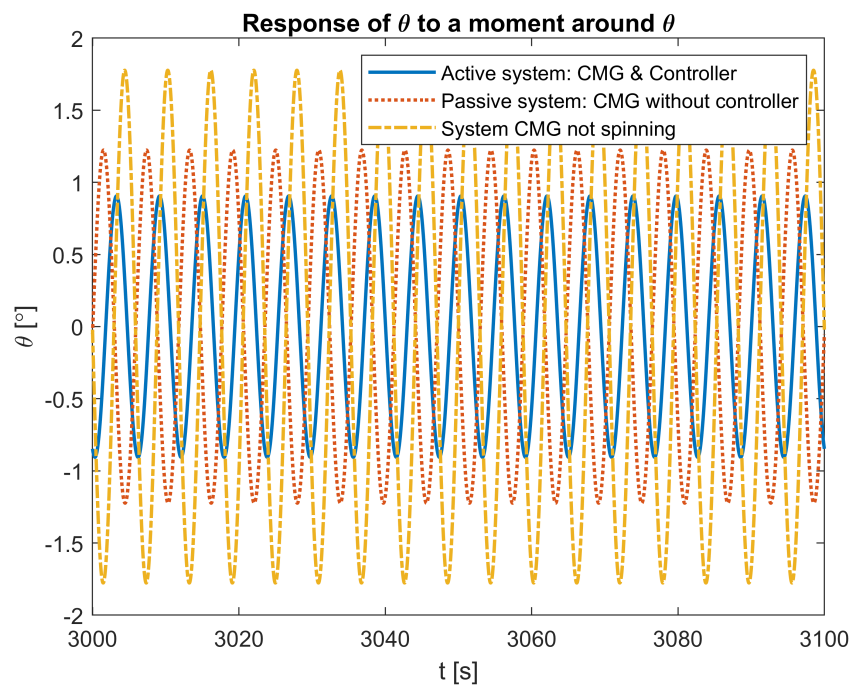


Figure 4.2: Response of monopile angle θ to a sinusoidal disturbance moment input around θ

These results show the same as what the bode plots depict in a more intuitive manner. Although it is hard to see in Figure 3.19 at 0.17 Hz the system that is not spinning is less negative than the passive and active control line. This means that any disturbance input is followed more closely. Therefore the disturbance moment has a greater effect on the monopile angle than in the cases where the CMG is spinning. The active system has the lowest frequency response curve which also shows in the lowest output of angle compared to the other two systems.

When looking at Figure 3.19 it can already be deduced that if a lower frequency is chosen for the disturbing force then a passive controller might give more favourable results. To illustrate this the result of a sinusoidal input with an 8s period with the same amplitude as before is given in Figure 4.3. This period corresponds to a frequency of 0.13Hz . As to be expected the results for the passive system are better i.e. lower amplitude of θ .

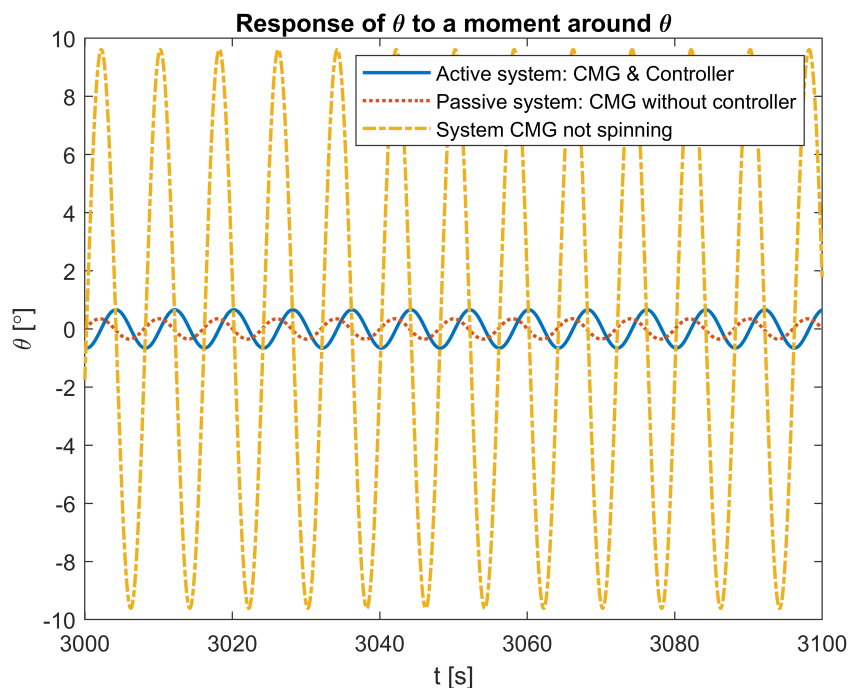


Figure 4.3: Response of monopile angle θ to a sinusoidal disturbance moment input around θ with a frequency of 0.13Hz . ($T_p = 8\text{s}$)

It should be noted that in order to get these figures to correspond with the bode plots a small amount of damping is introduced. The reason for this is that when a sudden force is introduced to the system it acts as a step response. A step response excites all frequencies and therefore the behaviour of the single frequency input would not be as clear. Due to the small amount of damping that is added over time the other frequencies will damp out and the steady state behaviour is seen that can be observed in the figures. The damping is small enough so that the amplitude difference from the undamped system is negligible. Especially, since the disturbance frequencies are not at the resonance frequencies where damping has a larger impact.

4.2. ORCAFLEX MODEL RESULTS

In the OrcaFlex simulations a sea state is used instead of a sinusoidal excitation consisting of a single frequency. A wave train is a group of waves of different frequencies simulating the wave conditions of a sea state. The sea state used has a significant wave height of $H_s = 2m$ and according to [5] and explained in Section 2.3.2 the range of wave periods can be calculated by using Equation 2.72 which is stated again for convenience in equation 4.1. Using the specified significant wave height the range of wave periods is from 5 to 8 seconds. The simulations will be run for every T_p from 5 to 8 with steps of 0.5s. This will therefore be done for 7 simulations per system. The peakedness factor discussed in the same section is calculated with equation 4.2. An overview is given in Table 4.1 for the simulations run for each system. The 3 systems are: CMG not spinning, passive system and actively controlled. This will give a better idea on the performance of the systems due to the range of frequencies/periods used. By doing this for the total T_p range a better understanding is gained of the behaviour of how the system behaves in this sea state. Each simulation will be run with a submerged depth of 15 meters and for 10800 seconds which equates to 3 hours with a time step of 0.05 seconds. Note, there is also a fourth line shown in the result plots. This line is the limited actively controlled system. More on this at the end of this section.

$$\sqrt{13H_s} < T_p < \sqrt{30H_s} \quad (4.1)$$

$$\begin{aligned} \gamma &= 5 \quad \text{for} \quad \frac{T_p}{\sqrt{H_s}} \leq 3.6 \\ \gamma &= e^{5.75 - 1.15 \frac{T_p}{\sqrt{H_s}}} \quad \text{for} \quad 3.6 < \frac{T_p}{\sqrt{H_s}} < 5 \\ \gamma &= 1 \quad \text{for} \quad 5 \leq \frac{T_p}{\sqrt{H_s}} \end{aligned} \quad (4.2)$$

Table 4.1: The peak periods used in the simulations with their corresponding peak enhancement factors according to DNVGL [5]

Peak period T_p [s]	Peak enhancement factor γ [-]
5.0	5.00
5.5	3.59
6.0	2.39
6.5	1.59
7.0	1.06
7.5	1.00
8.0	1.00

The spectral density plot of the wave frequencies is shown in Figure 4.4 for a T_p of 8 seconds. This is shown as an example to illustrate that the wave is not a single frequency anymore. From this graph it is evident that there is a big difference between the single frequency input to which the MATLAB model was subjected to and the actual sea state representing reality. However, the most energy is still at the main frequency of 0.13Hz (8 second period).

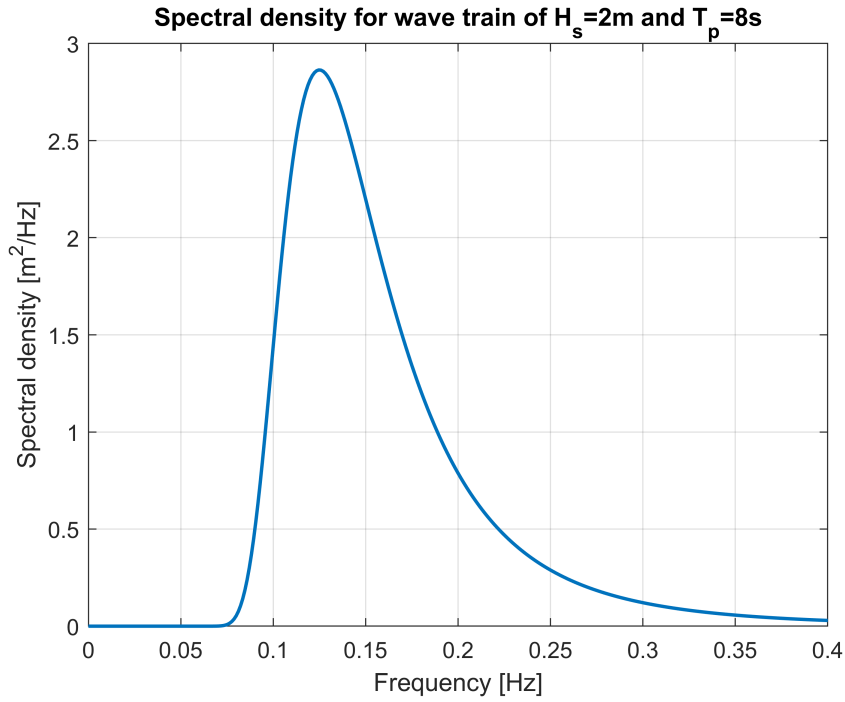


Figure 4.4: Spectral density of a wave train with $H_s = 2m$ and $T_p = 8s$

When looking at the time history results of the simulations, and only considering the maximum values, the result might differ from what is expected. This is due to the randomness of the irregular waves generated. Each seed that can be used to produce a random irregular wave train could therefore produce a different maximum value. To reduce the randomness that is involved in these types of simulation a statistical measure is introduced called the *Most Probable Maximum*, MPM. OrcaFlex uses equation 4.3 to calculate the MPM for the 3 hour simulation. In this equation μ is the mean of the simulation, σ the standard deviation, T the length of the simulation (i.e. 3 hours) and T_z the mean up-crossing period [26]. For a detailed derivation refer to [24].

$$MPM = \mu + \sigma \sqrt{2 \ln \left(\frac{T}{T_z} \right)} \quad (4.3)$$

The results of the determined MPM per T_p of each system is given in Figure 4.5. If the behaviour of the system is considered where the CMG is not spinning then it becomes clear that when the T_p goes from 5 to 8 seconds the maximum angle increases. This makes sense due to the fact the eigenfrequency of the system is around 7.75 seconds (0.129 Hz). However, as concluded in Section 3.3.2 and shown in Figure 3.4 there can be a difference between the eigenfrequencies of the MATLAB and OrcaFlex models up to 12%. With OrcaFlex having the lower frequency of the 2 models. This explains why at 8 seconds the angle is at its highest point as this is closer to its eigenfrequency in OrcaFlex.

If the passive system is examined then the same phenomenon is observed but rather in the lower period ranges. Again, this corresponds to what is seen Figure 3.19. It can be seen that the eigenfrequency of the passively controlled system is at 0.21 Hz . Therefore, it is expected to have a higher monopile angle output to incoming disturbances at shorter wave periods. Another aspect that can be deduced from Figure 4.5 is, when only looking at the CMG that is not spinning and the passive system, is that indeed the passive system can be used to reduce the monopile angle output. This is done by tuning the eigenfrequency of the system in such a manner that the natural frequencies do not coincide with the wave periods. However, in this situation for an H_s of 2 m the corresponding waves periods will still give higher output at the lower periods. Only when the wave period is longer than 6 seconds the passive system performs better. Nonetheless, this passive system might be more beneficial if the system can be made even stiffer. This could be done by a greater angular velocity of the CMG or a larger radius increasing the inertia around its spinning axis.

As expected the actively controlled system outperforms both systems. Except for T_p is 5.5 seconds. Even though, in reality this difference of less than one degree is negligible. When comparing the results in Figure 4.5 with the bode in Figure 3.19, as is done before, then it comes as no surprise that the output is a relatively flat line. The corresponding crane wire angles are shown in Figure 4.6. The same behaviour can be observed here as the angle is directly proportional to the monopile angle.

Another benefit from a control moment gyroscope is the fact that it lowers the forces on the gripper applied by the monopile. This is shown in Figure 4.7. The force on the gripper is the lowest for the actively controlled system. Followed by the system where the CMG is not spinning. The odd figure is the passive system which is higher than all the other systems. This has to do with the fact mentioned earlier when a sea state is considered instead of a single frequency input. Looking at Figure 4.4 it can be seen that there is still quite a bit of energy carried by the waves at the 0.2 Hz frequency which is the eigenfrequency of the system. Therefore, the pile will see some resonance which is partly countered by the passive CMG. However, this will keep the pile more upright and thus will encounter higher wave loads due to the pile staying more vertical in the water. These wave loads are then transferred directly to the gripper.

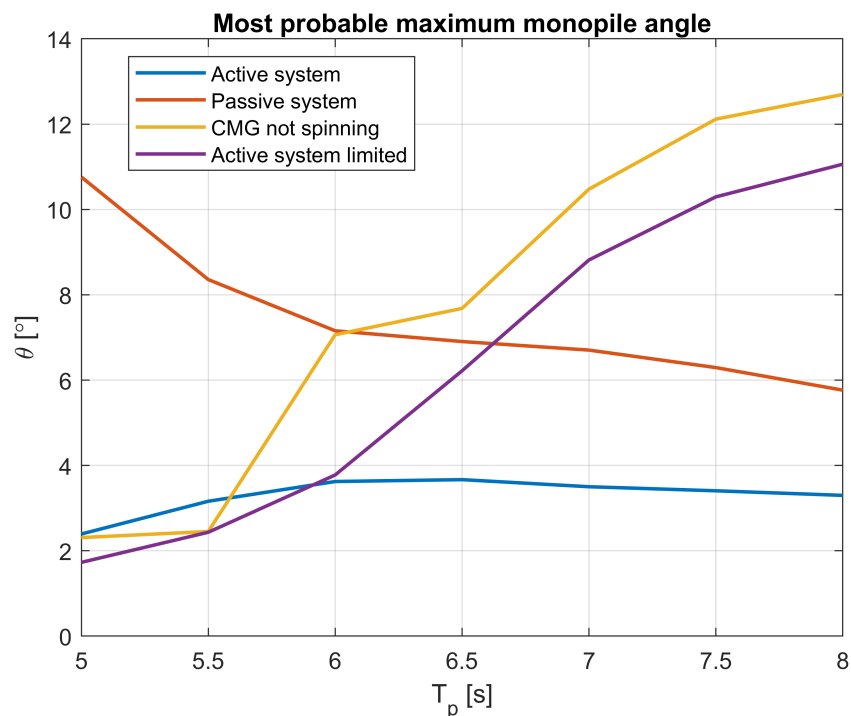


Figure 4.5: Most probable maximum monopile angle θ for whole range of T_p for an H_s of 2 m

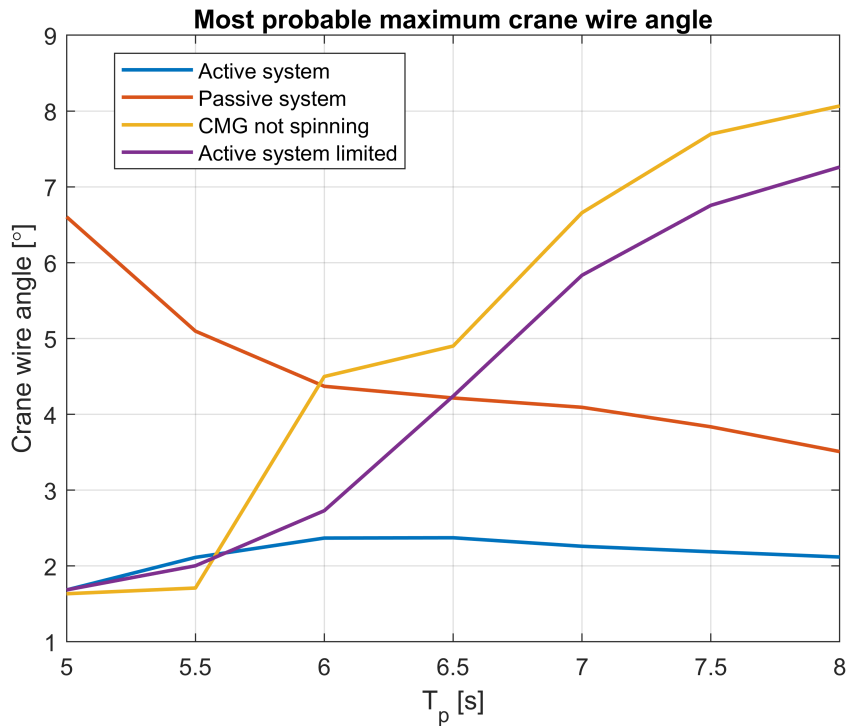


Figure 4.6: Most probable maximum crane wire angles for whole range of T_p for an H_s of 2m

It is important to note that these results are with a CMG that does not have a limited moment. Therefore, the figures show 4 lines. The "active system limited" line is where the maximum CMG moment is capped at 1158kN which is the maximum moment calculated in 3.5.2. What is obvious from this line is that it follows the trend of the system where the CMG is not spinning. However, it performs better along the full range of periods shown. This is the result of the moment not being large enough to fully counteract the forces of the waves on the monopile. If the moment limit is raised the line would tend to follow the behaviour more closely of the system without a limit. Nonetheless, it shows that the performance does increase in this sea state. Meaning lower monopile angles and gripper forces.

To get an idea of the behaviour when the maximum moment is increased the radius will only be increased to 1.7 meters. Adding these 20 centimeters to the radius results in a 50% higher moment output as shown in Figure 3.14 which equates to a maximum moment output of 1737kN. It has to be kept in mind though that same controller is used and thus this controller is not optimally tuned for this new CMG size. The results of the new maximum moment are compared to the maximum moment shown before and are shown in Figure 4.8. It can be seen that it leads to a maximum decrease of the monopile angle of only 7.6%. by increasing the moment the behaviour will start to look more like the active system with no limit on it shown in Figure 4.5. However, when increasing the CMG dimensions the tuning has to be redone to get the optimal results.

When looking at the figures it can be deduced that a well tuned CMG with the proper dimensions could dampen out excessive motions of a monopile while being lowered. It should also be noted that the way this CMG is limited is by applying a direct maximum on the moment applied on the monopile. This is not how the physical CMG moment limitation actually works. In a physical CMG system, the nutation velocity is the limiting factor, thereby indirectly limiting the moment. The limiting factor is the nutation angle this should be limited to 0.3 radians per second. However, this could not be done at this point due to the state space equation being used during each iteration of the python script at each time step in Orcaflex. Therefore, the result might alter when implementing the maximum nutation angle velocity. Another aspect that one should be mindful of is the fact that the equations are linearized. Thus, as explained earlier the moment can be maintained even after the angle is not considered small any more.

It becomes clear that that the chosen CMG does not deliver enough moment to notably damp the monopile motions by quite large amount. Thus in future iterations the output moment should be increased. Options for increasing the output moment are: increasing the rotational velocity of the CMG ring, increasing the maximum velocity of the nutation angle ϕ or changing the dimensions of the CMG. At this point not a lot of research is done to see what the possibilities are in this particular configuration and should be looked into further in a future study. This goes beyond the objective of this research.

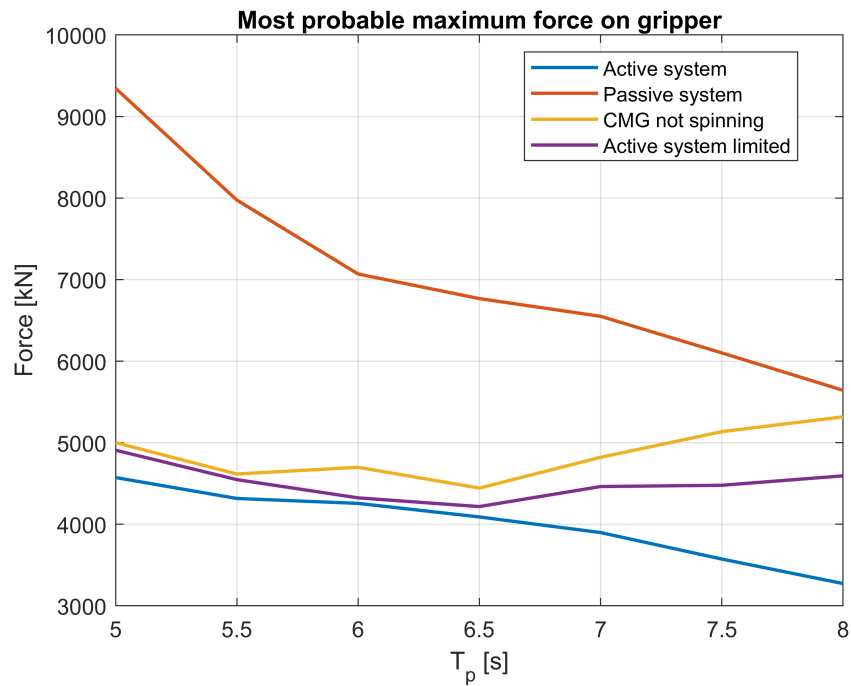


Figure 4.7: Most probable maximum force on gripper for whole range of T_p for an H_s of 2m

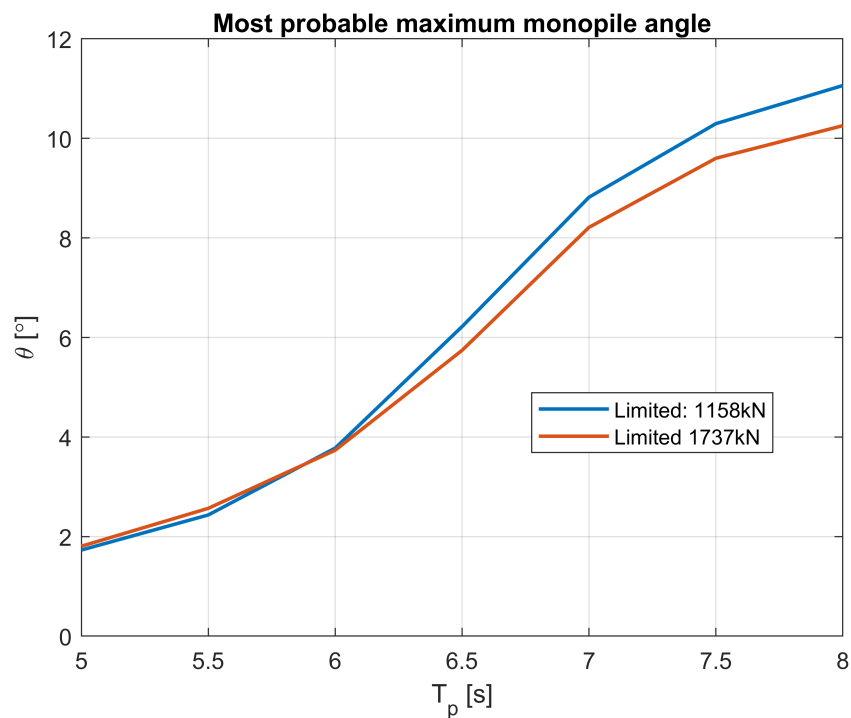


Figure 4.8: Comparison of two systems with a capped maximum moment to see the effect of a larger moment

5

CONCLUSION AND RECOMMENDATIONS

The objective of this chapter is to explain the findings of the work performed in this report and to discuss possible points of interest for future research. First a conclusion of the research done will be discussed after which the recommendations are elaborated up on.

5.1. CONCLUSION

In order to increase the workability of monopile installations one of the main aspects of the installation process has been revised: Lowering of the monopile to the seabed. This was done with the purpose of reducing the crane wire angle of the crane wire which is proportional to the monopile angle. The reduction in excessive monopile motion will be controlled with the use of a gyroscopic actuator. This is in correspondence with the main research objective stated in the introduction and again below for completeness sake.

Optimize the workability of offshore installations of monopiles by using gyroscopic motion actuators.

As a means to achieve the main objective sub-objective were established. Each sub-objective is listed below accompanied by their main findings determined during this thesis.

DETERMINE BEST SUITABLE GYROSCOPE ACTUATOR SYSTEM TO CONTROL EXCESSIVE MOTIONS OF A MONOPILE SUSPENDED ON A CRANE.

During the literature study performed ahead of thesis it was determined that the most suitable gyroscopic actuator is the control moment gyroscope. CMGs can create a larger moment with respect to reaction wheels with any given amount of momentum capacity that the rotating disk can store. A downside is that the equations of motion are more complex and therefore tuning the controller is more challenging.

SET UP THE COMPUTER MODEL OF THE MONOPILE, GYROSTABILIZER, GRIPPER AND CRANE SYSTEM.

In Chapter 3 a model is created in MATLAB. The model describes the motion of a suspended monopile partly submerged in water and held in place by a gripper. The equations of motion are constructed using the Lagrange method. This model consists of the monopile which is suspended from a crane by a crane wire, a gripper and the trapped and added mass due to the submerged part of the monopile. Both the gripper and crane wire are modelled as a spring. The same has been done in OrcaFlex to validate the MATLAB model. This was done by comparing the eigenfrequencies. It was determined in section 3.3.2 that the model's resemblance is close enough for a controller to be tuned in MATLAB, as this can not be done in OrcaFlex, and then be used in OrcaFlex in order to simulate real wave conditions. A submerged length of 15 meters was used as the eigenfrequency of the system will be directly in the range of wave frequencies.

The control moment gyroscope (CMG) is later added to the system as a means to actuate the monopile and mitigate the excessive motions of the monopile due to wave loads. The main finding when looking at the

equations of the control moment gyroscope is that the moment is dependent on the nutation velocity (angular velocity of the spinning plane of the CMG), inertia of the CMG and the angular velocity of the CMG. Changing any of these parameters will affect and/or limit the moment output of the system. The chosen system has a maximum moment 1158 kN. Which is to be believed to be a realistic limit given the size and weight constraints. and the current state of the art CMG technologies. This maximum is only for small nutation angles as the moment created will always work on a perpendicular plane essentially reaching 0 at a 90 degree nutation angle for the desired moment axis. This effect is not accounted for due to the linearization of the equations.

DETERMINE EIGENFREQUENCY OF THE TOTAL SYSTEM.

The models that were constructed in Chapter 3 are then used to analyse the behaviour of the system. The eigenfrequencies were determined for each meter of the lowering process: from 0 to 30 meters of submergence. It is determined that the eigenfrequency is sensitive to the crane wire length and the amount of trapped and added mass in and around the monopile. The first natural frequency will start to decrease especially after 10 meters of submergence due to the longer length of the wire and increased water mass.

The frequencies are also highly dependent on the CMG used. The finding is that the system becomes stiffer, natural frequency increases, when the angular velocity of the system is increased when looking at a passive system, i.e. no controller but the CMG is spinning.

ADD A WAVE SPECTRUM THAT INCLUDE THE EIGENFREQUENCIES OF THE SYSTEM.

The wave spectrum that is used in the OrcaFlex model is the JONSWAP spectrum. This was chosen as this spectrum describes the conditions on the North Sea where wind farms are a common sight. With the chosen significant wave height (H_s) of 2 meters the corresponding periods (T_p) range from 5 to 8 seconds. As shown in section 4.2 this sea state is made up of a whole range of waves with different frequencies each carrying a certain amount of energy. However, most energy is concentrated at each of the periods corresponding frequency.

CREATE CONTROLLER FOR THE GYROSTABILISATION SYSTEM AND INCORPORATE IT INTO THE COMPLETE MODEL TO TEST EFFECT.

The MATLAB model constructed in section 3.6.2 was used to tune a controller for the CMG. It was determined that a Proportional-Derivative (PD) controller was the best option as the integral part of the controller had little to no effect. This is due to the fact that the integrator works at the low frequency range and in this range the CMG has a negligible effect on the system. The reason for this is that at low frequencies the angular velocity of the nutation angle is low and thus the moment created is small as the moment is directly related to the moment output.

The nutation angle is used for the feedback loop in the controller instead of the monopile angle. This can be done due to the nutation angle being proportional to the monopile angle. This is known as a full precession state controller as the controller is fully dependent on the state variables of the CMG and not directly of the monopile angle. Therefore, there is no extra device needed to measure the monopile angle. The gains are tuned in such a manner that the disturbance input on the monopile angle is damped so that the resonance peaks in the bode plots are almost non existent.

A python script has been created to simulate the PD controller and the CMG in the OrcaFlex software. This is done because a CMG can not be easily modelled within OrcaFlex. For each period a simulation was run for 3 hours with a time step of 0.05. This was done for 4 variants of the system: CMG on the pile but not spinning, passive control system where the CMG is spinning but does not include a controller and 2 actively controlled systems where one is limited to the physical capacity of the CMG and the other one is not. The results clearly indicate that the best system is the actively controlled system. It has the most consistent crane wire angles over the range of periods considered. With respect to the system where the CMG is not spinning it distinctly shows that the resonance frequency is damped out and the angles are more or less equal for all different T_p values. This is in direct contrast with the system where the CMG is not spinning where large crane wire angles are seen at the period coinciding with the eigenfrequencies. The passive system shows the same behaviour

as the CMG not spinning system with respect to having clear resonance frequencies. However, the peak is in the higher frequency range instead of the lower frequencies as the system is stiffer due to the CMG and large crane wire angles are observed in this area.

The results reveal that overall a system with a controller performs best. It has the most consistent results and lowers the most probable maximum crane wire and monopile angles, especially, near the resonance frequency of the original system. The monopile angle reduces by an average of 49% and in the best scenario 74%. The average decrease of the crane wire angle over the periods considered is 48%. The maximum reduction in crane wire angle is 74%. Not only does it performs best when looking at the angles of the monopile and crane wire it also shows the most promising results when looking at the forces that the monopile applies on the gripper with a mean reduction in force of 17% and a maximum reduction of 38%. Which could lead to less costly grippers. Due to the fact that they have to withstand smaller loads and thus can be smaller leading to a snowball effect, i.e. smaller gripper, easier design, reduced steel weight, saving deck space etc. These are all cost saving aspects.

However, when the physical limitations are considered that hold for the CMG moment, by capping out the moment at $1158kN$, the added value of a CMG is limited to an average reduction in monopile angle of around 20% and for the crane wire angle it is 15%. The gripper force is reduced by an average of 7% while at the most optimal period the reduction is 13%.

MAIN OBJECTIVE

This study shows that having a properly tuned CMG on the monopile can be beneficial when installing monopiles. It clearly shows that the crane wire angle is reduced, the motion of the monopile is damped and gripper loads are decreased. This can either lead to less complicated grippers which also takes up less deck space or being able to operate in sea state with a higher significant wave height with the same equipment. The latter will effectively lead to a higher workability of the monopile installations.

However, the improvements gained by the limited system are not as large and at this point might not be worthwhile building the system as is. The limited system should be examined in more detail using a method that resembles the physical workings of having a limit to the maximum moment. Nevertheless, both options are able to install monopiles in rougher weather conditions which will lead to less downtime of the operation. Both options will make the installation of offshore wind farms less expensive and therefore more economically viable. This will make offshore wind farms an even more suitable option for renewable energy production during and after the transition from fossil fuels.

5.2. RECOMMENDATION

There are a number of recommendations that could aid future studies on the topic. Some recommendations are made to make the results more true to reality while others point future researchers in a specific direction on what to investigate or improve on.

INCLUDE WAVES IN MATLAB

The MATLAB model can be extended to generate the wave structure interaction more realistically. A code that generates the randomness of sea states and calculates the correct wave forces on the pile could avoid the use of OrcaFlex. This could save computational time because the interaction between OrcaFlex and the Python script makes the simulation slower.

INCLUDE 3D EFFECTS

The created models are in 2D. As most motions only occur in the wave direction it is a good approximation of what would happen in the 3D case. However, the next step should be to include this in the actual modelling. This should be done to see the impact of the CMG in a 3D environment and finding ways to solve occurring problems, if any. This could give more insight whether or not the CMG affects the movement around the other axis and if a separate CMG is needed to constrain that movement.

NON-LINEAR EQUATIONS OF MOTION AND CONTROL METHODS

In this study the equations of motion are linearized in order to use them in a state space representation and to use the preferred method of tuning the controller explained in section 3.4.1. However, as the CMG is quite a non-linear system consisting of many sine and cosine terms it would be more precise if this was not linearized around the equilibrium point. This would result in the need for more intricate non-linear control tuning methods as well. Nonetheless, this could also lead to improved performance of the system and is worth analyzing this in future studies.

OPTIMIZATION OF THE CMG SIZE

A study to gain the optimal size of a possible CMG should be done in order to get a better understanding of the possibilities. This should include but not be limited to the following aspect:

- A study into the actual size of the disk/ring
- The nutation velocity and the spinning velocity
- Size and weight limits should be determined keeping an eye on the ever changing size of the monopiles
- Integration in an upend/lifting tool
- Power requirements

Another important aspect is the economical side. A cost-benefit analysis/study should be performed to see whether or not it is within financially possible limits. This is quite an intricate and extensive study as these are just some of the variables involved in getting this idea off the drawing table and into practice.

A

EQUATIONS OF MOTION OF A PENDULUM

To make the theory that is explained in chapter 2 easier to comprehend, a simple example of the methods discussed is given below. The example that is explained is that of a pendulum. The method below follows the steps explained in 2 in order to get the equations of motion, the linearized model and the state space model. The first step is to describe the mechanical system's motion. This could be done using the x and z coordinates. However, the system can be described using only one generalized coordinates. As can be seen in Figure A.1 the position of mass m can be defined by just one general coordinate which is the angle of the pendulum θ . The length L is a constant and therefore not a general coordinate. The x and z position are shown in equation A.1 and the generalized coordinates and its derivatives are shown in equation A.2.

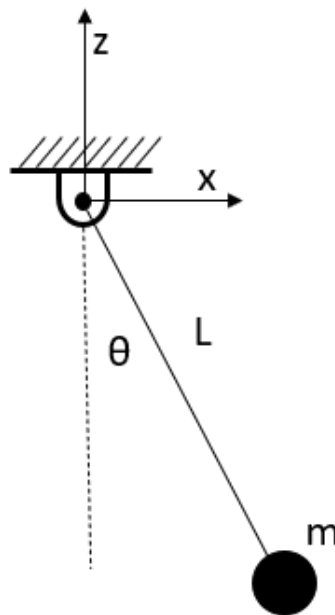


Figure A.1: Single pendulum

$$x = L \sin \theta \qquad z = -L \cos \theta \qquad (\text{A.1})$$

$$q = [\theta] \qquad \dot{q} = [\dot{\theta}] \qquad \ddot{q} = [\ddot{\theta}] \qquad (\text{A.2})$$

Now that the location of the mass is defined the next step is to determine the kinetic and potential energy. To do this the velocities of the mass are needed and thus the positions are differentiated with respect to time. The velocities are shown in equation A.3.

$$\dot{x} = L\dot{\theta} \cos\theta \qquad \dot{z} = L\dot{\theta} \sin\theta \qquad (\text{A.3})$$

Now using the equations for velocity in x and z direction and substituting them in equation A.4 will lead to the results shown in equation A.5.

$$T_x = \frac{1}{2} m_p \dot{x}^2 \qquad T_z = \frac{1}{2} m_p \dot{z}^2 \qquad (\text{A.4})$$

$$T_x = \frac{1}{2} m_p (L\dot{\theta} \cos\theta)^2 \qquad T_z = \frac{1}{2} m_p (L\dot{\theta} \sin\theta)^2 \qquad (\text{A.5})$$

Adding the kinetic energies in both directions will give the total kinetic energy which is shown in equation A.6.

$$T = T_x + T_z \qquad \rightarrow \qquad T = \frac{1}{2} m_p L^2 \dot{\theta}^2 \qquad (\text{A.6})$$

After the kinetic energy is determined the potential energy has to be defined. As the mass is solely connected to the massless and infinitely stiff beam, which makes it rotate about the pivot point, the only potential energy the system has is that of gravity. This equation is given in equation A.7

$$V = -g m_p L \cos\theta \qquad (\text{A.7})$$

The equations of motion using Lagrangian mechanics stated in equation 2.31 is shown below for convenience, A.8. This equation turns into equations A.9 which is just a single equation due to there being only one general coordinate. Each term is calculated and filled in to get the final equations of motion for a simple pendulum which is shown in equation A.13.

$$\frac{d}{dt} \left(\frac{\partial T}{\partial \dot{q}_j} \right) - \frac{\partial T}{\partial q_j} + \frac{\partial V}{\partial q_j} = Q_j, \quad j = 1 \dots n_d \qquad (\text{A.8})$$

$$\frac{d}{dt} \left(\frac{\partial T}{\partial \dot{\theta}} \right) - \frac{\partial T}{\partial \theta} + \frac{\partial V}{\partial \theta} = 0 \qquad (\text{A.9})$$

$$\frac{d}{dt} \left(\frac{\partial T}{\partial \dot{\theta}} \right) = L^2 m_p \ddot{\theta} \qquad (\text{A.10})$$

$$\frac{\partial T}{\partial \theta} = 0 \qquad (\text{A.11})$$

$$\frac{\partial V}{\partial \theta} = L g m_p \sin\theta \qquad (\text{A.12})$$

$$\ddot{\theta} = -\frac{g}{L} \sin\theta \qquad (\text{A.13})$$

It can be seen that even a simple example of a pendulum is a non linear equation due to the sine term. The next step is to linearize this problem using the steps explained in chapter 2.1.2. To obtain the mass and stiffness matrices of the equation of motion. The equations that are needed are stated again for convenience. First the stiffness matrix will be determined using equation A.14. After which the mass matrix is determined in a similar fashion shown in equation A.15.

$$k_{sr} = \left. \frac{\partial^2 V}{\partial q_s \partial q_r} \right|_{q_{eq}} \qquad \rightarrow \qquad k_{11} = \left. \frac{\partial^2 g m_p (L - L \cos\theta)}{\partial \theta^2} \right|_{q_{eq}=0} = L g m_p \qquad (\text{A.14})$$

$$m_{sr} = \left. \frac{\partial^2 T}{\partial \dot{q}_s \partial \dot{q}_r} \right|_{q_{eq}} \rightarrow m_{11} = \left. \frac{\partial^2 \frac{1}{2} L^2 m_p \dot{\theta}^2}{\partial \dot{\theta}^2} \right|_{q_{eq}=0} = L^2 m_p \quad (\text{A.15})$$

$$m\ddot{q} + kq = 0 \rightarrow m_p \ddot{\theta} + \frac{g}{L} m_p \theta = 0 \quad (\text{A.16})$$

Now that the mass and stiffness matrices are known they can be used to build the state space model. The regular state space format is shown in equations A.17. In order to get the A , B , C and D_{ss} matrices the first step is to isolate \ddot{q} as shown in equation A.19. Since there is only one generalized coordinate the mass matrix $M = m_{11}$. The same is valid for the stiffness matrix $K = k_{11}$. No damping is assumed thus the damping matrix $D = 0$. The input vector u can be used to add any external forces e.g. torque at the pivot point of the pendulum to control its motion. Where B_0 specifies on which variable the force acts, which in this example can only be θ .

$$\dot{x} = Ax + Bu \quad (\text{A.17})$$

$$y = Cx + D_{ss}u \quad (\text{A.18})$$

$$\ddot{q} + M^{-1}D\dot{q} + M^{-1}Kq = M^{-1}B_0u \quad (\text{A.19})$$

Following the step shown in equation A.19 this will turn in to equation A.20

$$\ddot{q} + M^{-1}Kq = M^{-1}B_0u \rightarrow \ddot{q} + \frac{g}{L}\theta = \frac{B_0}{m_p L^2}u \quad (\text{A.20})$$

The state vector is shown below in equation A.21 if the generalized coordinates of a pendulum are used.

$$x = \begin{pmatrix} x_1 \\ x_2 \end{pmatrix} = \begin{pmatrix} q \\ \dot{q} \end{pmatrix} = \begin{pmatrix} \theta \\ \dot{\theta} \end{pmatrix} \quad (\text{A.21})$$

Rewriting equation A.21 will lower the order from the equation of motion from second order to first order differential equation leading to the following set of equations describing the motion of the system using the state space formulation.

$$\dot{x}_1 = x_2, \quad (\text{A.22})$$

$$\dot{x}_2 = -\frac{g}{L}x_1 + \frac{B_0}{m_p L^2}u \quad (\text{A.23})$$

$$y = C_{oq}x_1 + C_{ov}x_2 \quad (\text{A.24})$$

In equation A.24 the output matrix C is built up out of the displacement matrix and the velocity matrix C_{oq} and C_{ov} , respectively.

For the purpose of demonstration let the final state space equation describe an input (u) acting on the system and as an output show the displacement and the velocities. Thus, B_0 , C_{oq} and C_{ov} will be 1. The A , B , and C matrices are obtained by using equation A.25 and the result is shown in equation A.26. The D_{ss} matrix will be 0 as this is the feedthrough/feedforward matrix which is 0 in this example.

$$A = \begin{bmatrix} 0 & I \\ -M^{-1}K & -M^{-1}D \end{bmatrix}, \quad B = \begin{bmatrix} 0 \\ M^{-1}B_0 \end{bmatrix}, \quad C = [C_{oq} \quad C_{ov}] \quad (\text{A.25})$$

$$A = \begin{bmatrix} 0 & 1 \\ -\frac{g}{L} & 0 \end{bmatrix}, \quad B = \begin{bmatrix} 0 \\ \frac{1}{m_p L^2} \end{bmatrix}, \quad C = \begin{bmatrix} 1 & 0 \\ 0 & 1 \end{bmatrix} \quad (\text{A.26})$$

$$\begin{pmatrix} \dot{x}_1 \\ \dot{x}_2 \end{pmatrix} = \begin{bmatrix} 0 & 1 \\ -\frac{g}{L} & 0 \end{bmatrix} \begin{pmatrix} x_1 \\ x_2 \end{pmatrix} + \begin{bmatrix} 0 \\ \frac{1}{m_p L^2} \end{bmatrix} u \quad (\text{A.27})$$

$$y = \begin{bmatrix} 1 & 0 \\ 0 & 1 \end{bmatrix} \begin{pmatrix} x_1 \\ x_2 \end{pmatrix} \quad (\text{A.28})$$

Now that it is in state space form a controller can be designed to keep θ steady around one of its equilibrium positions, in this case the pendulum with $\theta = 0$ thus pointing downward is stable equilibrium. However, when θ equals π there is an unstable equilibrium and it is the configuration where the pendulum is pointing directly upwards.

B

EQUATIONS OF MOTION OF A PENDULUM ON A CART

To further support the theory given in Chapter 2 and to give more insight on how to approach a problem that involves multiple generalized coordinates the example of a pendulum on a cart will be discussed. This particular example has 2 degrees of freedom ($n_d = 2$), 4 states ($n = 4$), one input ($s = 1$) and 4 outputs ($r = 4$). As can be seen in Figure B.1 the cart with mass m_c is constrained so that it can only move in the x direction and is attached to a spring. The Pendulum is attached to the cart, the angle the pendulum makes is θ and has mass m_p . Thus the generalized coordinates are x and θ as shown below together with their derivatives in equation B.1.

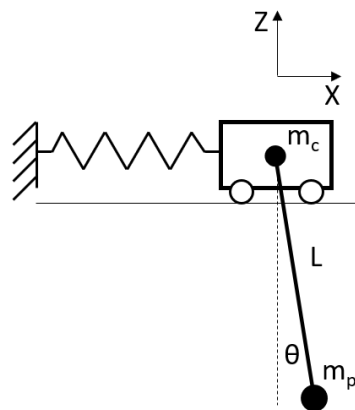


Figure B.1: Cart pendulum

$$q = \begin{bmatrix} x_c \\ \theta \end{bmatrix} \quad \dot{q} = \begin{bmatrix} \dot{x}_c \\ \dot{\theta} \end{bmatrix} \quad \ddot{q} = \begin{bmatrix} \ddot{x}_c \\ \ddot{\theta} \end{bmatrix} \quad (\text{B.1})$$

The location of the cart is solely dependent on x as it is constrained in z direction. The position of the pendulum mass m_p is almost identical to that of a simple pendulum (refer to Appendix A) apart for the exception that in this configuration it is dependent on the cart's position as well. Using the equations given in B.2 and B.3 the position and the velocities can be determined of the cart and pendulum. Subscript c indicates that this variable is that of the cart while the p denotes to the pendulum mass.

$$x_p = x_c + L \sin \theta \quad z_p = -L \cos \theta \quad (\text{B.2})$$

$$\dot{x}_p = \dot{x}_c + L \dot{\theta} \cos \theta \quad \dot{z}_p = L \dot{\theta} \sin \theta \quad (\text{B.3})$$

Now the kinetic energy of the system can be determined, shown in equations B.4 to B.6.

$$T_c = \frac{1}{2} m_c \dot{x}_c^2 \quad T_p = \frac{1}{2} m_p (\dot{x}_p^2 + \dot{z}_p^2) \quad (\text{B.4})$$

$$T_c = \frac{1}{2} m_c \dot{x}_c^2 \quad T_p = \frac{1}{2} m_p (L^2 \dot{\theta}^2 + 2 \cos \theta L \dot{\theta} \dot{x}_c + \dot{x}_c^2) \quad (\text{B.5})$$

$$T = T_c + T_p \quad \rightarrow \quad T = m_p L \dot{\theta} \dot{x}_c \cos \theta + \frac{1}{2} ((m_c + m_p) \dot{x}_c^2 + m_p L^2 \dot{\theta}^2) \quad (\text{B.6})$$

The potential energy is built up by the potential energy of the spring and gravity.

$$V = \frac{1}{2} k_{spring} x_c^2 - L g m_p \cos \theta \quad (\text{B.7})$$

Now that the potential and kinetic energy are known equation B.8 can be used to determine the equations of motion. Each term for $q_1 = x_c$ is given in equations B.10 to B.12.

$$\frac{d}{dt} \left(\frac{\partial T}{\partial \dot{q}_j} \right) - \frac{\partial T}{\partial q_j} + \frac{\partial V}{\partial q_j} = Q_j, \quad j = 1, 2 \quad (\text{B.8})$$

$$\frac{\partial T}{\partial \dot{q}_1} = \frac{\partial T}{\partial \dot{x}_c} = \dot{x}_c (m_c + m_p) + L m_p \dot{\theta} \cos \theta \quad (\text{B.9})$$

$$\frac{d}{dt} \left(\frac{\partial T}{\partial \dot{q}_1} \right) = \frac{d}{dt} \left(\frac{\partial T}{\partial \dot{x}_c} \right) = -L m_p \dot{\theta}^2 \sin \theta + \ddot{x}_c (m_c + m_p) + L m_p \ddot{\theta} \cos \theta \quad (\text{B.10})$$

$$\frac{\partial T}{\partial q_1} = \frac{\partial T}{\partial x_c} = 0 \quad (\text{B.11})$$

$$\frac{\partial V}{\partial q_1} = \frac{\partial V}{\partial x_c} = k_{spring} x_c \quad (\text{B.12})$$

substituting these equations into equation B.8 will give equation B.13

$$\ddot{x}_c (m_c + m_p) - L m_p \dot{\theta}^2 \sin \theta + L m_p \ddot{\theta} \cos \theta + k_{spring} x_c = 0 \quad (\text{B.13})$$

The same can be done for $q_2 = \theta$. This is shown in equations B.15 to B.17

$$\frac{\partial T}{\partial \dot{q}_2} = \frac{\partial T}{\partial \dot{\theta}} = L m_p (L \dot{\theta} + \dot{x}_c \cos \theta) \quad (\text{B.14})$$

$$\frac{d}{dt} \left(\frac{\partial T}{\partial \dot{q}_2} \right) = \frac{d}{dt} \left(\frac{\partial T}{\partial \dot{\theta}} \right) = L^2 m_p \ddot{\theta} + L m_p \ddot{x}_c \cos \theta - L m_p \dot{\theta} \dot{x}_c \sin \theta \quad (\text{B.15})$$

$$\frac{\partial T}{\partial q_2} = \frac{\partial T}{\partial \theta} = -L m_p \dot{\theta} \dot{x}_c \sin \theta \quad (\text{B.16})$$

$$\frac{\partial V}{\partial q_2} = \frac{\partial V}{\partial \theta} = L g m_p \sin \theta \quad (\text{B.17})$$

$$L m_p (L \ddot{\theta} + g \sin \theta + \ddot{x}_c \cos \theta) = 0 \quad (\text{B.18})$$

The next step is to linearize the equation around the equilibrium position to get the linearized stiffness and mass matrices. Following the element wise differentiation around the equilibrium point given in section 2.1.2, per element this is shown in equations B.19 to B.21 for the linearized stiffness matrix. The result is the linearized stiffness matrix shown in B.23.

$$k_{11} = \left. \frac{\partial^2 V}{\partial x_c^2} \right|_{q_{eq}=0} = k_{spring} \quad (\text{B.19})$$

$$k_{12} = k_{21} = \left. \frac{\partial^2 V}{\partial x_c \partial \theta} \right|_{q_{eq}=0} = 0 \quad (\text{B.20})$$

$$k_{22} = \left. \frac{\partial^2 V}{\partial \theta^2} \right|_{q_{eq}=0} = L g m_p \quad (\text{B.21})$$

$$(\text{B.22})$$

$$K = \begin{bmatrix} k_{spring} & 0 \\ 0 & L g m_p \end{bmatrix} \quad (\text{B.23})$$

The mass matrix elements are given in equations B.24 to B.26. The final result is the mass matrix given in B.28.

$$m_{11} = \left. \frac{\partial^2 T}{\partial \dot{x}_c^2} \right|_{q_{eq}=0} = m_c + m_p \quad (\text{B.24})$$

$$m_{12} = m_{21} = \left. \frac{\partial^2 T}{\partial \dot{x}_c \partial \dot{\theta}} \right|_{q_{eq}=0} = L m_p \quad (\text{B.25})$$

$$m_{22} = \left. \frac{\partial^2 T}{\partial \dot{\theta}^2} \right|_{q_{eq}=0} = L^2 m_p \quad (\text{B.26})$$

$$(\text{B.27})$$

$$M = \begin{bmatrix} m_c + m_p & L m_p \\ L m_p & L^2 m_p \end{bmatrix} \quad (\text{B.28})$$

With no external forces the linearized equations of motion for the cart pendulum system in matrix notation are $M\ddot{q} + Kq = 0$. Next, this equation will be converted into state space form using the same steps as discussed in section 2.1.2 and shown in Appendix A. For convenience the equation used is stated below, equation B.29. The inverse of matrix M is given in equation B.30. No damping is assumed and thus D is 0.

$$A = \begin{bmatrix} 0 & I \\ -M^{-1}K & -M^{-1}D \end{bmatrix}, \quad B = \begin{bmatrix} 0 \\ M^{-1}B_0 \end{bmatrix}, \quad C = [C_{oq} \quad C_{ov}] \quad (\text{B.29})$$

$$M^{-1} = \begin{bmatrix} \frac{1}{m_c} & -\frac{1}{L m_c} \\ -\frac{1}{L m_c} & \frac{1}{L^2 m_c m_p} \end{bmatrix} \quad (\text{B.30})$$

The A matrix is given in B.31. The B matrix is dependent on which variable can be controlled. In this example the cart its position is controlled by exerting a force on it and thus $B_0 = [1, 0]^T$ the result is shown in B.32.

$$A = \begin{bmatrix} 0 & 0 & 1 & 0 \\ 0 & 0 & 0 & 1 \\ -\frac{k_{spring}}{m_c} & \frac{g m_p}{m_c} & 0 & 0 \\ \frac{k_{spring}}{L m_c} & \frac{-g(m_c + m_p)}{L m_c} & 0 & 0 \end{bmatrix} \quad (\text{B.31})$$

$$B = \begin{bmatrix} 0 \\ 0 \\ \frac{1}{m_c} \\ -\frac{1}{L m_c} \end{bmatrix} \quad (\text{B.32})$$

The output matrix C can be chosen, in this case C is chosen such that it outputs the displacements of both x and θ and their derivatives. Therefore the C matrix will be an identity matrix with dimensions 4x4 shown in B.33.

$$C = \begin{bmatrix} 1 & 0 & 0 & 0 \\ 0 & 1 & 0 & 0 \\ 0 & 0 & 1 & 0 \\ 0 & 0 & 0 & 1 \end{bmatrix} \quad (\text{B.33})$$

The D matrix is equal to 0. The final result in state space form is given below in equations B.35 to B.36. With x given in

$$x = \begin{pmatrix} x_1 \\ x_2 \\ x_3 \\ x_4 \end{pmatrix} = \begin{pmatrix} q_1 \\ q_2 \\ \dot{q}_1 \\ \dot{q}_2 \end{pmatrix} = \begin{pmatrix} x \\ \theta \\ \dot{x} \\ \dot{\theta} \end{pmatrix} \quad (\text{B.34})$$

$$\dot{x} = Ax + Bu \quad (\text{B.35})$$

$$\begin{pmatrix} \dot{x}_1 \\ \dot{x}_2 \\ \dot{x}_3 \\ \dot{x}_4 \end{pmatrix} = \begin{bmatrix} 0 & 0 & 1 & 0 \\ 0 & 0 & 0 & 1 \\ -\frac{k_{spring}}{m_c} & \frac{gm_p}{m_c} & 0 & 0 \\ \frac{k_{spring}}{Lm_c} & \frac{-g(m_c+m_p)}{Lm_c} & 0 & 0 \end{bmatrix} \begin{pmatrix} x_1 \\ x_2 \\ x_3 \\ x_4 \end{pmatrix} + \begin{bmatrix} 0 \\ 0 \\ \frac{1}{m_c} \\ -\frac{1}{Lm_c} \end{bmatrix} u \quad (\text{B.36})$$

$$y = \begin{bmatrix} 1 & 0 & 0 & 0 \\ 0 & 1 & 0 & 0 \\ 0 & 0 & 1 & 0 \\ 0 & 0 & 0 & 1 \end{bmatrix} \begin{pmatrix} x_1 \\ x_2 \\ x_3 \\ x_4 \end{pmatrix} \quad (\text{B.37})$$

C

MATLAB CODE EXAMPLE

The following is the code used to solve the equations of motion of the system which are derived in Chapter 3 and the theory behind it is explained in Chapter 2.1.1.

```
1 clear all; close all; clc; clearvars;
2 %=====
3 %%%%          PART 1          %%%%
4 %=====
5 syms x          real
6 syms z          real
7 syms theta     real
8 syms g          real
9 syms m_tot     real
10 syms L_cgtot   real
11 syms D_g       real
12 syms k_wire    real
13 syms k_gripper real
14 syms L_w       real
15 syms L_0       real
16 syms L_e       real
17 syms I         real
18 syms L_0stretch real
19
20 %=====
21 %%%          Define kinematic relations and dof %%%
22 %=====
23 %position of Hook wrt cg equilibrium
24 Hx = x - L_cgtot * sin(theta);
25 Hz = z + L_cgtot * cos(theta);
26
27 %position of gripper
28 Gx = x + (D_g+z)*tan(theta);
29
30 % Generalized DoF
31 q = [x, z, theta];
32
33 %% =====
34 %%%% Build energies T and V %%%
35 %=====
36 syms x_d      real
37 syms z_d      real
38 syms theta_d  real
39
40 % DoF
41 q_d = [x_d, z_d theta_d];
42
43 x_d = jacobian(x,q)*q_d.';
44 z_d = jacobian(z,q)*q_d.';
45 theta_d = jacobian(theta,q)*q_d.';
46
```

```

47
48 %% Define kinetic energy (T)
49 T_x      = 1/2 * m_tot * x_d^2    ;
50 T_z      = 1/2 * m_tot * z_d^2    ;
51 T_theta  = 1/2 * I * theta_d^2   ;
52
53 T        = simplify(T_x + T_z + T_theta);
54
55
56 %% Elongated crane wire length
57
58 %Total crane wire length
59 L_w = sqrt( Hx^2 + Hz^2 );
60
61 %Elongated length
62 L_w0 = L_0 ;
63 L_e  = L_w - L_w0;
64
65
66 %% Define potential energy (V)
67 V_gravity = m_tot * g * z;
68 V_wire    = 1/2 * k_wire * L_e^2;
69 V_gripper = 1/2 * k_gripper * Gx^2;
70
71 V        = V_gravity + V_wire + V_gripper ;
72
73 %% =====%
74 %%% Find Lagrange Equations %%%
75 %=====%
76 %=====%
77 %%% D(dT/dqd)/Dt - dT/dq + dV/dq - Q = 0 %
78 %%%=====%
79 % second time derivatives of dofs
80 syms theta_dd      real
81 syms x_dd          real
82 syms z_dd          real
83 syms t              real
84
85 q_dd = [x_dd, z_dd, theta_dd];
86
87 % - compute dT/dqd
88
89 dT_dqd = simplify(jacobian(T,q_d).'); % note: transposed used to adjust dimension
90 % use "." and not "." alone for ...
% transposed, otherwise Matlab/Maple ...
% assumes a complex conj. transposed !
91
92 % - compute D(dT/dqd)/Dt
93 % --> total D/Dt of dT/dqd = partial d(dT/dqd)/dt
94 % + d(dT/dqd)/dq*dq
95 % + d(dT/dqd)/dq*dqdd
96 DdT_Dtdqd = (jacobian(dT_dqd,t)) ...
97 + (jacobian(dT_dqd,q)) * q_d.' ...
98 + (jacobian(dT_dqd,q_d)) * q_dd. ';
99 % - compute dT/dq
100 dT_dq = (jacobian(T,q)).' ;
101 % - compute dV/dq
102 dV_dq = (jacobian(V,q)).' ;
103 %- Set up equations
104 Equations = DdT_Dtdqd - dT_dq + dV_dq;
105
106 %% =====%
107 %%% Linearized equations of motion %%%
108 %=====%
109 Main_vars_rev2ForAppendix;
110
111 M = simplify(jacobian(dT_dqd,q_d));
112 C = simplify(jacobian(DdT_Dtdqd - dT_dq,q_d));%NOTE, that this matrix=0
113 C = simplify(subs(C,q_d,[0 0 0]));
114 C = simplify(subs(C,q_dd,[0 0 0]));
115 K = simplify(jacobian(dV_dq,q));

```



```

116 %equilibrium position
117 x_eq          = 0; %m
118 z_eq          = -(L_0+L_cgtot+L_0stretch); %m
119 theta_eq     = 0.0; %rad
120
121 q_eq = [x_eq, z_eq, theta_eq] ;
122
123 %actual linearized matrices
124 M_eq = M;
125 K_eq = K;
126
127 for i = 1:length(q_eq)
128     M_eq = subs(M_eq,q(i),q_eq(i));
129     K_eq = subs(K_eq,q(i),q_eq(i));
130 end
131
132
133 %% =====%
134 %%% Eigenfrequencies %%%
135 %=====%%
136 KK = double(subs(K_eq));
137 MM = double(subs(M_eq));
138 [EV,EF] = eig(KK,MM);
139 EFHz = sqrt(EF)/(2*pi)
140
141 %normalize eigenvectors so that they add up to 1
142 for n = 1: size(EV,2)
143     a = norm(EV(:,n));
144     EV(:,n) = EV(:,n)/a;
145 end
146
147 %% =====%
148 %%% Build state space %%%
149 %=====%%
150 % used: Chapter 2 [Gawronski] Advanced Structural Dynamics and Active Control of ...
      Structures.pdf
151 MK = subs(-inv(M_eq) * K_eq);
152
153 % For clarity: X = [x, z, theta, x_d, z_d, theta_d]=[X1, X2, X3, X4, X5, X6]
154 %               X_d = [X4, X5 X6, X4_d, X5_d, X5_d]
155
156 A = [zeros(length(q),length(q)), eye(length(q),length(q));
157      MK, zeros(length(q),length(q))];
158
159
160 B0 = [0 0 1];
161 BOM_eq = [inv(M_eq) * B0.'].';
162 B = [0,0,0, BOM_eq].';
163
164 %for C matrix give all states as output thus identity matrix
165 % (size should be number of outputs* (2*DOF)
166 C = [eye(2*length(q),2*length(q))];
167
168 D = zeros(size(C,1),size(B,2));%No damping assumed

```


D

POTENTIAL ENERGY DERIVATIVES

The equations below are the derivatives of the potential energy of the system described in Chapter 3. The MATLAB code shown in Appendix C gives the following equations for the derivatives of the potential energy of the system with respect to x , z and θ .

$$\frac{\partial V}{\partial x} = \frac{k_{gripper}(2x + 2 \tan \theta (D_g + z))}{2} - \frac{k_{wire} \left(L_0 - \sqrt{(z + L_{cgtot} \cos \theta)^2 + (x - L_{cgtot} \sin \theta)^2} \right) (2x - 2L_{cgtot} \sin \theta)}{2\sqrt{(z + L_{cgtot} \cos \theta)^2 + (x - L_{cgtot} \sin \theta)^2}} \quad (D.1)$$

$$\frac{\partial V}{\partial z} = gm_z + k_{gripper} \tan \theta (x + \tan \theta (D_g + z)) - \frac{k_{wire} \left(L_0 - \sqrt{(z + L_{cgtot} \cos \theta)^2 + (x - L_{cgtot} \sin \theta)^2} \right) (2z + 2L_{cgtot} \cos \theta)}{2\sqrt{(z + L_{cgtot} \cos \theta)^2 + (x - L_{cgtot} \sin \theta)^2}} \quad (D.2)$$

$$\frac{\partial V}{\partial \theta} = \frac{k_{wire} (2L_{cgtot} \cos \theta (x - L_{cgtot} \sin \theta) + 2L_{cgtot} \sin \theta (z + L_{cgtot} \cos \theta)) \left(L_0 - \sqrt{(z + L_{cgtot} \cos \theta)^2 + (x - L_{cgtot} \sin \theta)^2} \right)}{2\sqrt{(z + L_{cgtot} \cos \theta)^2 + (x - L_{cgtot} \sin \theta)^2}} + k_{gripper} (D_g + z) (x + \tan \theta (D_g + z)) (\tan^2 \theta + 1) \quad (D.3)$$

After dividing out the 2 in the fractions and using equations 3.7, 3.9, 3.10 and 3.11 (stated again in equations D.4 to D.7 for convenience) and substituting them in to equations D.1, D.2 and D.3 the simplified equations that are shown in Chapter 3 are obtained. The simplified equations are equations 3.17, 3.22 and 3.27.

$$H_x = x - L_{cgtot} \sin \theta \quad (D.4)$$

$$H_z = z + L_{cgtot} \cos \theta \quad (D.5)$$

$$G_x = x + (D_g + z) \tan \theta \quad (D.6)$$

$$L_e = L_w - L_0 = \sqrt{(x - L_{cgtot} \sin \theta)^2 + (z - L_{cgtot} \cos \theta)^2} - L_0 \quad (D.7)$$

To help the reader that wants to check calculations by hand the derivatives of H_x^2 , H_z^2 and G_x^2 are given. As they are needed when solving for the potential energy derivatives using the chain rule. The trivial solutions

(such as 1 and 0) are not given.

$$\frac{\partial H_x^2}{\partial x} = \frac{\partial (x - L_{cg\,tot} \sin \theta)^2}{\partial x} = 2(x - L_{cg\,tot} \sin \theta) \quad (D.8)$$

$$\frac{\partial H_x^2}{\partial \theta} = \frac{\partial (x - L_{cg\,tot} \sin \theta)^2}{\partial \theta} = -2L_{cg\,tot} \cos \theta (x - L_{cg\,tot} \sin \theta) \quad (D.9)$$

$$\frac{\partial H_z^2}{\partial z} = \frac{\partial (z + L_{cg\,tot} \cos \theta)^2}{\partial z} = 2(z + L_{cg\,tot} \cos \theta) \quad (D.10)$$

$$\frac{\partial H_z^2}{\partial \theta} = \frac{\partial (z + L_{cg\,tot} \cos \theta)^2}{\partial \theta} = -2L_{cg\,tot} \sin \theta (z + L_{cg\,tot} \cos \theta) \quad (D.11)$$

$$\frac{\partial G_x^2}{\partial z} = x + ((D_g + z) \tan \theta)^2 = 2 \tan \theta (\tan \theta (D_g + z) + x) \quad (D.12)$$

The derivative with respect to θ of $\tan \theta$ is equal to \sec^2 with $\sec^2 = \cos^{-2}$. Using $\sin^2 + \cos^2 = 1$ and dividing by \cos^2 gives $\sin^2 \cdot \cos^{-2} + 1 = \cos^{-2}$. With $\tan \theta = \sin \cdot \cos^{-1}$ thus giving $\sin^2 \cdot \cos^{-2} + 1 = \cos^{-2}$ equals to $\tan^2 + 1 = \sec^2$.

$$\frac{\partial G_x^2}{\partial \theta} = \frac{\partial (x + (D_g + z) \tan \theta)^2}{\partial \theta} = 2(D_g + z) ((D_g + z) \tan \theta + x) \sec^2 \theta = 2(D_g + z) (x + \tan \theta (D_g + z)) (\tan^2 \theta + 1) \quad (D.13)$$

E

NONLINEAR STIFFNESS MATRIX ELEMENTS

The elements for the nonlinear stiffness matrix before substitution are given in equations E.1 to E.9. When substitution of terms is performed the equations can be written as equations 3.32 to 3.40 in Chapter 3. The Matrices are created by using the MATLAB code shown in Appendix C.

$$k_{11} = \frac{\partial^2 V}{\partial q_1 \partial q_1} = k_{grripper} - \frac{k_{wire} \left(L_0 - \sqrt{(z + L_{cgtot} \cos \theta)^2 + (x - L_{cgtot} \sin \theta)^2} \right)}{\sqrt{(z + L_{cgtot} \cos \theta)^2 + (x - L_{cgtot} \sin \theta)^2}} + \frac{k_{wire} (x - L_{cgtot} \sin \theta)^2}{(z + L_{cgtot} \cos \theta)^2 + (x - L_{cgtot} \sin \theta)^2} + \frac{k_{wire} \left(L_0 - \sqrt{(z + L_{cgtot} \cos \theta)^2 + (x - L_{cgtot} \sin \theta)^2} \right) (x - L_{cgtot} \sin \theta)^2}{\left((z + L_{cgtot} \cos \theta)^2 + (x - L_{cgtot} \sin \theta)^2 \right)^{3/2}}$$

(E.1)

$$k_{12} = \frac{\partial^2 V}{\partial q_1 \partial q_2} = k_{grripper} \tan \theta + \frac{k_{wire} (2z + 2L_{cgtot} \cos \theta) (2x - 2L_{cgtot} \sin \theta)}{4 \left((z + L_{cgtot} \cos \theta)^2 + (x - L_{cgtot} \sin \theta)^2 \right)}$$

(E.2)

$$+ \frac{k_{wire} \left(L_0 - \sqrt{(z + L_{cgtot} \cos \theta)^2 + (x - L_{cgtot} \sin \theta)^2} \right) (2z + 2L_{cgtot} \cos \theta) (2x - 2L_{cgtot} \sin \theta)}{4 \left((z + L_{cgtot} \cos \theta)^2 + (x - L_{cgtot} \sin \theta)^2 \right)^{3/2}}$$

$$k_{13} = \frac{\partial^2 V}{\partial q_1 \partial q_3} = k_{grripper} (D_g + z) (\tan^2 \theta + 1) + \frac{L_{cgtot} k_{wire} \cos \theta \left(L_0 - \sqrt{(z + L_{cgtot} \cos \theta)^2 + (x - L_{cgtot} \sin \theta)^2} \right)}{\sqrt{(z + L_{cgtot} \cos \theta)^2 + (x - L_{cgtot} \sin \theta)^2}} - \frac{L_{cgtot} k_{wire} (2x - 2L_{cgtot} \sin \theta) (x \cos \theta + z \sin \theta)}{2 \left((z + L_{cgtot} \cos \theta)^2 + (x - L_{cgtot} \sin \theta)^2 \right)} - \frac{L_{cgtot} k_{wire} \left(L_0 - \sqrt{(z + L_{cgtot} \cos \theta)^2 + (x - L_{cgtot} \sin \theta)^2} \right) (2x - 2L_{cgtot} \sin \theta) (x \cos \theta + z \sin \theta)}{2 \left((z + L_{cgtot} \cos \theta)^2 + (x - L_{cgtot} \sin \theta)^2 \right)^{3/2}}$$

(E.3)

$$k_{21} = \frac{\partial^2 V}{\partial q_2 \partial q_1} = k_{gripper} \tan \theta + \frac{k_{wire} (2z + 2L_{cgtot} \cos \theta) (2x - 2L_{cgtot} \sin \theta)}{4 \left((z + L_{cgtot} \cos \theta)^2 + (x - L_{cgtot} \sin \theta)^2 \right)} + \frac{k_{wire} \left(L_0 - \sqrt{(z + L_{cgtot} \cos \theta)^2 + (x - L_{cgtot} \sin \theta)^2} \right) (2z + 2L_{cgtot} \cos \theta) (2x - 2L_{cgtot} \sin \theta)}{4 \left((z + L_{cgtot} \cos \theta)^2 + (x - L_{cgtot} \sin \theta)^2 \right)^{3/2}} \quad (E.4)$$

$$k_{22} = \frac{\partial^2 V}{\partial q_2 \partial q_2} = k_{gripper} \tan^2 \theta - \frac{k_{wire} \left(L_0 - \sqrt{(z + L_{cgtot} \cos \theta)^2 + (x - L_{cgtot} \sin \theta)^2} \right)}{\sqrt{(z + L_{cgtot} \cos \theta)^2 + (x - L_{cgtot} \sin \theta)^2}} + \frac{k_{wire} (z + L_{cgtot} \cos \theta)^2}{(z + L_{cgtot} \cos \theta)^2 + (x - L_{cgtot} \sin \theta)^2} + \frac{k_{wire} \left(L_0 - \sqrt{(z + L_{cgtot} \cos \theta)^2 + (x - L_{cgtot} \sin \theta)^2} \right) (z + L_{cgtot} \cos \theta)^2}{\left((z + L_{cgtot} \cos \theta)^2 + (x - L_{cgtot} \sin \theta)^2 \right)^{3/2}} \quad (E.5)$$

$$k_{23} = \frac{\partial^2 V}{\partial q_2 \partial q_3} = k_{gripper} (\tan^2 \theta + 1) (x + D_g \tan \theta + z \tan \theta) + k_{gripper} \tan \theta (D_g + z) (\tan^2 \theta + 1) + \frac{L_{cgtot} k_{wire} \sin \theta \left(L_0 - \sqrt{(z + L_{cgtot} \cos \theta)^2 + (x - L_{cgtot} \sin \theta)^2} \right)}{\sqrt{(z + L_{cgtot} \cos \theta)^2 + (x - L_{cgtot} \sin \theta)^2}} - \frac{L_{cgtot} k_{wire} (2z + 2L_{cgtot} \cos \theta) (x \cos \theta + z \sin \theta)}{2 \left((z + L_{cgtot} \cos \theta)^2 + (x - L_{cgtot} \sin \theta)^2 \right)} + \frac{L_{cgtot} k_{wire} \left(L_0 - \sqrt{(z + L_{cgtot} \cos \theta)^2 + (x - L_{cgtot} \sin \theta)^2} \right) (2z + 2L_{cgtot} \cos \theta) (x \cos \theta + z \sin \theta)}{2 \left((z + L_{cgtot} \cos \theta)^2 + (x - L_{cgtot} \sin \theta)^2 \right)^{3/2}} \quad (E.6)$$

$$\begin{aligned}
k_{31} = \frac{\partial^2 V}{\partial q_3 \partial q_1} &= k_{gripper} (D_g + z) (\tan^2 \theta + 1) + \frac{L_{cgtot} k_{wire} \cos \theta \left(L_0 - \sqrt{(z + L_{cgtot} \cos \theta)^2 + (x - L_{cgtot} \sin \theta)^2} \right)}{\sqrt{(z + L_{cgtot} \cos \theta)^2 + (x - L_{cgtot} \sin \theta)^2}} \\
&- \frac{L_{cgtot} k_{wire} (2x - 2L_{cgtot} \sin \theta) (x \cos \theta + z \sin \theta)}{2 \left((z + L_{cgtot} \cos \theta)^2 + (x - L_{cgtot} \sin \theta)^2 \right)} \\
&- \frac{L_{cgtot} k_{wire} \left(L_0 - \sqrt{(z + L_{cgtot} \cos \theta)^2 + (x - L_{cgtot} \sin \theta)^2} \right) (2x - 2L_{cgtot} \sin \theta) (x \cos \theta + z \sin \theta)}{2 \left((z + L_{cgtot} \cos \theta)^2 + (x - L_{cgtot} \sin \theta)^2 \right)^{3/2}}
\end{aligned} \tag{E.7}$$

$$\begin{aligned}
k_{32} = \frac{\partial^2 V}{\partial q_3 \partial q_2} &= k_{gripper} (\tan^2 \theta + 1) (x + D_g \tan \theta + z \tan \theta) + k_{gripper} \tan \theta (D_g + z) (\tan^2 \theta + 1) \\
&+ \frac{L_{cgtot} k_{wire} \sin \theta \left(L_0 - \sqrt{(z + L_{cgtot} \cos \theta)^2 + (x - L_{cgtot} \sin \theta)^2} \right)}{\sqrt{(z + L_{cgtot} \cos \theta)^2 + (x - L_{cgtot} \sin \theta)^2}} \\
&- \frac{L_{cgtot} k_{wire} (2z + 2L_{cgtot} \cos \theta) (x \cos \theta + z \sin \theta)}{2 \left((z + L_{cgtot} \cos \theta)^2 + (x - L_{cgtot} \sin \theta)^2 \right)} \\
&- \frac{L_{cgtot} k_{wire} \left(L_0 - \sqrt{(z + L_{cgtot} \cos \theta)^2 + (x - L_{cgtot} \sin \theta)^2} \right) (2z + 2L_{cgtot} \cos \theta) (x \cos \theta + z \sin \theta)}{2 \left((z + L_{cgtot} \cos \theta)^2 + (x - L_{cgtot} \sin \theta)^2 \right)^{3/2}}
\end{aligned} \tag{E.8}$$

$$\begin{aligned}
k_{33} = \frac{\partial^2 V}{\partial q_3 \partial q_3} &= k_{gripper} (D_g + z)^2 (\tan^2 \theta + 1)^2 + \frac{L_{cgtot}^2 k_{wire} (x \cos \theta + z \sin \theta)^2}{(z + L_{cgtot} \cos \theta)^2 + (x - L_{cgtot} \sin \theta)^2} \\
&+ \frac{L_{cgtot}^2 k_{wire} \left(L_0 - \sqrt{(z + L_{cgtot} \cos \theta)^2 + (x - L_{cgtot} \sin \theta)^2} \right) (x \cos \theta + z \sin \theta)^2}{\left((z + L_{cgtot} \cos \theta)^2 + (x - L_{cgtot} \sin \theta)^2 \right)^{3/2}} \\
&+ \frac{L_{cgtot} k_{wire} \left(L_0 - \sqrt{(z + L_{cgtot} \cos \theta)^2 + (x - L_{cgtot} \sin \theta)^2} \right) (z \cos \theta - x \sin \theta)}{\sqrt{(z + L_{cgtot} \cos \theta)^2 + (x - L_{cgtot} \sin \theta)^2}} \\
&+ 2 k_{gripper} \tan \theta (D_g + z) (\tan^2 \theta + 1) (x + D_g \tan \theta + z \tan \theta)
\end{aligned} \tag{E.9}$$

F

CONTROL OF A CART-PENDULUM SYSTEM

In this Appendix the example of the cart pendulum system, Appendix B, is used to create a simple controller. This is done according to the steps discussed in Chapter 2. Here the cart is controlled in order to make sure that the pendulum motion is damped/stabilized. This is done using a PID controller. This controller exerts an external force that moves the cart in order to stabilize the motion of the pendulum after the pendulum is released at a certain angle.

In Table F.1 the dimensions are given that are used in this example. These dimensions include the pendulum length L , spring stiffness k_{spring} and the pendulum and cart masses m_p and m_c , respectively. These values are arbitrarily chosen.

Table F.1: The dimensions of cart pendulum system used in this example

Description	Abbreviation	Value	Unit
pendulum length	L	1.0	m
Pendulum mass	m_p	0.5	kg
Cart mass	m_c	1.0	kg
Spring stiffness	k_{spring}	100.0	N/m

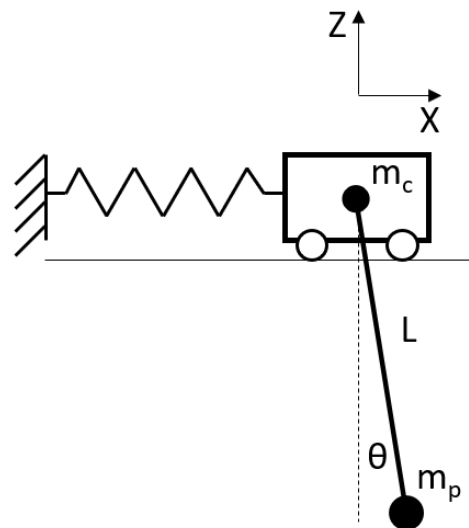


Figure F.1: Cart pendulum

The state space representation is given in Appendix B. The goal now is to use a PID controller to damp out the motion caused by an initial angle of the pendulum. The angle of the pendulum, θ , is set to 0.1 radians or 5.73 degrees and is then released. The goal is to design the PID controller such that it does not exert a force of more than 10N, damps the motion with 98% in 2 seconds, with a maximum x displacement of 0.5 meters and a maximum x velocity of 0.5 meters per second.

The control block diagram is constructed and is shown in E2. The control block diagram depicted is a regular control block diagram for a PID controller. The extra gain block at the bottom is just to isolate θ out of the 4 states that come out of the state space block. As the goal is to damp out any motion of the pendulum, due to a disturbance or an initial offset from its equilibrium position, the reference signal is set to 0. This means that in the sum block where the actual value of θ is subtracted from this reference value the error signal e is created which is used as input for the controller to make sure this error becomes 0 again.

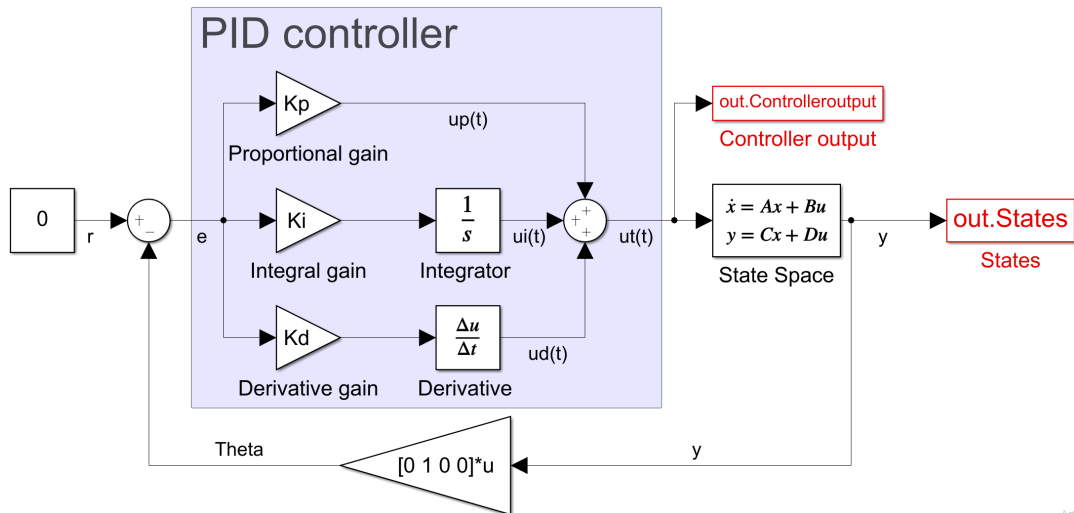


Figure E2: Control block diagram of the cart pendulum

The first step is to create Bode plot of the signal from u to y , which is just the frequency response of the system without controller. This is shown in Figure E3 which shows the frequency response of θ . As expected there are 2 peaks due to there being 2 degrees of freedom. These peaks are the natural frequency of the system. The lowest frequency is mostly due to the pendulum and is 0.49Hz . This is almost equal to a pure pendulum with out the cart and spring, given in equation E1. The second peak has much more influence of the cart mass and the spring.

$$f_{\text{pendulum}} = \frac{1}{2\pi\sqrt{\frac{L}{g}}} = 0.50\text{Hz} \quad (\text{E.1})$$

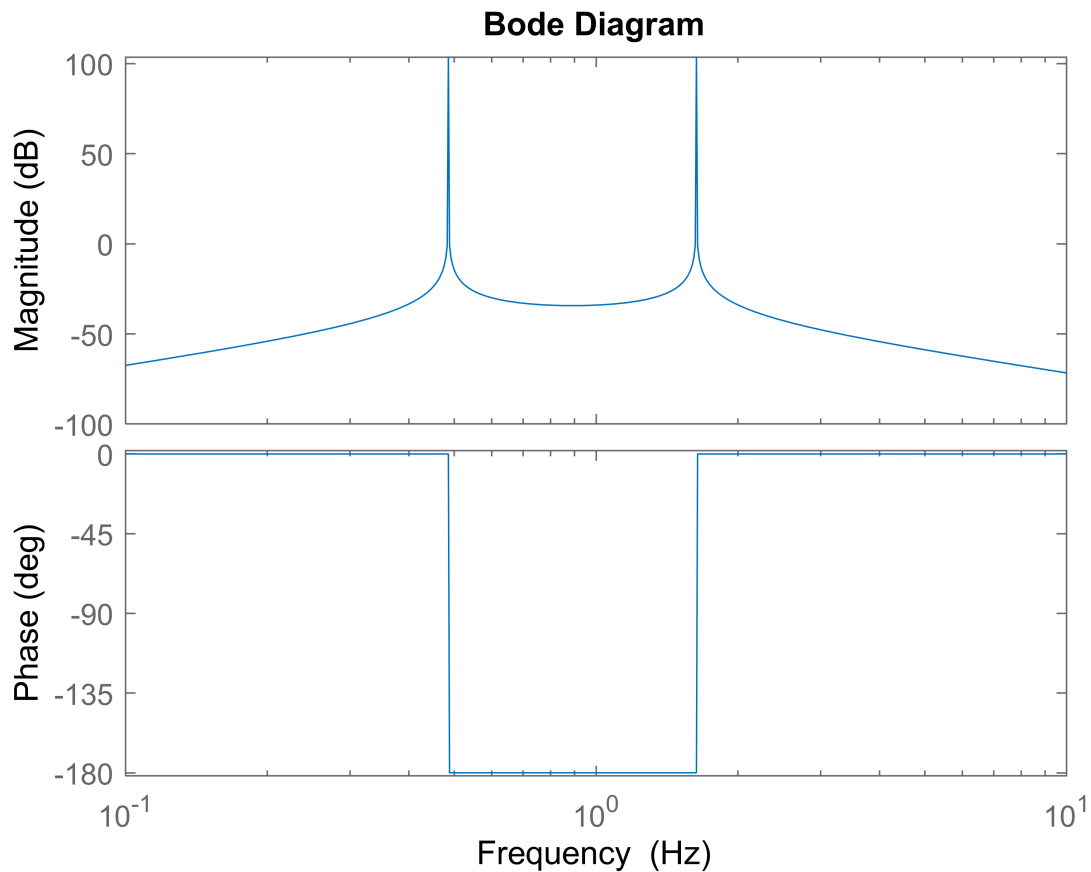


Figure E3: Bode plot of θ of the cart pendulum system

Due to the absence of damping the peaks are really sharp/steep and thus any excitation at this frequency will cause large deviations from its equilibrium point. Thus, the goal is to lower these peaks using the PID controller in order to get the desired results. In the same figure the controller transfer function is shown together with the open and closed loop frequency responses which include this controller. The response of the controller is the created from the signal e to u_t and the transfer function is shown in equation E2. The open loop response does include the controller and is created from the signal e to y and its transfer function is given in E3. The open loop line is the sum of the system and the controller response lines. The main purpose of the open loop response is to check the stability of the closed loop system. The closed loop is the signal from r to y with transfer function E4. The objective is to "straighten" the closed loop line out at $0dB$ so that any input relates to a more linear deviation.

$$\frac{u}{e} = C \quad (E2)$$

$$\frac{y}{e} = PC \quad (E3)$$

$$\frac{y}{r} = \frac{PC}{1 + PC} \quad (E4)$$

The values of K_p , K_i and K_d are chosen following the loop shaping method described in "High Performance mechatronics" [23]. First the bandwidth has to be determined. As this is a fictional situation and there is no real actuator the bandwidth is also arbitrary and is set at $f_c = 3Hz$. Now the gain is determined by checking what the gain, G_{dB} , is on the 'system' bode plot at that frequency. This is $-49Db$. The total gain, K_t , is then calculated using equation E5 [23] and is equal to -281.8 .

$$K_t = -\frac{1}{10^{\frac{G_{dB}}{20}}} \quad (E5)$$

in order to calculate the integral and derivative gain the respective frequencies should be known. These frequencies indicate when the integrating actions stops and the differentiating actions starts. they are computed using the bandwidth frequency f_c according to equations E6 and E7. these equations state that the differentiating frequency starts at $0.33f_c$ frequency while the integration frequency stops at approximately $0.1f_c$ [23]. These equations also convert them to radians in order for them to be directly implemented in the next step.

$$\omega_d = \frac{2\pi f_c}{3} \quad (E6)$$

$$\omega_i = 2\pi \cdot 0.1 \cdot f_c \quad (E7)$$

Now the next step is to determine the PID gains using the total gain K_t and the frequency f_c . K_p , K_i and K_d is given in equations E8, E9 and E10 [23]. Implementing the correct values in these equations will lead to the following values for the PID gains: $K_p = -81.8$, $K_i = -154$ and $K_d = -13$.

$$K_p = \frac{K_t}{3} \quad (E8)$$

$$K_i = K_p \omega_i \quad (E9)$$

$$K_d = \frac{K_p}{\omega_d} \quad (E10)$$

In Figure E4 can be seen that the peaks after the implementation are almost non-existent compared to the original system and thus are artificially damped by the controller.

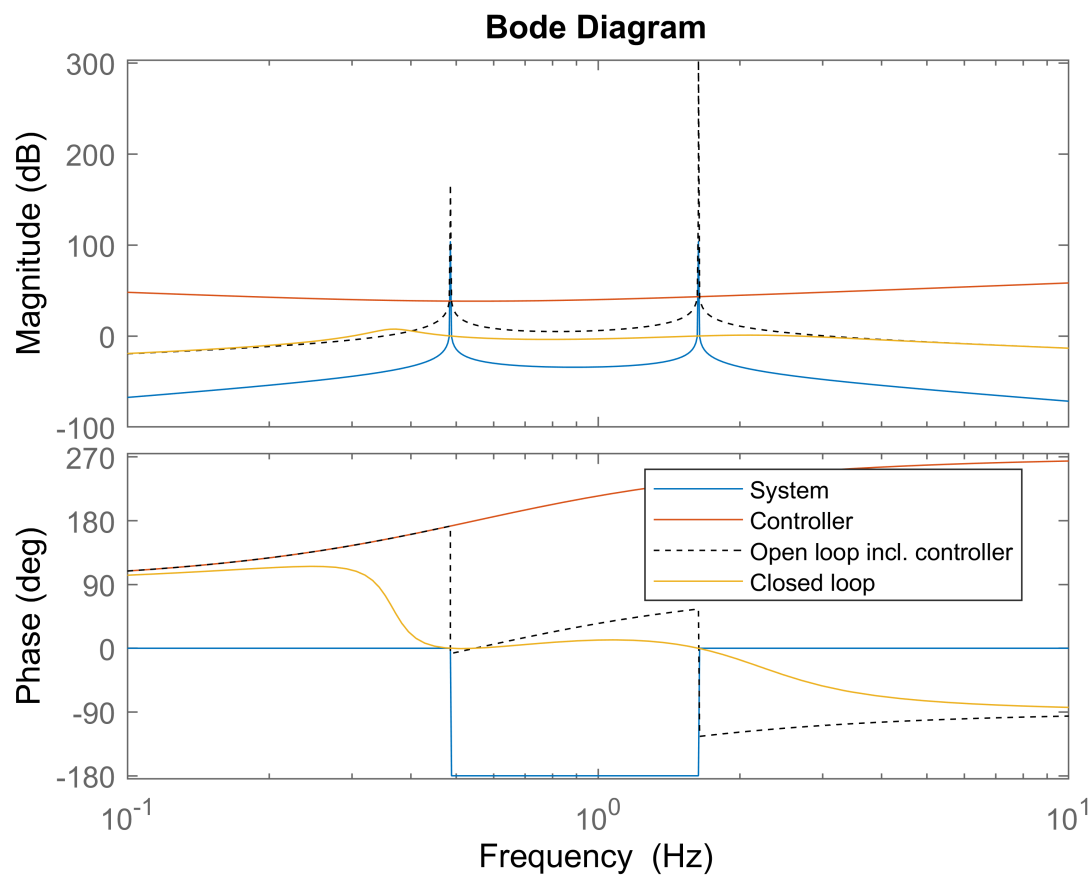
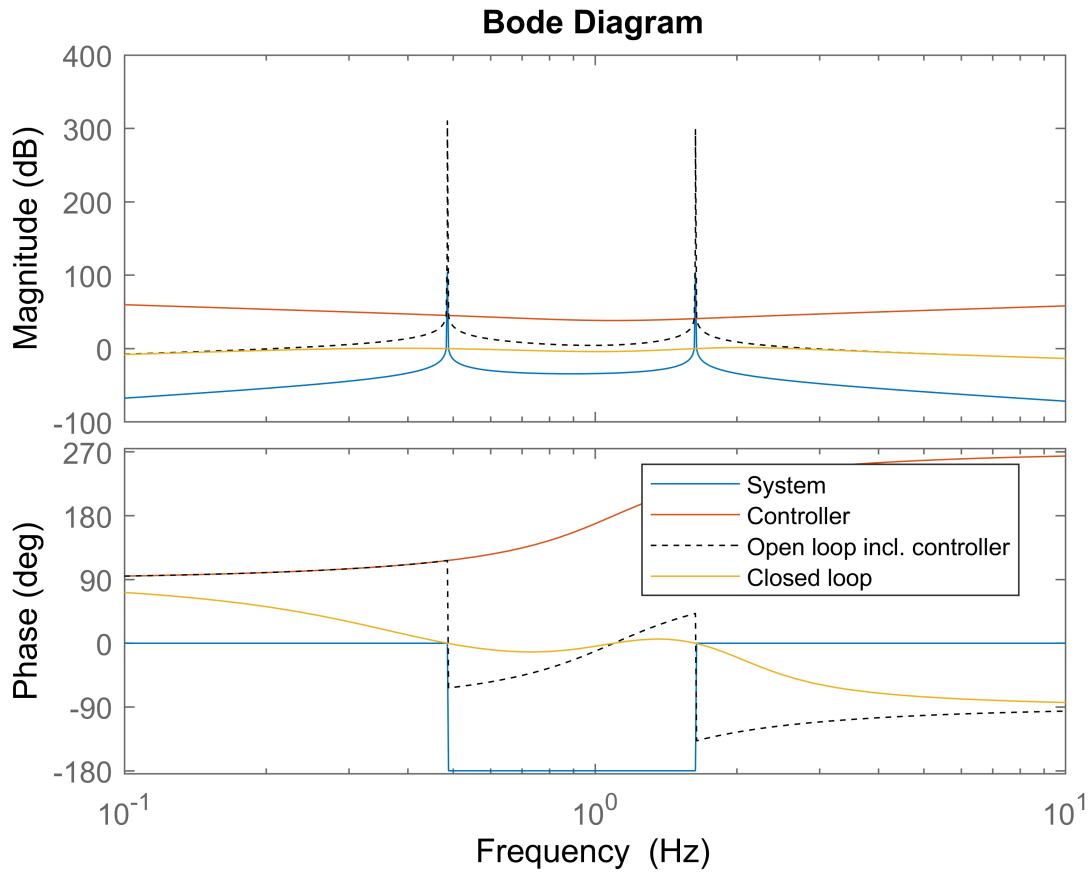


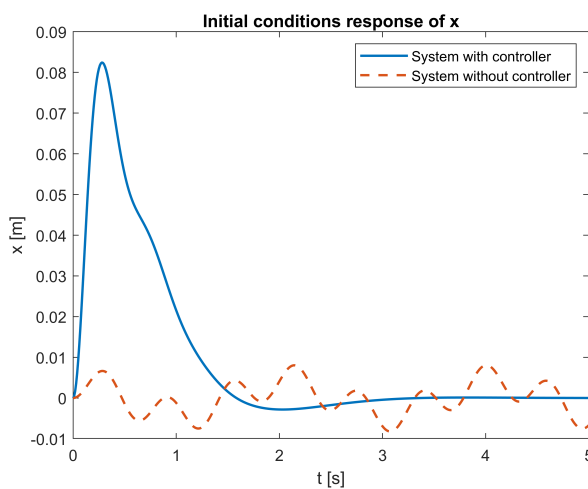
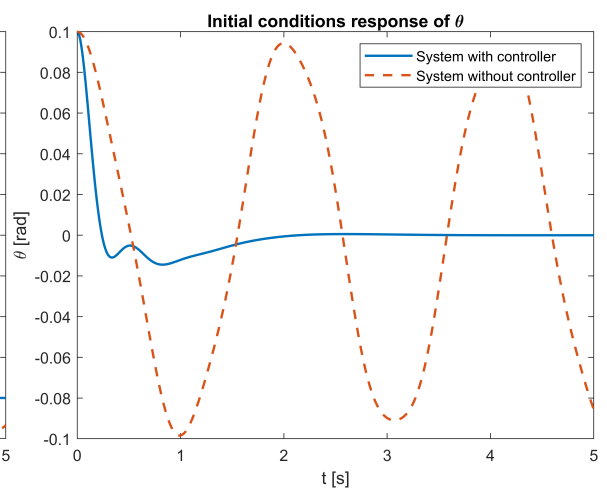
Figure E4: Bode plots of θ of the cart pendulum system and important transferfunctions

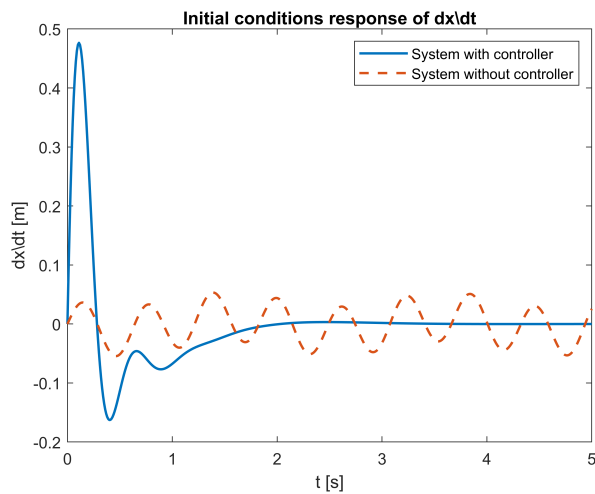
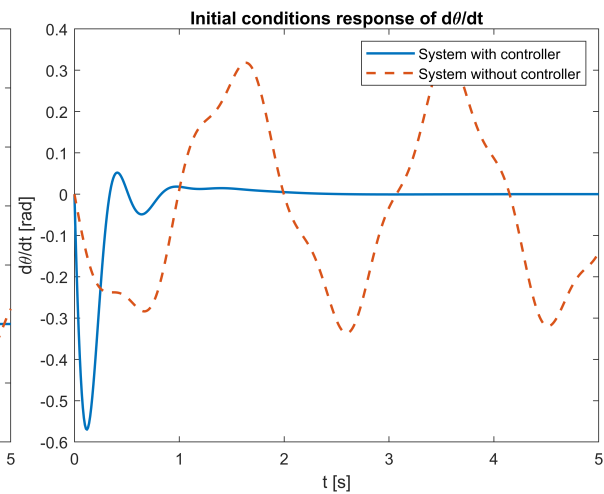
However, at the region where the integrator is working (at the lower frequencies) there is still some tuning that can be done in order to get better results. The frequency at which it stops should be higher and thus the integral frequency is shifted to start to 1.2Hz (instead of $0.1f_c$ it is now taken as $0.4f_c$). The final bodeplot can be seen in figure E5 with final values for proportional gain K_p , integral gain K_i and derivative K_d as -81.8 , -617.0 and -13.0 , respectively

When we look at the phase margins in the bottom part of the figure it can be observed that the open loop line never crosses the -180 degrees line and thus it is stable. This means in theory the gain can go to infinity and the system would still be stable.

Figure E5: Bode plot of θ of the cart pendulum system and important transferfunctions

The motion of the original system without and with tuned controller are shown in Figures E6, E7, E8 and E9. It can be seen that the motion of the original system will repeat itself indefinitely due to there being no damping terms and thus no decay of the motion can be seen. Adding the PID controller will damp this motion out artificially.

Figure E6: Initial conditions response of x Figure E7: Initial condition response of θ

Figure E8: Initial conditions response of x Figure E9: Initial condition response of θ

As can be seen in these figures the requirements that were mentioned before are met. The maximum x position is 0.08 m , which is far below the allowed 0.5 m . For the maximum x velocity the maximum value should not exceed 0.5 m/s and the maximum velocity is 0.48 m/s . The required time to reach 2% of its initial value is also met. As can be seen in at 2 seconds the curve is almost completely stable and has value of $-5.95 \cdot 10^{-4}$ which is 0.60% of its initial value and thus this criteria is also met.

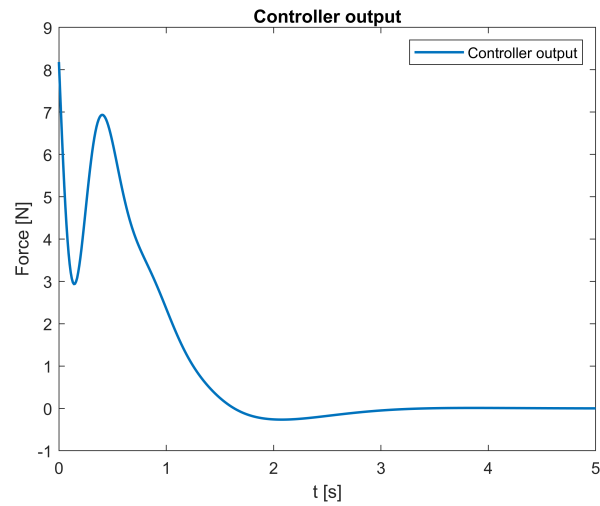


Figure F.10: Bode plot of θ of the cart pendulum system

The last requirement was to not exceed a force on the cart of $10N$. The controller output is shown in Figure F.10. The maximum controller output is at the start. This makes sense as the largest deviation from the desired resting position is at this moment. However, it does not exceed a value of $8.2N$ and thus the last requirement is also met. Note that this controller is not optimized and is solely for demonstrative purposes to help understand the theory brought forward in Chapter 2.

G

EULER ANGLES

Due to the fact that the problem involves rotating objects *Euler angles* can be used as they are a useful tool to describe rotations in the different frames. Examples of rotating rigid bodies in the presented problem are the monopile around the gripper and the gyroscope around its axis in the form of the angular velocity of the disc and the nutation or precession angle.

For rotations about a fixed point a rotation matrix R can be used which is the orthogonal matrix that transforms the coordinates of a point r from the body fixed coordinate system to the space fixed coordinate system as shown in equation G.1 [30].

$$r = Rr' \tag{G.1}$$

Where r is the space fixed coordinates and r' the body fixed coordinates.

Given a vector \vec{r} which indicates the position r in the body frame, this vector will always keep its length after any transformation to other reference frames. The space fixed frame has three axis on which the unit vectors $\vec{e}_x, \vec{e}_y, \vec{e}_z$ lie [30]. To find vector \vec{r} coordinates given in the space fixed frame the vector is rewritten to $\vec{r} = x\vec{e}_x + y\vec{e}_y + z\vec{e}_z$ where x, y and z are scalars which can be grouped into a coordinate vector called r , $r = (x, y, z)$. The difference between the two vectors is not important in 1 coordinate system. However, with rotating rigid bodies multiple reference frames are clearly described. One frame moves with the object and is called the body fixed frame, denoted by the prime symbols $(\vec{e}_{x'}, \vec{e}_{y'}, \vec{e}_{z'})$, and the space fixed reference frame $(\vec{e}_x, \vec{e}_y, \vec{e}_z)$ [30].

The next step is to express r in the body fixed coordinate system which gives $\vec{r} = x'\vec{e}_{x'} + y'\vec{e}_{y'} + z'\vec{e}_{z'}$ this will lead to the body fixed coordinates of $r' = (x', y', z')$ [30]. These will remain constant in a rigid body. Any rotation the body makes around the origin of the reference frame can be described by the Euler angles, in most cases the (3-1-3) sequence is used (3-1-3 referencing to the order in which the body rotates around its axis in this case first the z-axis then x-axis and again z-axis). The body fixed frame is initially aligned with the space fixed reference frame and the first rotation will be about its \vec{e}_z -axis with an angle ϕ . A new coordinate system is now denoted by $(\vec{e}_\xi, \vec{e}_\eta, \vec{e}_\zeta)$ as shown in Figure G.1a [30].

The next rotation is about the intermediate coordinate system's \vec{e}_ξ -axis by the angle θ creating another intermediate coordinate system given by $(\vec{e}_{\xi'}, \vec{e}_{\eta'}, \vec{e}_{\zeta'})$ as depicted in Figure G.1b. The final rotation is about the $\vec{e}_{\zeta'}$ -axis with an angle ψ . This rotation will lead to the body fixed axis system $(\vec{e}_{x'}, \vec{e}_{y'}, \vec{e}_{z'})$ [30].

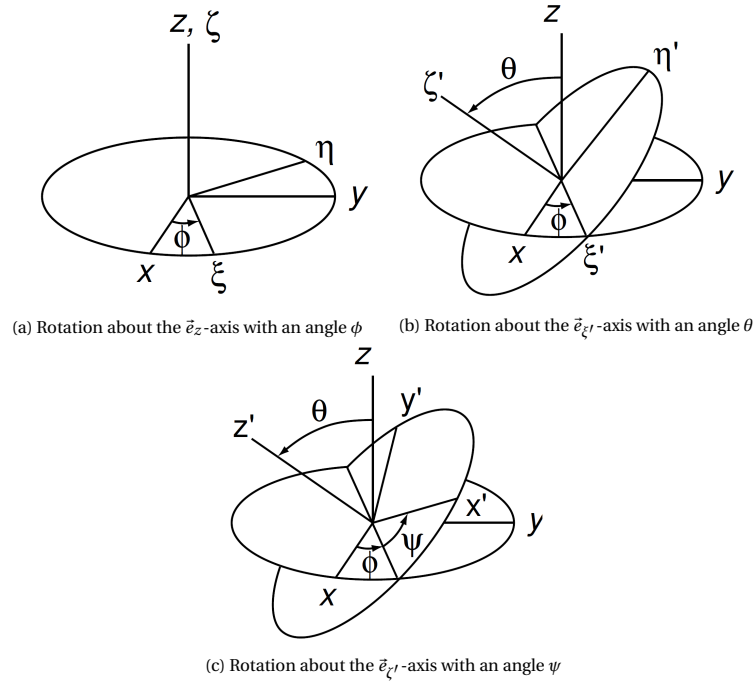


Figure G.1: Illustration of the rotations around a fixed point using Euler angles [30]

Each of the rotations mentioned above can be described by rotation matrices. The rotation around the \vec{e}_z -axis by an angle ϕ can be represented mathematically as shown in equation G.2. Where ρ are the coordinates (ξ, η, ζ) of point r in the $(\vec{e}_\xi, \vec{e}_\eta, \vec{e}_\zeta)$ coordinate system [30].

$$r = R_\phi \rho, \quad \text{with} \quad R_\phi = \begin{bmatrix} \cos \phi & -\sin \phi & 0 \\ \sin \phi & \cos \phi & 0 \\ 0 & 0 & 1 \end{bmatrix} \quad (\text{G.2})$$

The second rotation around the \vec{e}_ξ by angle θ is shown in equation G.3 in which ρ' are the coordinates (ξ', η', ζ') of point r in the $(\vec{e}_{\xi'}, \vec{e}_{\eta'}, \vec{e}_{\zeta'})$ coordinate system [30].

$$\rho = R_\theta \rho', \quad \text{with} \quad R_\theta = \begin{bmatrix} 1 & 0 & 0 \\ 0 & \cos \theta & -\sin \theta \\ 0 & \sin \theta & \cos \theta \end{bmatrix} \quad (\text{G.3})$$

The last rotation is around the $\vec{e}_{\xi'}$ by angle ψ is shown in equation G.4 in which r' are the body fixed coordinates as mentioned before [30].

$$\rho' = R_\psi r', \quad \text{with} \quad R_\psi = \begin{bmatrix} \cos \psi & -\sin \psi & 0 \\ \sin \psi & \cos \psi & 0 \\ 0 & 0 & 1 \end{bmatrix} \quad (\text{G.4})$$

Substituting these equations, equation G.4 in G.3 and then equation G.3 into G.2, will lead to the complete rotation matrix from body coordinates to the space fixed coordinates and can be written as equation G.1. In this case R is defined in the three Euler angles (ϕ, θ, ψ) and is the product of these 3 consecutive rotation as given in G.5. The order of matrix multiplication has to be noted [30].

$$R = R_\phi R_\theta R_\psi \quad (\text{G.5})$$

to go from the space fixed to the body fixed coordinates the inverse transformation has to be performed as shown in equation G.6.

$$r' = R^{-1}r \quad (\text{G.6})$$

with (again note the order of the matrix multiplication)

$$R^{-1} = R^T = R_\psi^T R_\theta^T R_\phi^T \quad (\text{G.7})$$

The same result can be found by reversing the direction of the consecutive rotations (changing the sign of the angle from + to -) and reversing the order.

Since angular velocity and acceleration are important aspects in the matter of stabilizing the rotations of a MP by means of a gyroscope it is convenient to state how to derive the angular acceleration and velocities when Euler angles are used.

Angular velocity $\vec{\omega}$ is usually taken by taking the time derivative of equation G.1 and substituting G.6. As mentioned previously body fixed coordinates are constant and thus the term $\dot{r} = 0$ giving equation G.8.

$$\dot{r} = \dot{R}R^T r \quad (\text{G.8})$$

The antisymmetric matrix $\dot{R}R^T$ will be named $\tilde{\omega}$ which is the same as the cross product of the angular velocities components $\vec{\omega}$, $(\omega_x, \omega_y, \omega_z)$ in the body fixed coordinate system, given in equation G.9.

$$\dot{r} = \tilde{\omega}r = \omega \times r \quad (\text{G.9})$$

Where

$$\tilde{\omega} = \begin{bmatrix} 0 & -\omega_z & \omega_y \\ \omega_z & 0 & -\omega_x \\ -\omega_y & \omega_x & 0 \end{bmatrix} \quad (\text{G.10})$$

The components from of the angular velocity in the space fixed system can be obtained by implementing the partial derivatives of equation G.8 which is given in G.11 [30].

$$\tilde{\omega} = \frac{\delta R}{\delta \phi} R^T \dot{\phi} + \frac{\delta R}{\delta \theta} R^T \dot{\theta} + \frac{\delta R}{\delta \psi} R^T \dot{\psi} \quad (\text{G.11})$$

There is a shortcut to this method as it is quite a cumbersome task. The angular velocity vectors around each axis are given in G.12.

$$\vec{\omega}_\phi = \dot{\phi} \vec{e}_z, \quad \vec{\omega}_\theta = \dot{\theta} \vec{e}_\xi \quad \text{and} \quad \vec{\omega}_\psi = \dot{\psi} \vec{e}_{\zeta'} \quad (\text{G.12})$$

The sum of these angular velocities is the total angular velocity of the entire body $\vec{\omega} = \vec{\omega}_\phi + \vec{\omega}_\theta + \vec{\omega}_\psi$. The angular velocity components in the space fixed system $(\omega_x, \omega_y, \omega_z)$ are found by using the transformation matrices and transforming each angular velocity accordingly, equation G.13 [30].

$$\begin{bmatrix} \omega_x \\ \omega_y \\ \omega_z \end{bmatrix} = \begin{bmatrix} 0 \\ 0 \\ \dot{\phi} \end{bmatrix} + R_\phi \begin{bmatrix} \dot{\theta} \\ 0 \\ 0 \end{bmatrix} + R_\phi R_\theta \begin{bmatrix} 0 \\ 0 \\ \dot{\psi} \end{bmatrix} \quad (\text{G.13})$$

Which after expanding the terms looks as equation G.14.

$$\begin{bmatrix} \omega_x \\ \omega_y \\ \omega_z \end{bmatrix} = \begin{bmatrix} 0 & \cos \phi & \sin \phi \sin \theta \\ 0 & \sin \phi & -\cos \phi \sin \theta \\ 1 & 0 & \cos \theta \end{bmatrix} \begin{bmatrix} \dot{\phi} \\ \dot{\theta} \\ \dot{\psi} \end{bmatrix}, \quad \omega = A\dot{u} \quad (\text{G.14})$$

As can be seen A is now used to name the angular velocity transformation matrix. To get the components of the angular velocity expressed in the body fixed system $\omega' = (\omega'_x, \omega'_y, \omega'_z)$ can be found transforming equation

G.14: $\omega' = R^T A \dot{u}$. However, the same approach can be followed as before by transforming the individual angular velocities stated in G.12 leading to G.15 [30].

$$\begin{bmatrix} \omega'_x \\ \omega'_y \\ \omega'_z \end{bmatrix} = \begin{bmatrix} 0 \\ 0 \\ \dot{\psi} \end{bmatrix} + R_\psi^T \begin{bmatrix} \dot{\theta} \\ 0 \\ 0 \end{bmatrix} + R_\psi^T R_\theta^T \begin{bmatrix} 0 \\ 0 \\ \dot{\phi} \end{bmatrix} \quad (\text{G.15})$$

Eventually leading to equation G.16 when expanded

$$\begin{bmatrix} \omega'_x \\ \omega'_y \\ \omega'_z \end{bmatrix} = \begin{bmatrix} \sin \psi \sin \theta & \cos \psi & 0 \\ \cos \psi \sin \theta & -\sin \psi & 0 \\ \cos \theta & 0 & 1 \end{bmatrix} \begin{bmatrix} \dot{\phi} \\ \dot{\theta} \\ \dot{\psi} \end{bmatrix}, \quad \omega' = B \dot{u} \quad (\text{G.16})$$

It goes without saying that in this case $B = R^T A$. It should be noted that Both matrix A and B have determinant of $-\sin \theta$ and have a singularity whenever $\theta = \pm \pi$ [30]. This phenomenon is known as *gimbal lock* at which it is impossible to uniquely determine the Euler angles from the angular velocity [30].

BIBLIOGRAPHY

- [1] N.D.P. Barltrop, Centre for Marine, and Petroleum Technology. *Floating Structures: A Guide for Design and Analysis*. CMPT, 1998. URL <https://books.google.nl/books?id=B04ZAQAAIAAJ>.
- [2] Robert D. Blevins. *Formulas for natural frequency and mode shape*. Krieger, Malabar, 1995. ISBN 0894648942 9780894648946.
- [3] Bloomberg. *Offshore Wind Outlook 2019 World Energy Outlook special report, 2020* (accessed February 21, 2020). <https://about.bnef.com/blog/global-offshore-wind-market-set-to-grow-sixfold-by-2030/>.
- [4] K. E. Diamond. Why offshore wind is viable for northeastern, east central coastal states. *Electric Light and Power*, 88(4):44, 2010.
- [5] DNVGL. *DNVGL-RP-C205, Environmental conditions and environmental loads*, 2017.
- [6] DNVGL. *DNVGL-ST-N001, Marine operations and marine warranty*, 2018.
- [7] General Electric. *GE's Haliade-X offshore wind turbine*, 2021 (accessed January 08, 2021). [https://www.ge.com/renewableenergy/wind-energy/offshore-wind/haliade-x-offshore-turbine#:~:text=VIDEO-,World's%20Most%20Powerful%20offshore%20Wind%20Turbine,64%25\)%2C%20and%20digital%20capabilities.](https://www.ge.com/renewableenergy/wind-energy/offshore-wind/haliade-x-offshore-turbine#:~:text=VIDEO-,World's%20Most%20Powerful%20offshore%20Wind%20Turbine,64%25)%2C%20and%20digital%20capabilities.)
- [8] Peter Enevoldsen and George Xydis. Examining the trends of 35 years growth of key wind turbine components. *Energy for Sustainable Development*, 50:18–26, 2019. ISSN 0973-0826. doi: <https://doi.org/10.1016/j.esd.2019.02.003>. URL <http://www.sciencedirect.com/science/article/pii/S097308261831353X>.
- [9] Sif Offshore foundations. *Wind foundations*, 2021 (accessed January 08, 2021). <https://sif-group.com/en/wind/foundations>.
- [10] W. Gawronski. *Advanced Structural Dynamics and Active Control of Structures*. Springer New York, 2004. ISBN 9780387406497. URL <https://books.google.nl/books?id=GRp0lk6LrXMC>.
- [11] Michel Geradin and Daniel J. Rixen. *Mechanical Vibrations : Theory and Application to Structural Dynamics*. John Wiley & Sons, Incorporated, New York, UNITED KINGDOM, 2015. ISBN 9781118900185. URL <http://ebookcentral.proquest.com/lib/delft/detail.action?docID=1873192>.
- [12] Thomas C. Gillmer. *Modern ship design*. Naval Institute Press, Annapolis, Md., 2d ed. edition, 1975. ISBN 0870213881 9780870213885.
- [13] Jerry H. Ginsberg. *Engineering dynamics*. Cambridge University Press, Cambridge, 2008. ISBN 0521883032 9780521883030. URL <http://catdir.loc.gov/catdir/toc/ecip0717/2007018344.html><http://catdir.loc.gov/catdir/enhancements/fy0743/2007018344-d.html><http://catdir.loc.gov/catdir/enhancements/fy0743/2007018344-b.html>.
- [14] Klaus Hasselmann, T. Barnett, E. Bouws, H. Carlson, D. Cartwright, K. Enke, J. Ewing, H. Gienapp, D. Hasselmann, P. Kruseman, A. Meerburg, Peter Muller, Dirk Olbers, K. Richter, W. Sell, and H. Walden. Measurements of wind-wave growth and swell decay during the joint north sea wave project (jonswap). *Deut. Hydrogr. Z.*, 8:1–95, 1973.
- [15] Leo H. Holthuijsen. *Waves in Oceanic and Coastal Waters*. Cambridge University Press, Cambridge, 2007. ISBN 9780521129954. doi: DOI:10.1017/CBO9780511618536. URL <https://www.cambridge.org/core/books/waves-in-oceanic-and-coastal-waters/F6BF070B00266943B0ABAFAE6F54465>.

- [16] IEA. *Global Offshore Wind Market Set to Grow Sixfold by 2030*, 2020 (accessed February 21, 2020). <https://www.iea.org/reports/offshore-wind-outlook-2019>.
- [17] J. M. J. Journee, W. W. Massie, R. H. M. Huijsmans, Faculty of Mechanical Maritime Delft University of Technology, and Engineering Materials. *Offshore hydromechanics*. TU Delft, Delft, 3rd ed. edition, 2000.
- [18] R. Lacal-Arántegui, J. M. Yusta, and J. A. Domínguez-Navarro. Offshore wind installation: Analysing the evidence behind improvements in installation time. *Renewable and Sustainable Energy Reviews*, 92:133–145, 2018. doi: 10.1016/j.rser.2018.04.044. URL <https://www.scopus.com/inward/record.uri?eid=2-s2.0-85046368692&doi=10.1016%2fj.rser.2018.04.044&partnerID=40&md5=608a5df06041be6ff6d41a2386a414ea>.
- [19] F. A. Leve, B. J. Hamilton, and M. A. Peck. *Spacecraft momentum control systems*. Spacecraft Momentum Control Systems. Microcosm Press and Springer, 2015. doi: 10.1007/978-3-319-22563-0. URL <https://www.scopus.com/inward/record.uri?eid=2-s2.0-84955356939&doi=10.1007%2f978-3-319-22563-0&partnerID=40&md5=102db24c116975801daa7f955f04ec48>.
- [20] L. Li, Z. Gao, T. Moan, and H. Ormberg. Analysis of lifting operation of a monopile for an offshore wind turbine considering vessel shielding effects. *Marine Structures*, 39:287–314, 2014. doi: 10.1016/j.marstruc.2014.07.009. URL <https://www.scopus.com/inward/record.uri?eid=2-s2.0-84908343434&doi=10.1016%2fj.marstruc.2014.07.009&partnerID=40&md5=b4cb1c59b179698f93f01ecd02c94a1d>.
- [21] Lizet Ramirez, Daniel Fraile, Guy Brindley, WindEurope. *Offshore Wind in Europe, Key trends and statistics 2019*, 2020 (accessed February 21, 2020). <https://www.iea.org/reports/offshore-wind-outlook-2019>.
- [22] Jorge Montoya-Chairez, Victor Santibanez, and Javier Moreno-Valenzuela. Adaptive control schemes applied to a control moment gyroscope of 2 degrees of freedom. *Mechatronics*, 57:73–85, 2019. ISSN 0957-4158. doi: <https://doi.org/10.1016/j.mechatronics.2018.11.011>. URL <https://www.sciencedirect.com/science/article/pii/S0957415818301867>.
- [23] R. Munnig Schmidt, G. Schitter, A. Rankers, and J. Van Eijk. *The Design of High Performance Mechatronics - 2nd Revised Edition : High-Tech Functionality by Multidisciplinary System Integration*. IOS Press, Incorporated, Burke, NETHERLANDS, THE, 2014. ISBN 9781614993681. URL <http://ebookcentral.proquest.com/lib/delft/detail.action?docID=1637647>.
- [24] Michel K. Ochi. *Ocean Waves: The Stochastic Approach*. Cambridge Ocean Technology Series. Cambridge University Press, Cambridge, 1998. ISBN 9780521563789. doi: DOI: 10.1017/CBO9780511529559. URL <https://www.cambridge.org/core/books/ocean-waves/4C4CF2D1D70FDAB03724DFD41F705E72>.
- [25] Orcaflex. *Orcaflex applications*, 2020 (accessed April 10, 2020). <https://www.orcina.com/orcaflex/applications/>.
- [26] Orcaflex. *Orcaflex Extreme value statistics theory*, 2021 (accessed August 25, 2021). <https://www.orcina.com/webhelp/OrcaFlex/Content/html/Extremevaluestatisticstheory.htm>.
- [27] Tristan Perez and Paul D. Steinmann. Analysis of ship roll gyrostabiliser control. *IFAC Proceedings Volumes*, 42(18):310–315, 2009. ISSN 1474-6670. doi: <https://doi.org/10.3182/20090916-3-BR-3001.0007>. URL <https://www.sciencedirect.com/science/article/pii/S1474667016319139>.
- [28] Encyclopaedia Britannica Ronald A.R. Tricker, Claudia Cenedese. *Wind waves and swell*, 2020 (accessed March 02, 2020). <https://www.britannica.com/science/wave-water#ref301517>.
- [29] H. Schaub and J. L. Junkins. Singularity avoidance using null motion and variable-speed control moment gyros. *Journal of Guidance, Control, and Dynamics*, 23(1):11–16, 2000. doi: 10.2514/2.4514. URL <https://www.scopus.com/inward/record.uri?eid=2-s2.0-0033905770&doi=10.2514%2f2.4514&partnerID=40&md5=6d66bd8cc1e96dece2bc2105d09d5bfb>.

- [30] A. L. Schwab and J. P. Meijaard. How to draw euler angles and utilize euler parameters. In *ASME 2006 International Design Engineering Technical Conferences and Computers and Information in Engineering Conference*, volume Volume 2: 30th Annual Mechanisms and Robotics Conference, Parts A and B, pages 259–265, 2006. doi: 10.1115/detc2006-99307. URL <https://doi.org/10.1115/DETC2006-99307>.
- [31] Sánchez, Gutiérrez López, Negro, and M. Dolores Esteban. Foundations in offshore wind farms: Evolution, characteristics and range of use. analysis of main dimensional parameters in monopile foundations. *Journal of Marine Science and Engineering*, 7:441, 2019. doi: 10.3390/jmse7120441. URL <https://www.mdpi.com/2077-1312/7/12/441>.
- [32] N. C. Townsend and R. A. Shenoi. Control strategies for marine gyrostabilizers. *IEEE Journal of Oceanic Engineering*, 39(2):243–255, 2014. doi: 10.1109/JOE.2013.2254591. URL [https://www.scopus.com/inward/record.uri?eid=2-s2.0-84899484214&doi=10.1109/\\$%2fJOE.2013.2254591&partnerID=40&md5=4c5707e4f4946c406428ae52c0ea79cc](https://www.scopus.com/inward/record.uri?eid=2-s2.0-84899484214&doi=10.1109/$%2fJOE.2013.2254591&partnerID=40&md5=4c5707e4f4946c406428ae52c0ea79cc).
- [33] N. C. Townsend, A. J. Murphy, and R. A. Shenoi. A new active gyrostabiliser system for ride control of marine vehicles. *Ocean Engineering*, 34(11):1607–1617, 2007. ISSN 0029-8018. doi: <https://doi.org/10.1016/j.oceaneng.2006.11.004>. URL <http://www.sciencedirect.com/science/article/pii/S0029801807000364>.
- [34] Evrim Ursavas. A benders decomposition approach for solving the offshore wind farm installation planning at the north sea. *European Journal of Operational Research*, 258(2):703–714, 2017. ISSN 0377-2217. doi: <https://doi.org/10.1016/j.ejor.2016.08.057>. URL <http://www.sciencedirect.com/science/article/pii/S0377221716306968>.
- [35] Heike Vallery and Arend L. Schwab. *Advanced Dynamics*. Delft University of Technology, Delft, 2018. ISBN 9789461869487.
- [36] Ronny Votel and Doug Sinclair. Comparison of control moment gyros and reaction wheels for small earth-observing satellites. In *26th Annual Aiaa/usu Conference on Small Satellites: Enhancing Global Awareness Through Small Satellites*. Digital commons, 2012.
- [37] G. Xydis. A techno-economic and spatial analysis for the optimal planning of wind energy in kythira island, greece. *International Journal of Production Economics*, 146(2):440–452, 2013. doi: 10.1016/j.ijpe.2013.02.013. URL [https://www.scopus.com/inward/record.uri?eid=2-s2.0-84886723242&doi=10.1016/\\$%2fj.ijpe.2013.02.013&partnerID=40&md5=690a84bd784da4a98449c11e9d31d224](https://www.scopus.com/inward/record.uri?eid=2-s2.0-84886723242&doi=10.1016/$%2fj.ijpe.2013.02.013&partnerID=40&md5=690a84bd784da4a98449c11e9d31d224).
- [38] Ian R. Young. *Wind generated ocean waves*. Amsterdam : Elsevier, 1999. ISBN 0080433170. URL <http://lib.ugent.be/catalog/rug01:000752409>.